LBNL-41425

ERNEST ORLANDO LAWRENCE
BERKELEY NATIONAL LABORATORY

Ultra-Short-Period W/B4C Multilayers for X-Ray Optics-Microstructure Limits on Reflectivity

Christopher C. Walton

Materials Sciences Division

December 1997

Ph.D. Thesis

REFERENCE COPY
Does Not
Circulate

Bldg. 50 Library - Ref.
Lawrence Berkeley National Laboratory

LBNL-41425
Copy 1

DISCLAIMER

This document was prepared as an account of work sponsored by the United States Government. While this document is believed to contain correct information, neither the United States Government nor any agency thereof, nor the Regents of the University of California, nor any of their employees, makes any warranty, express or implied, or assumes any legal responsibility for the accuracy, completeness, or usefulness of any information, apparatus, product, or process disclosed, or represents that its use would not infringe privately owned rights. Reference herein to any specific commercial product, process, or service by its trade name, trademark, manufacturer, or otherwise, does not necessarily constitute or imply its endorsement, recommendation, or favoring by the United States Government or any agency thereof, or the Regents of the University of California. The views and opinions of authors expressed herein do not necessarily state or reflect those of the United States Government or any agency thereof or the Regents of the University of California.

LBNL-41425

Ultra-Short-Period W/B4C Multilayers for X-Ray Optics-Microstructure Limits on Reflectivity

Christopher Charles Walton
Ph.D. Thesis

College of Engineering
Department of Materials Science and Mineral Engineering
University of California, Berkeley

and

Materials Sciences Division
Ernest Orlando Lawrence Berkeley National Laboratory
University of California
Berkeley, CA 94720

December 1997

This research was supported by the Director, Office of Energy Research, Office of Basic Energy Sciences, Materials Sciences Division, of the U.S. Department of Energy under Contract No. DE-AC03-76SF00098

LBNL-41425

Ultra-Short-Period W/B_4C Multilayers for X-Ray Optics-Microstructure Limits on Reflectivity

by

Christopher Charles Walton

B.S. (Massachusetts Institute of Technology) 1990
M.S. (University of California, Berkeley) 1992

A dissertation submitted in partial satisfaction of the

requirements for the degree of

Doctor of Philosophy

in

Engineering-Materials Science and Mineral Engineering

in the

GRADUATE DIVISION

of the

UNIVERSITY OF CALIFORNIA, BERKELEY

Committee in charge:

Professor Gareth Thomas, Chair
Dr. Jeffrey B. Kortright
Professor Didier de Fontaine
Professor Raymond Jeanloz

Fall 1997

Ultra-Short-Period W/B4C Multilayers for X-Ray Optics-Microstructure Limits on Reflectivity

Copyright © 1997

by

Christopher Charles Walton

The U.S. Department of Energy has the right to use this document
for any purpose whatsoever including the right to reproduce
all or any part thereof

Abstract

Ultra-Short-Period W/B_4C Multilayers for X-Ray Optics–
Microstructure Limits on Reflectivity

by

Christopher Charles Walton

Doctor of Philosophy in Engineering – Materials Science and Mineral Engineering

University of California, Berkeley

Professor Gareth Thomas, Chair

Multilayer thin films are used as Bragg reflectors for soft x-rays in the energy range 50eV < E < 1000eV in many x-ray optics applications such as x-ray microscopes and telescopes, reducing optics for extreme ultraviolet (EUV) lithography, and x-ray polarizers and phase retarders. Applications often depend critically on reflectivity, which has not been systematically characterized for multilayer periods below 20Å. For this study, W/B_4C multilayers were fabricated by magnetron sputtering on Si(111), with periods from 48Å to as little as 4.7Å. The x-ray reflectivity measured at λ = 1.54Å and at 45° incidence (289eV < E < 860eV) was found to decrease sharply for multilayer periods less than 15-20Å. Examination by high-resolution transmission electron microscopy (HRTEM) showed an expansion of the thickness of the W-rich layers of 30-40% from the nominal values, consistent with intermixture of the two materials during sputter growth, and discontinuous W-rich layers for multilayer periods below about 15Å. The experimental data for the specular reflectivity in the hard and soft x-ray regimes and the diffuse scattering fit well to a model of multilayer roughness. The model is expressed as a power-law dependence of roughness on spatial frequency. Analysis of small-angle scattering in transmission from multilayers grown on free-standing Si_3N_4 membranes confirms the onset of discontinuity at periods between 14Å and 22Å. Spectroscopy studies by x-ray absorption (NEXAFS) and electron energy loss (EELS) at the boron K-edge (188eV) are consistent with changes in the average boron bonding environment, as the multilayer period decreases and the W-rich layers are increasingly thin and dispersed. A discrete W-rich phase is present for periods at least as small as 6.3Å. Results are consistent with interpenetration of the discontinuous and

sparsely-covered W-rich layers, not interdiffusion of the two materials, being the primary cause of reflectivity loss at very short periods. Implications for materials choice and sputtering conditions for optimal reflectivity of short-period multilayers are discussed.

to my parents, whose respect for education made this possible,

and to Erin.

TABLE OF CONTENTS

Title page i
Abstract
Dedication iii
Table of Contents iv
Acknowledgements vi

1. INTRODUCTION 1
   1.1 Multilayer Mirrors as X-Ray Optical Elements 1
   1.2 Short-Period Multilayers 4
   1.3 Motivation for this Study 5
   1.4 Methods of this Study and Organization of the Thesis 6
   1.5 Figures 8
   1.6 References 9

2. SAMPLE PREPARATION AND ANOMALIES OF LAYER THICKNESSES 10
   2.1 Equipment Equipment and Specifications 10
   2.2 Sputtering Rates and Thickness Determination 12
   2.3 Details of Thickness Determination and its Relation to Actual Structure 12
   2.4 Summary 16
   2.5 Figures 18
   2.6 References 20

3. X-RAY PERFORMANCE: PEAK REFLECTIVITY 21
   3.1 Experimental 21
   3.2 Reflectivity Results 23
   3.3 Blue Multilayers 25
   3.4 Motivation for Further Study: Understanding Microstructure Limits on Performance 26
   3.5 Possible Mechanisms Limiting Reflectivity 26
   3.6 Figures 30
   3.7 References 35

4. MICROSTRUCTURE BY TRANSMISSION ELECTRON MICROSCOPY 36
   4.1 Introduction 36
   4.2 Experiment 37
   4.3 Results and Discussion 38
      4.3.1 Cross-Section 38
      4.3.2 Plan-View 41
   4.4 Summary 42
   4.5 Figures 44
   4.6 References 47

5. INTERNAL BONDING – NEAR-EDGE SPECTROSCOPY 48
   5.1 Introduction 48
      5.1.1 Theory of Absorption Spectroscopy 49
      5.1.2 Application 51
   5.2 Electron Energy-Loss Spectroscopy 51
      5.2.1 Experiment 51
      5.2.2 Data Reduction 52
      5.2.3 Results 52
      5.2.4 Discussion 53
   5.3 Near-Edge X-ray Absoption Fine Structure (NEXAFS) in transmission 54
      5.3.1 Introduction 54
      5.3.2 Experiment and Samples 55

5.3.3 Results and Data Reduction 56
5.3.4 Discussion 56
5.4 NEXAFS by Total Electron Yield (TEY) 58
5.4.1 Introduction 58
5.4.2 Experiment 59
5.4.3 Results 59
5.4.4 Discussion 59
5.5 General Discussion 62
5.6 Conclusions 63
5.7 Figures 65
5.8 References 73

6. ANALYSIS OF X-RAY REFLECTIVITY 74
6.1 Introduction 74
6.2 Theory and Methods of Reflectivity Analysis 74
6.2.1 Examples Case 74
6.2.2 Calculating Reflectivity 78
6.2.3 Analyzing Real Multilayers 79
6.2.4 Treatment of Interface Roughness 82
6.3 Analysis of Reflectivity Results 86
6.3.1 Fitting Methods 86
6.3.2 Fit Results 87
6.4 Summary 93
6.5 Figures 95
6.6 References 103

7. DIFFUSE SCATTERING STUDIES 105
7.1 Introduction 105
7.2 Small-Angle Scattering 106
7.2.1 Experiment 107
7.2.2 Data Reduction 108
7.2.3 Results 109
7.2.4 Analysis 109
7.2.5 Fits and Discussion 112
7.2.6 Conclusions 115
7.3 Rocking Scans 116
7.3.1 Introduction 116
7.3.2 Experiment and Data Reduction 117
7.3.3 Results 118
7.3.4 Discussion 118
7.3.5 Analysis 118
7.3.6 Fits 123
7.3.7 Conclusions from Rocking Scan Analysis 126
7.4 General Conclusions on Diffuse Scattering Results 127
7.5 Figures 128
7.6 References 133

8. SYNTHESIS 134
8.1 Conclusions 134
8.2 Suggestions for Improving Reflectivity at Ultra-Short Periods 136
8.3 Suggested Future Work on W/B_4C 137
8.4 References 139

Acknowledgements

I would like especially to acknowledge Dr. Jeff Kortright for much-needed support and mentorship through difficult times in the research leading to this thesis, and Prof. Gareth Thomas for longstanding support in materials and microscopy efforts. I would also like to thank the dissertation committee for their efforts in reviewing this dissertation.

Special thanks are due to Eric Gullikson for much advice and assistance in experimental work at the Advanced Light Source and interpretation of results, and to Ron Tackaberry and Everett Harvey for always knowing the answers to my computer troubles. Thank you also to Paul Denham for his expert repairs and advice on sputtering and diffractometry equipment, and to Julie Najita for invaluable help with statistics.

This research was supported by the director, Office of Energy Research, Office of Basic Energy Sciences, Materials Sciences Division of the U.S. Department of Energy under Contract #AC03-76SF00098.

Chapter One

Introduction

1.1 Multilayer Mirrors as X-Ray Optical Elements

A major challenge in the use of x-ray light has always been the fabrication of optical elements that can change the path of the radiation to make it more useful. The early applications of x-rays for medical imaging all relied on line-of-sight paths direct from the x-ray tube, and the problem of focussing or reflecting the radiation remains sufficiently challenging that the most heavily used imaging applications, such as medical and airport x-rays and industrial parts inspection, are still done in this way. Unlike visible light, x-rays experience very small refraction or reflection on passing through matter, and generally cannot be focused or reflected by simple lenses and mirrors. In physical terms, the index of refraction is much closer to unity, for a given material, in the x-ray region of the spectrum (with energies in the approximate range of 50eV to 100keV) than in the visible (approximately 2eV to 3eV). Because of this, the optical contrast at any single interface of two materials, and hence the reflection or refraction of the light, is weak. In addition, this energy range includes many core and valence electron excitations, making most materials strongly absorbing and further limiting the use of refractive optics.

Two exceptions to this have been used for many x-ray optics applications. At very low incidence angles, nearly parallel to the surface, any smooth surface will show high reflectivity, because the perpendicular momentum transfer decreases with the angle and can be made too small for penetration. In the case of x-rays the refractive index is usually less than unity, and at low angles there is total external reflection below the critical angle. This fact has been used for many applications, such as glancing-incidence focussing mirrors for synchrotron beamlines and Wolter-type telescope optics consisting of many concentric rings reflecting at glancing angles. However, this method is limited by the small reflecting area that can be presented to the beam, because of the steep angle, and by large optic aberrations. It is also

limited by the small deflection of the beam available at each reflection, though for some applications many sequential small-angle reflections from a single curved surface can produce a large deflection, in a "whispering-gallery" waveguide. This is a true optical reflection, in that it occurs at a single surface at a symmetrical condition of equal incident and reflected angles (*specular* reflection), and is not a constructive interference effect.

A second exception uses the coherent diffraction of x-rays by a natural crystal – the diffracting crystal is used as a mirror for a specific incident angle and wavelength of light. In this method, the weak scattering at any single plane of atoms adds constructively and coherently with that at many parallel planes. Diffraction is an elastic scattering process, meaning the scattered rays have the same energy as the incident. Though this is often called referred to as a "reflection" from the crystal, it is fundamentally different from reflection at a surface, because the intensity depends on the internal structure of the diffracting crystal, and the diffraction can occur at any angle relative to the sample surface. It occurs for a given crystal only at specific combinations of angle and wavelength given by the Bragg equation:

$$n\lambda = 2d\sin\theta \tag{1}$$

where n (a positive integer) is the order of the diffraction event, λ is the wavelength of the incident light , d is the distance separating the scattering planes, and θ is the angle of incidence, measured from the surface. Natural crystals find many applications in x-ray optics, such as monochromators to collimate the beam from a divergent source and select desired wavelengths. Common crystals are silicon, germanium and graphite, and for somewhat longer wavelengths, mica and potassium biftalate (KAP). However, this method has its own limitations. First, to obtain high reflectivity, the crystal must have continuous planes in the proper orientation, so it occurs only for large flat single crystals or within the small bending curvature the crystal can withstand. Second, the d-spacings available between the scattering planes (and hence the available diffraction angle at a given wavelength) are limited to the natural periods of available crystals. The bending of the crystals can be a difficult mechanical problem and produces its own optical aberrations.

The principle of a diffractive optic, however, using constructive interference from many weak scattering planes to produce strong reflectivity, can be extended if a crystal can be made at any desired d-spacing. If the crystal consists not of a periodic array of planes of atoms but of a periodic stack of films

deposited on a substrate, then the artificial crystal can be made at any period and on a curved surface. This is the idea of the multilayer mirror. By operating at the Bragg condition of the multilayer, high reflectivity can be obtained at high angles of incidence, where the specular reflectivity from the surface is vanishingly small. The multilayer can equivalently be viewed as a stack of half-wave interference coatings like those used in the visible light regime.

The first attempts to construct such a multilayer were by Koeppe[1] and Deubner[2]. They deposited gold and silver layers by electroplating but were unable to observe diffraction of x-rays by the layered structure. The first multilayer diffraction was found by DuMond and Youtz,[3] who made multilayers of Cu and Au with periods of about 200Å. After a time of about one month the diffraction peak had disappeared because of room-temperature diffusion of the two materials. This was the beginning of a long body of research, recently reviewed by Greer,[4] on the use of multilayers in diffusion studies.

In x-ray optic applications, significant early advances were made by Spiller[5-7] and Barbee and Keith[8] and an early review of theory was published by Underwood and Barbee.[9] Many groups around the world now work on multilayer optics from glancing incidence to normal incidence, and fabrication techniques and mirror performance have been studied in detail. A general review book covering theory and many applications has been published by Spiller,[10] and a recent review of mirror performance and limitations is given by Kortright.[11] The literature will be covered in more detail later in the appropriate chapters.

A general schematic of a multilayer mirror is given in Fig. 1. The layers are grown in alternating order of a dense material (typically a refractory metal) and a light one, with the d-spacing carefully controlled to meet the Bragg condition for the desired wavelength and angle of incidence. The denser material is selected to have the highest possible optical contrast with the lighter material, as measured by the difference of the refractive indices at the wavelength of interest, and the light material is chosen as a spacer between the dense layers with the lowest possible absorption. In practice, in addition to their optical properties, the two materials' reactivity, relative surface energy, and tendency toward interdiffusion strongly influence the choice of materials. The layers are usually grown by evaporation or sputtering, though electron-beam evaporation has also been used.[12]

The layer interfaces scatter x-rays coherently: a small fraction of the incident wave is scattered elastically from each interface, and all the scattered waves have the same phase relationship to the incident beam. There is also a small inelastic component which is incoherently scattered: the scattered waves have random phase relative to the incident beam. In the multilayer, each period actually contains two reflecting surfaces, the top and bottom of the absorber layer. Both contribute to the reflectivity though they have a 180° phase difference from each other. The wavelength maximally reflected at a given angle is determined only by the period of the structure, and the relative thicknesses of the two layers within the period affect only the relative heights of the different orders of multilayer reflectivity, analogous to the relationship between the plane spacing and the structure factor in diffraction from a natural crystal. Reflectivity can be increased by depositing more layers, which narrows the reflectivity peak, since this is increasing the crystal size. With a large number of periods, absorption by the upper layers decreases the contribution of the lower layers to the reflectivity, so the achievable reflectivity approaches a limit which depends on the optical properties of the materials. This effect of absorption can be decreased somewhat by reducing the thickness of the dense layers from half the d-spacing to a lower value, and the lower absorption compensates for increasing destructive interference of the waves from the two interface types. In practice, imperfections in the multilayer can increase from layer to layer, making very large numbers of layers less useful, and most applications use 200 layer pairs or less. A treatment of the considerations in designing a multilayer mirror is provided by Spiller.[10]

1.2 Short-Period Multilayers

With the improvement of the technology of multilayer growth and the increasing availability of high-brightness synchrotron x-ray sources, interest has grown in the use of multilayers of shorter and shorter periods. As described in the review by Kortright, near-normal-incidence reflectivity (i.e. maximum fraction of incident intensity reflected at the first Bragg interference peak) is generally good for energies up to about 100eV, with the best reflectivities near this energy being about 68% obtained from the well-researched Mo/Si system, with more recent slight improvements in Mo/Be. For higher energies (shorter periods) available reflectivities are lower. This is in part a fundamental physical barrier, since with

increasing energy the refractive indices of all materials tend to unity as the materials interact more weakly with the x-rays, and the available optical contrast between any two materials is reduced. However, the layer microstructure begins to affect performance as well. For normal incidence at an energy of 100eV, the multilayer period is about 65Å, so the individual layers are 25-35Å, or on the order of 15 atomic diameters, thick. As the period is reduced further, any roughness or other imperfection in the interfaces becomes increasingly important. Even taking into account the lower optical contrast, the experimental reflectivities begin to fall farther below the maximum theoretically available for any material combination. For periods near 20Å, the best normal-incidence reflectivities are a few percent. Common applications of multilayers of period 20Å or less are to increase reflectivity of grazing-incidence mirrors for hard x-ray mirrors for synchrotron beamlines, and for spectral analysis of light in the regime $\lambda = 10\text{-}30$Å.

Of particular interest for this study were applications of multilayers as linear polarizers and phase retarders. In work at soft x-ray energies near the Fe $L_{2,3}$ edge[13] Kortright *et al.* used W/B_4C multilayers with d = 12.4Å at an incidence angle of 45°. This is the polarizing angle (Brewster angle) at these wavelengths and this mirror can selectively reflect the s-polarized component of the beam (electric vector of the light normal to the plane of incidence) and suppress the p-component (electric vector parallel to plane of incidence), with an intensity extinction ratio of better than 10^4. The polarized soft x-ray beam can then be used to measure optical activity of materials in the soft x-ray regime, and with the tunable energy of a synchrotron can provide an element-specific magneto-optical probe.[14] The available signal for such experiments, however, depends on the reflectivity of the polarizing mirror, which for the experiments described was slightly less than 1%. W/B_4C is one of the few systems to show usable reflectivity at these wavelengths, but its reflectivity had not been studied carefully.

1.3 Motivation for This Study

The application to polarization studies in the soft x-ray gives a motivation to investigate the reflectivity of multilayers with very short periods of 15Å or less. This study was undertaken in part to systematically study how reflectivity depended on the period for such thin multilayers, in which the individual layers are only some 5 atoms thick or less. However more general questions present themselves.

How short can the period of W/B_4C be made? Why does W/B_4C still show reflectivity at these periods when many other common multilayer systems do not? What is the microstructure of a multilayer of near atomic dimensions? At what period is reflectivity lost completely, and what is the fundamental cause? This study was begun to answer these questions.

1.4 Methods of This Study and Organization of the Thesis

A combination of several techniques was needed to address the main questions of the study. The goal was to learn as much as possible about the internal structure of ultra-short-period W/B_4C multilayers, and what effect it has on their reflectivity. A systematic investigation of the reflectivity of W/B_4C was first made for periods of 30Å and below, with some samples extending the range to near 50Å. The details of the sputtering process used to make the multilayers, taking into account much existing knowledge on sputtering, gives some insight into the structure of the layers. The reflectivity was measured at the 45° incidence angle at which the multilayers are used in polarization applications, and at lower angles with hard x-rays (λ = 1.54Å, CuK_α), and the trends in reflectivity examined. The sputtering apparatus and its use for these samples is described in Chapter 2, and the reflectivity results at constant θ = 45° and constant λ = 1.54Å, along with high-angle CuK_α x-ray scans, are described in Chapter 3.

The transmission electron microscope gives a powerful local probe of the microstructure of the multilayers, which can help in understanding the effects of growth on reflectivity and microstructure. Features from atomic sizes to a few hundred Angstroms can be examined by direct imaging. Multilayer specimens were examined in cross-section and plan view, and these results are presented in Chapter 4.

With decreasing period, the interface regions occupy a larger fraction of the multilayer, and some change in the local bonding of the constituent atoms is expected. To measure changes in bonding, spectroscopic studies near the boron K edge, by Electron Energy Loss Spectroscopy (EELS) and Near-Edge X-ray Absorption Fine Structure (NEXAFS), are presented in Chapter 5.

While the x-ray reflectivity is the fundamental property of interest in the multilayers, it also gives detailed structural information. The experimental reflectivity can be compared with theoretical values calculated for ideal and imperfect layered structures, and the comparison used to study imperfections in the

layers. In this study, detailed modeling of the reflectivity was used, including imperfections of layer roughness and interdiffusion, and this is presented in Chapter 6. Finally, the diffuse (non-specular) scattering caused by the interface imperfections was studied directly, and the results compared with the reflectivity analysis, in Chapter 7. A synthesis of the final conclusions and suggestions for future work in this system are made in the final chapter.

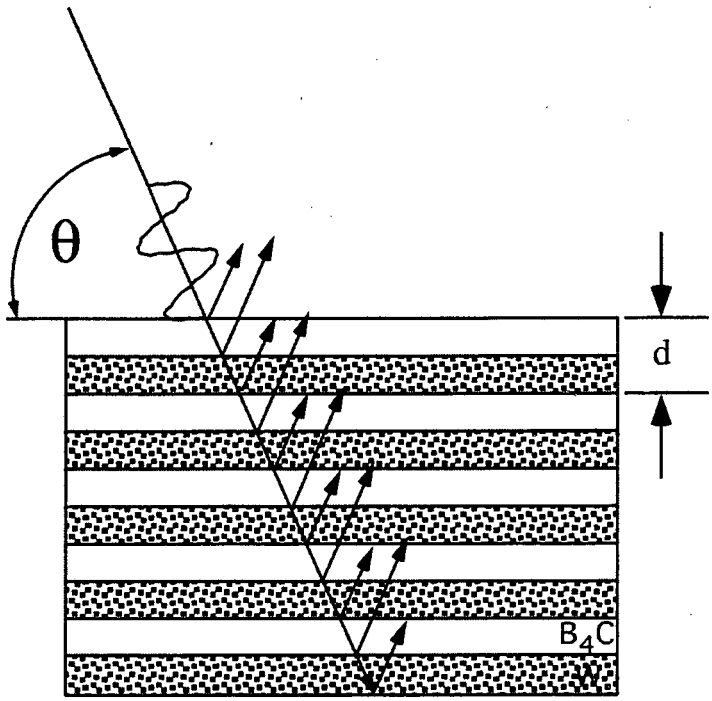

Fig. 1. Schematic of reflection of light by a multilayer mirror. Scattered waves from the same type of interface (top of borrom) are in phase with each other, but there is a 180° phase shift between the two types.

References

[1]H. Keoppe, Ph.D., Giessen, Hesse, Germany, 1923.

[2]W. Deubner, Ann. Phys. Leipzig **5**, 261 (1930).

[3]J. DuMond and J. P. Youtz, Journal of Applied Physics **11**, 357 (1940).

[4]A. L. Greer, "Diffusion and reactions in thin films," presented at the Symposium B of the 1994 E-MRS Spring Conference, Strasbourg, France, 1994 (unpublished).

[5]E. Spiller, "Reflective multilayer coatings for the far UV region," Applied Optics **15** (10), 2333-8 (1976).

[6]R. P. Haelbich, A. Segmuller, and E. Spiller, "Smooth multilayer films suitable for X-ray mirrors," Applied Physics Letters **34** (3), 184-6 (1979).

[7]E. Spiller, "Low-loss reflection coatings using absorbing materials," Applied Physics Letters **20** (9), 365-7 (1972).

[8]T. W. Barbee and D. C. Keith, presented at the Workshop on Instrumentation for Synchrotron Radiation Research, 1978 (unpublished).

[9]J. H. Underwood and T. W. Barbee, Jr., "Layered synthetic microstructures as Bragg diffractors for X rays and extreme ultraviolet: theory and predicted performance," Applied Optics **20** (17), 3027-34 (1981).

[10]Eberhard Spiller, *Soft X-Ray Optics* (SPIE Optical Engineering Press, Bellingham, Wash. USA, 1994).

[11]J. B. Kortright, "Status and limitations of multilayer X-ray interference structures," Journal of Magnetism and Magnetic Materials **156** (1-3), 271-5 (1995).

[12]E. Louis, H. J. Voorma, N. B. Koster *et al.*, "Multilayer coated reflective optics for extreme UV lithography," presented at the International Conference on Micro- and Nanofabrication, Davos, Switzerland, 1994 (unpublished).

[13]R. Carr, J. B. Kortright, M. Rice *et al.*, "Performance of the elliptically polarizing undulator on SPEAR," presented at the 5th International Conference on Synchrotron Radiation Instrumentation, Stony Brook, NY, USA, 1994 (unpublished).

[14]J. B. Kortright and M. Rice, "Soft X-ray optical rotation as element-specific magneto-optical probe," presented at the Symposium Magnetic Ultrathin Films, Multilayers and Surfaces. Symposium, San Francisco, CA, USA, 1995 (unpublished).

Chapter Two

Sample Preparation and Anomalies of Layer Thicknesses

2.1 Equipment and Specifications

All multilayer specimens used in this study were fabricated with the multilayer sputtering system at the Center for X-Ray Optics at LBNL. The system uses well-established magnetron sputtering technology and is shown schematically in Fig. 1. The substrates are held in circular frames mounted in the sputtering table. The table rotates under the control of a stepper motor to bring the substrates over the various stationary sputtering guns in sequence. The stepper motor is guided by simple commands entered into a computer to give the repeated rotations necessary for the multilayer structure. As the table turns, a planetary rotation spins the samples within it to improve the uniformity of the coatings. The table can hold 3 specimens but for multilayers only two can be used per run because of the spacing of the guns. The specimens are electrically grounded to the chamber walls through the frames holding them.

The magnetron guns are surrounded with shields which confine the plasma so the sputter yield is directed mostly up at the substrates, and the target-substrate distance is about 10cm. One of the three guns is connected to an rf source and impedance-matching network, and the other two to dc sources. The rf power is generally needed for depositing insulating materials which could not conduct away the current needed to support a dc plasma, while dc sputtering is generally preferred for conductors. The guns use standard 4-inch sputtering targets available commercially. This study used 99.95% pure W from Pure Tech Inc. and 99.9% pure B_4C fromVacuum Engineering and Materials Co. The targets are stored in air when not in use, but are presputtered for several minutes before depositing on real substrates to allow any contaminants to be removed.

The sputtering chamber uses a mechanical pump for roughing to about 1 mtorr and a helium cryogenic pump to reach its base pressure near 1 x 10^{-6} torr. Pressures in the mtorr and above are measured with a capacitance manometer, and those below with a Granville-Philips ion gauge. The sputtering gas (99.998% Ar for this work) is introduced at a controlled rate, and the pressure is maintained with a feedback loop with an accuracy of ±0.005mtorr. All samples in this study were sputtered at 2.5mtorr, the pressure found by previous experience with this system to give the highest reflectivity multilayers. The effect of sputtering gas pressure on quality of x-ray multilayers has also been studied by Stearns *et al.*[1]

Substrates for reflectivity studies were standard (111) silicon wafers, 3 inches in diameter and cut about 3° off the (111) plane. Such a miscut is standard in the electronics industry because the ledges of the cut-off (111) planes aid in growth of device layers on the silicon when the native oxide has been removed. For these multilayers the native oxide (about 20Å thick) was left in place. For x-ray transmission measurements free-standing membranes of Si_3N_4 were used. These are produced by the Microtechnology Center at the Lawrence Livermore National Laboratory, by coating silicon wafers with Si_3N_4 then etching the silicon from the back to leave a window of Si_3N_4. The windows are 3mm by 3mm and the membrane is about 1500Å thick. For TEM plan-view specimens, glass microscope slides were heated and coated with Crystalbond 509 microcrystalline wax (Remco Industries). Copper 400-mesh TEM grids were placed on the molten wax where they floated by surface tension, and the slides were allowed to cool. The multilayers were deposited on the slides, covering also the grids and the wax in the grid holes, and after deposition the wax was dissolved with acetone leaving the TEM grids supporting the multilayer films. The grids were then dipped in boiling acetone (56°C) to remove any residual wax and examined without further preparation.

Sputtering runs were started with a base pressure of 2.5x-10^{-6}torr or better. The small d-spacings require low sputtering power, typically 400W rf for B_4C or 0.1A dc current for W. Rates are on the order of 1Å/s so samples typically spend about 5-10s over each gun. A typical run lasts about 2 hours, at the end of which the rotating table and samples have reached a temperature of 40-50°C. When the guns are turned off the chamber pressure drops almost immediately to near or below the starting base pressure, and the chamber is vented with dry nitrogen. No active heating or cooling of the substrates is used. Analysis of the gas in the chamber using a quadrupole residual-gas analyzer (RGA) shows that at its minimum or base

pressure (typically 1.2×10^{-6} torr) the predominant species is water (5×10^{-7} torr) with most of the balance as O, O_2 and Ar. During sputtering the Ar is of course the dominant species. Specimens produced in this chamber and analyzed by Rutherford Backscattering Spectroscopy (RBS) have shown about 1at% Ar incorporated from the sputtering gas.

All samples were stored in vacuum when not in use because of concern about oxidation. The total exposure to atmospheric pressure was generally 24 hours or less for all specimens.

2.2 Sputtering Rates and Thickness Determination

Each set of sputtering runs begins with rate testing for the particular targets in use, since there is variation of the rates with the increasing wear of the targets, the strength of the magnets on each sputtering gun, and for other reasons not well understood. Rate testing is done directly with multilayers, rather than single films of the constituents. A set of multilayers is made, keeping the rf power constant (B_4C) while using a wide range of dc currents. The d-spacing of each is measured (as described in Section 3.2), and the results are plotted as the rate per period versus the dc current (W). The best line is drawn through this plot. Regression of this line to zero dc current gives the rate for the B_4C alone (see Fig. 2), and the rest of the rate at some nonzero dc current is attributed to the tungsten. From the diagram we can choose any ratio of the W and B_4C thicknesses by choosing the right dc current, and any period by varying the table rotation speed. In practice different speeds are used over the different guns and between guns to save time, but the rate data used are the same.

2.3 Details of Thickness Determination and Its Relation to Actual Structure of Multilayers

In the case of materials which do not react, or when the reaction layers are much thinner than the multilayer period, the scheme above is sufficient to make a stack of any desired d and Γ (thickness ratio of the two components, expressed as the fraction of the total period occupied by the absorber layer). In the case where there is substantial reaction of the materials, however, the situation is more complicated. The quantity measured for rate testing is the multilayer period, and it is assumed that an increase in the period

with higher dc current is due to a thicker metal layer. But if the materials react, one layer will consume part of the other or a reaction layer will form in between, which will contribute to the period but may change the individual thicknesses by a different amount, which depends on the density of the reaction product and cannot be predicted from the linear regression alone. The evidence for this occurring in W/B_4C will be presented below.

The cross-section TEM of a 30Å W/B_4C multilayer is shown in Chapter 4, Fig. 1a. The nominal Γ (i.e. that expected from the rate data) for this specimen was 0.40, while the value measured from the micrograph is 0.64±0.05. The situation is similar in the 15Å multilayer in Chapter 4, Fig. 1b - a substantial expansion of the W-rich layer has occurred. For periods shorter than this Γ cannot be measured reliably from the TEM, but it is reasonable to expect that at least as much expansion would occur. This layer cannot simply be pure W from normal sputter growth, because if it were it would contribute to the overall thickness and be measured in the rate test. There are three other possibilities however. First, the W may have grown at much less than bulk density, and initial resputtering (removal of atoms from the growing film by heavier atoms deposited later) may have removed some of the B_4C below, reducing the overall thickness and deceiving the rate test; second, bulk-density W may have grown after the same resputtering phenomenon; or third, the W may have reacted with the B_4C below to form a lower-density compound. Each of these will now be considered.

Growth at low density is common in thin films, and is expected when arriving atoms have low mobility on the substrate because of a low substrate temperature (relative to the melting point of the sputtered material) or strong chemisorption of the atoms to the growing film. Both of these conditions apply in this case, since the melting point of W is over 10 times the temperature of the room-temperature substrate, and the W atoms can be expected to bond strongly with W, B or C in the growing films (see thermodynamic data presented below). However, underdense films of this sort are expected to densify substantially on annealing. An annealing study by Jankowski on sputtered W/B_4C multilayers[2] has found strong thermal stability and only small thickness changes for anneals at 500°C. Jankowski *et al.* found only a 6% contraction for a 20Å period multilayer, while the W layers are about 38% below bulk density under this hypothesis. In Jankowski's study, there was also a slight reduction in reflectivity but only by the amount expected for the reduction in period, consistent with little structural change. Since these

multilayers were sputtered under very similar conditions to the ones in this study it is not likely that a voided W structure was present, nor was it observed in Jankowski's TEM results. In sputtered multilayers in the similar W/C system[3-5], annealing has been found to expand the period while introducing crystallinity in the W layers, which is inconsistent with initial W far from its bulk density.

To examine the second possibility, x-ray fluorescence total yield tests were done by Dr. Robert Giaque of LBNL to measure the total amount of W present in the films. These tests compare the total tungsten L_β fluorescence signal from the W/B_4C multilayers with that of a standard W film, giving an absolute measurement of the number of W atoms present. The results are shown in Fig. 3. The specimens had 100 periods except the last which had 50; the results for the last have been doubled to normalize. The amount of W present is within about 10% of that expected from the nominal Γs for the entire range of multilayer periods 5Å-50Å, and there is no trend to the deviation from the expected value. The thicker layer cannot then be all W, since the observed thickness would require some 40% more W.

As for the third possibility, it is consistent with the thermodynamics of the system and the kinetics expected from the sputtering process. Arguments to support this in detail are presented below.

Thermodynamically W and B_4C are expected to react. Tungsten forms two carbides and four borides. An experimental ternary diagram published by Rudy[6] shows no ternary compounds but large ranges of solubility between the borides and carbides (Fig. 4). Using a standard state of 298K and published free energies of formation of the binary compounds, the following reactions are favorable:

$$4W + B_4C \rightarrow 4WB + C \qquad (\Delta G_{RXN} = -52.9 kJ/mol)$$

$$5W + B_4C \rightarrow 4WB + WC \qquad (\Delta G_{RXN} = -72.7 kJ/mol)$$

$$9W + B_4C \rightarrow 4W_2B + WC \qquad (\Delta G_{RXN} = -36.7 kJ/mol)$$

The first of these is approximately consistent with the mole ratios of W and B_4C present for $\Gamma = 0.4$. Of course in reality a sputtered film of high-T_m compounds on a cold substrate is likely to be too disordered for equilibrium stoichiometric compounds to form, but these data show that the driving forces for reaction are present.

From the literature on sputter growth many predictions can be made of the effects of the growth conditions on film structure. Many of these have recently been summarized by Smith in his text on thin

film deposition techniques.[7] The next few paragraphs will summarize what can be expected for the sputtering conditions used in this study.

Because the W atoms in the W target are much more massive than the Ar^+ ions in the plasma, it is expected that a significant fraction of the ions bombarding the target will be reflected from the target (as neutrals), and will bombard the growing film along with the W atoms being deposited. Moreover these neutrals have a significantly higher energy than the sputtered W atoms also arriving at the growing film. Simulations of the fraction reflected and energies of the reflected ions[8] with the TRIM code (TRansport of Ions in Matter; Biersack)[9], scaled for the sputtering voltages used in this study, predict that some 30% of the Ar ions will be reflected, with energies averaging about 100eV. This gives a reflected Ar flux about half the expected yield of W atoms. The energies of the W atoms can be described with the Thompson distribution,[10] and the majority of them are below 30eV under the conditions in this study. Thus the growing W film is subjected to considerable extra bombardment from the reflected Ar. During B_4C sputtering no reflected Ar is expected since the target B and C atoms are much lighter than Ar.

A "universal curve" of penetration depths of energetic particles bombarding a surface has been compiled by Ziegler[11] using the Lindhard, Scharff and Schiott (LSS) theory for particle implantation, which is accurate for many particle/material combinations when the penetration depth is greater than a few atomic diameters. This curve gives a penetration depth of about about 12Å for Ar atoms with energies of 100eV on a growing film of W. While this is on the edge of the applicability range of the theory, even as an estimate it shows that the reflected Ar neutrals should have a very significant intermixing effect on multilayers whose period is similar to this depth. More accurate numbers would require specific Monte Carlo investigations using the TRIM code.

In the experimental literature, Kortright and Denlinger[3] have investigated W/C multilayers from d = 8.3Å to 109Å and found evidence of substantial intermixing (as atomic neighbor correlations similar to WC and W_2C) even at the highest d-spacing. Jiang *et al.*[12] have investigated W/C multilayers of periods from 30Å to 90Å and found the W layers to be 3Å thicker than expected, and the C layers 7Å thinner, over the entire range. The authors conclude that a WC interface layer is formed during deposition but do not attribute it directly to the sputtering process. Svedberg *et al.*[13] have simulated sputter growth of Mo/W

multilayers (using the TRIDYN code from the Computer Physics Communications International code library) and found asymmetric interface widths - 12Å for W growing on Mo but 5Å for Mo on W. The difference is attributed to greater reflection of Ar from the W target, causing greater bombardment during the growth of the W film. In the case of W/B_4C this reflection, as described above, could account for the intermixing apparently occurring in the W layer, since the difference in masses is much greater and the bombardment would occur entirely during the W growth.

The apparent thickness of the W-rich layer, the moles of W it contains, and the assumption that the other layer is approximately bulk B_4C are sufficient information to calculate its density as $13 g/cm^3$ and its average composition as $WB_{1.0}C_{0.26}$, for the 30Å multilayer. For the 15Å multilayer the nominal Γ was less so the figures are $9.4\ g/cm^3$ and $WB_{2.5}C_{0.62}$. It appears from these numbers that the W-rich layers get denser at greater thicknesses, which is consistent with the intermixing model: as more W builds up the required mixing distance to the B_4C below increases, and the concentration of W and the density should increase. However, no general relationship between Γ_{meas} and Γ_{nom} over a range of thicknesses of the W-rich layer is possible from the information available. A detailed simulation of the sputtering process of the type used by Svedberg would shed light on this interesting question.

2.4 Summary

Sputtering rates of W in the multilayers show a nearly linear dependence on sputtering current, which, when measured over a range of currents, allows a linear regression to obtain the sputtering rates for both materials. These rates can be used to fabricate a multilayer of any desired period and relative W thickness Γ. However, the apparent value of Γ (measured by cross-section in the TEM) is 30-40% larger than the nominal value expected from the sputtering rates. Measurements of the amount of W present show that it is near the nominal value, indicating that the extra volume of the W layer is attributable to intermixing with the B_4C layer. Theoretical and experimental studies in the literature on the physics of the sputtering process show that during growth of the W layers, intermixing of the heavier W atoms with the B_4C layer beneath is expected for the sputtering conditions used. The W-rich layers therefore have a

density significantly less than that of bulk W. The intermixing density of these layers will be addressed further in Chapter 5, and will be related to x-ray reflectivity in Chapter 6

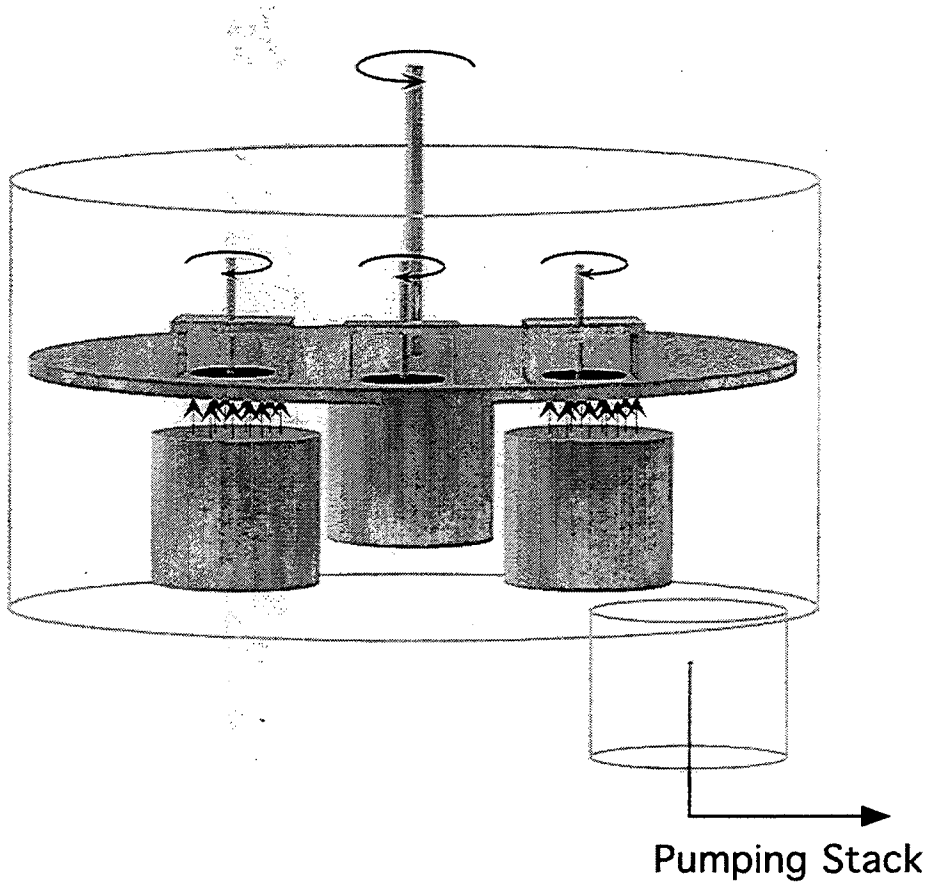

Fig. 1. Schematic of sputtering chamber used to make multilayer specimens. Three sputtering guns point up at samples in the rotating sample table.

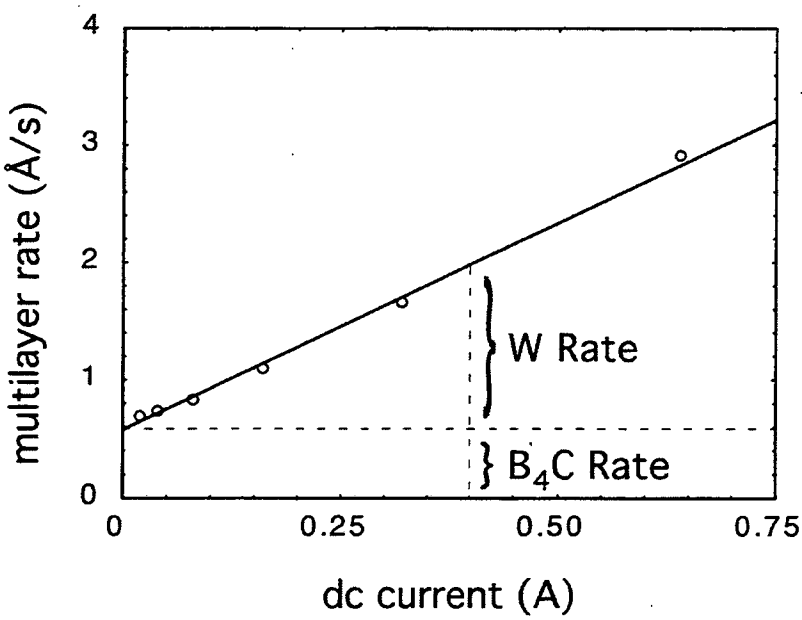

Fig. 2. Typical sputtering rate data. The vertical axis is the quotient of the multilayer period and the total time spent over both guns for one period.

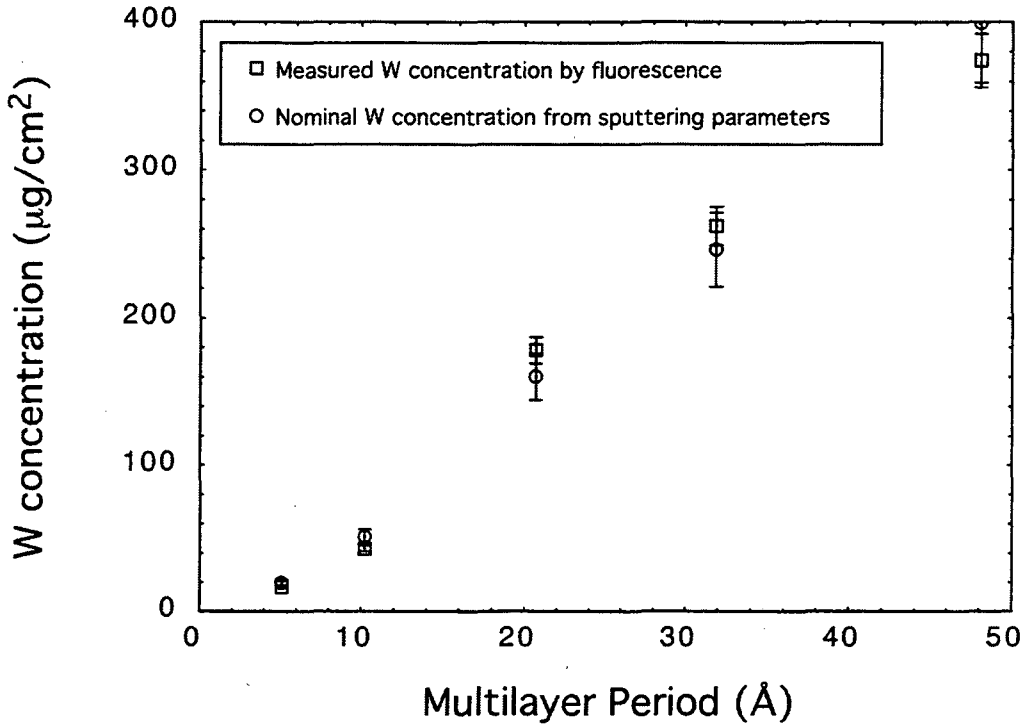

Fig. 3. Measurements of absolute tungsten concentration per unit area, by x-ray fluorescence total yield, for 5 multilayers covering the full range of periods, 5Å to 50Å.

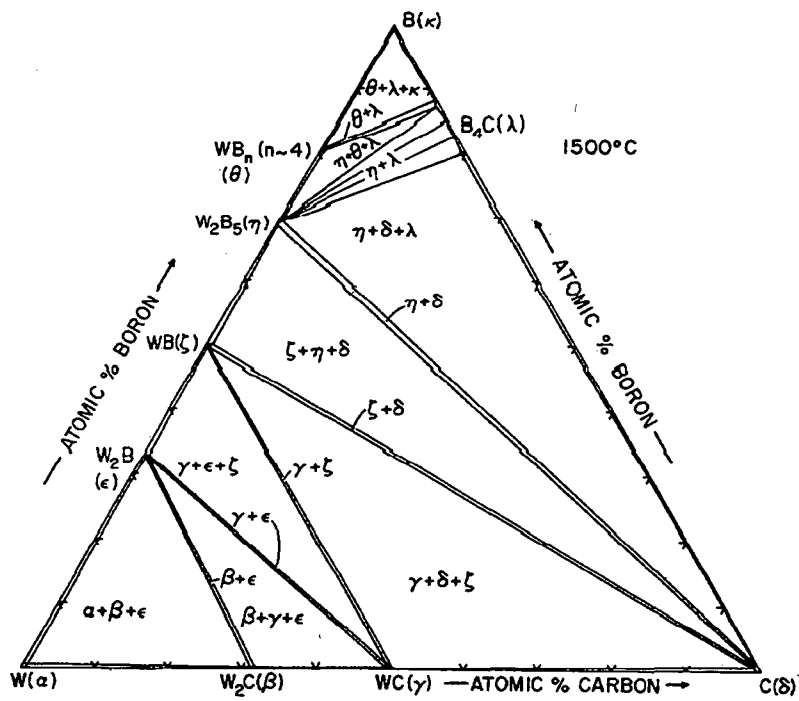

Fig. 4. Experimental ternary phase diagram of W/B/C, after Rudy.[6] 1500°C is the lowest-temperature isothermal section available - kinetic barriers are large because of the high melting points of all constituents.

References

[1]D. G. Stearns, R. S. Rosen, and S. P. Vernon, "Fabrication of high-reflectance Mo-Si multilayer mirrors by planar-magnetron sputtering," Journal of Vacuum Science & Technology A (Vacuum, Surfaces, and Films) **9** (5), 2662-9 (1991).

[2]A. F. Jankowski, L. R. Schrawyer, and M. A. Wall, "Structural stability of heat-treated W/C and W/B_4C multilayers," Journal of Applied Physics **68** (10), 5162-8 (1990).

[3]J.B. Kortright and J.D. Denlinger, "Tungsten-Carbon Multilayer System Studied with X-Ray Scattering," presented at the Multilayers: Synthesis, Properties and Non-electronic Applications, Boston, MA, 1987 (unpublished).

[4]Y. Lepetre, E. Ziegler, I. K. Schuller *et al.*, "Anomalous expansion of tungsten-carbon multilayers used in X-ray optics," Journal of Applied Physics **60** (7), 2301-3 (1986).

[5]T.W. Jr. Barbee, in *X-Ray Microscopy*, edited by G. Schmahl and D. Rudolph (Springer-Verlag, Berlin, New York, 1984), Vol. 43, pp. 144.

[6]E. Rudy, *Compendium of Phase Diagram Data* (Air Force Materials Lab. Metals and Ceramics Division, Wright Patterson Air Force Base, Ohio, 1969).

[7]Donald L. Smith, *Thin-film deposition : principles and practice* (McGraw-Hill, New York, 1995).

[8]W. Eckstein and J. P. Biersack, "Reflection of heavy ions," Zeitschrift fur Physik B (Condensed Matter) **63** (4), 471-8 (1986).

[9]J. P. Biersack and L. G. Haggmark, "A Monte Carlo computer program for the transport of energetic ions in amorphous targets," Nuclear Instruments and Methods **174** (1-2), 257-69 (1980).

[10]M.W. Thompson, Philosophical Magazine **18**, 377 (1968).

[11]J. F. Ziegler, J. P. Biersack, and U. Littmark, *Stopping and Range of Ions in Solids* (Pergamon Press, New York, 1985).

[12]Z. Jiang, V. Dupuis, B. Vidal *et al.*, "Improvement of the thermal stability of W/C multilayers," Journal of Applied Physics **72** (3), 931-7 (1992).

[13]E.B. Svedberg, J. Birch, I. Ivanov *et al.*, "Asymmetric Interface Broadening in Epitaxial Mo/W (001) Superlattices grown by Reactive Magnetron Sputtering on MgO (001) Substrates," presented at the Third International Conference on the Physics of X-Ray Multilayer Structures, Breckenridge, Colorado, USA, 1996 (unpublished).

Chapter Three

X-Ray Performance: Peak Reflectivity

The ultimate property of interest in the mirrors in this study is the x-ray reflectivity (at the peak of the first-order interference). Specular measurements with CuK_α radiation ($\lambda = 1.54$Å) are the first and easiest measurements because they can be performed in air with relatively simple equipment, and give a reliable indication of multilayer quality. Measurements at $\theta = 45°$ and 90° incidence (measured to the surface) give the true performance near the conditions in which the multilayer will be used as a polarizing optical element. The results of these two measurements for the range of specimens will be presented in this chapter, to provide the basic information motivating the other studies. Detailed analysis and more sophisticated x-ray scattering experiments will be left to Chapters 6 and 7.

3.1 Experimental

Reflectivity at CuK_α was measured on the rotating-anode source at the Center for X-Ray Optics, LBNL. The source uses a Rigaku RU-200 BEH x-ray generator, in which the rotating Cu anode allows an electron beam current of 200mA at 50kV for a power of 10kW. The anode spot is imaged with a Ge(111) crystal monochromator which has been lapped flat but left unpolished. The mosaic disorder at the surface widens the acceptance angle and gives a greater total flux at the expense of some angular resolution. The beam passes through a 0.5mm slit to reduce its width and is about 0.7mm wide at the sample plane. The scattered beam is collected by a slit at 55cm from the sample, immediately in front of the detector. The detector slit is set at 1.5mm, slightly wider than the beam, giving a measured angular resolution of about

0.05°. Between the detector and the sample, at 25cm from the sample, is a second slit the same width as the detector slit, and collinear with the detector slit and the rotation axis, to eliminate any scattered rays not originating at the sample plane, such as air scatter near the sample. The photons are counted by a Bicron NaI scintillation counter, whose output is screened by a discriminator to remove any extraneous signal such as low-energy inelastically-scattered photons or higher-order radiation passing the monochromator. Two attenuators of 0.001" and 0.002" Mo sheets are available to avoid saturation. The attenuators are inserted and compensated for automatically by the counting software, giving smooth curves through a dynamic range of 8 orders of magnitude. The calibration of the θ and 2θ angles was checked for each sample, and the absolute reflectivity was found by dividing each scan by the maximum intensity of the full incident beam. For scans that were to be analyzed in detail, an offset scan (a θ–2θ scan with θ offset by 0.3°) was collected to measure the diffuse background near the specular reflectivity condition, and this background was subtracted to obtain the true specular intensity.

Reflectivity measurements in the soft x-ray were made at Beamline 6.3.2 at the Advanced Light Source at LBNL. This bend-magnet beamline provides 10^{10}-10^{11} photons/sec/0.1%BW in the energy range 300-900eV used for these measurements. The bend magnet produces a vertical fan of centered on the electron orbit plane, with a range of polarization states of the light varying with the vertical angle. The slits defining the beam were positioned near the center of the fan of radiation so the light used was about 95% s-polarization. Each sample is adjusted to sit at the center of the beam, and the θ and 2θ angles are recalibrated for each specimen at ensure that the entire reflected beam reaches the detector. The energy is selected by a variable line-spacing grating monochromator, with appropriate filters to remove higher harmonics, and the reflected beam is measured as the current from a Si photodiode. The absolute reflectivities are obtained by dividing by the full beam intensity, as in the hard x-ray measurements. The entire beamline and sample are at a vacuum in the mid 10^{-7} torr range or better. Fuller details of the optical performance of this beamline have been published elsewhere.[1]

3.2 Reflectivity Results

Peak CuK_α reflectivities for the full range of periods are presented in Fig. 1. The parameter Γ was adjusted at several different periods to get the best reflectivity, and the data shown give only the highest values obtained for each period. Many of these values have not had the diffuse background subtracted but this generally affects the peak reflectivity by 2% or less of its value. The multilayer periods were determined by measuring the angles of all the Bragg peaks, and calculating a linear regression using a refraction-corrected Bragg equation as described by Kortright *et al.*[2] At the shortest periods only one Bragg peak was available and the Bragg equation was used directly; in these cases the one Bragg angle was great enough that refraction corrections were negligible.

It is clear from the figure that the reflectivity begins to drop severely for periods below about 15Å. Even for perfect multilayers some loss is expected, however, since the reflection is occurring at higher angles where the reflectivity of each interface is lower. Also, with the lower reflectivity at each interface, more layer-pairs are needed to approach the maximum possible reflectivity, while these samples were all fixed at 50 or 100 layer pairs. In order to provide a more meaningful trend we can compare each measured reflectivity to a value calculated for an ideal multilayer of the same structure. In Fig. 1b each reflectivity has been divided by such a calculated value. The details of the calculations are described in Chapter 6. The calculations assume the tungsten-rich layer to be less dense and thicker than the bulk value as described in the Chapter 2. These calculations are necessarily approximate as the density varies somewhat with the period, but it is clear that below about d = 15Å the multilayers are falling far below the expected performance. This must be attributable to a significant deviation from the idealized layered structure.

Representative reflectivity scans showing all the multilayer reflections are shown in Fig. 2. At very small θ the wafer sample does not yet fill the beam and some light misses the sample, so below $\theta \sim 0.5°$ the measured reflectivity is below the true value. Nearer to $\theta = 0°$, the detector has not yet moved out of the direct beam but part of the beam is blocked by the edge of the sample, so the measured reflectivity does not approach unity as it does in theory. The noise near reflectivity of 10^{-8} corresponds to about 0.1cps and is the "dark count" level of the detector, or the counts recorded when the x-ray beam is off. The dark

counts include contributions from electrical noise in the detector electronics and background radiation such as cosmic rays.

For high-order reflections to appear, the multilayer structure must accurately repeat throughout the stack. For example at the fourth-order reflection each multilayer period represents a path-length difference of 4λ, so any inaccuracy in the period has four times the phase effect on constructive interference it would at the first-order reflection. Local inaccuracies such as roughness are more serious in the same way. Alternatively the Bragg peaks can be thought of as intensities of Fourier components of the composition modulation in the multilayer, and the presence of the high-order reflections implies a more square profile with high-frequency components. The reflectivities shown are consistent with high-quality multilayers with sharp interfaces, at least for the longer periods where many reflections are visible. At the shorter periods the high-order reflections are below the noise level of the detector though they may still be present. Detailed quantitative analysis of the reflectivity, addressing the roughness of the interfaces and the shape of the composition profile, is presented in Chapter 6.

High-angle reflectivity scans for two multilayers at the extremes of the d-spacing range are presented in Fig. 3. The Bragg peaks from the multilayers can be seen on the left. The only other peaks present are a reflection from the silicon substrate, which has its (111) planes approximately parallel to the sample surface, and two parasitic peaks from the aluminum sample holder. A wide amorphous "halo" is seen on the upper curve near $\theta = 20°$, representing interatomic scattering. Since W scatters ten times more strongly than B or C at this wavelength, it is by far the dominant contributor to the signal and this feature represents primarily W-W correlations. For this reason it does not appear in the lower scan: taking into account the nominal Γ and the number of periods, the 5.11Å specimen has only a tenth as much W. These results indicate that these multilayers are amorphous over the entire range of d-spacings, in agreement with results from Jankowski[3] at d = 20Å and 40Å.

The peak reflectivities at constant $\theta = 45°$ are plotted in Fig. 4. Fig. 4*b* shows the reflectivities as a fraction of ideal calculated values as in Fig. 1. The calculations take into account the increased thickness of the W-rich layers, as in the CuK_α results, and also the polarization of the incident beam. The calculations also account for broadening of the peaks due to small variations in the period within the stack, which can be fitted approximately from the shape of the peak and will be described in more detail in Chapter 6. The

range of d-spacings for which reflectivities are shown is limited at the low end by the wavelengths available from the beamline. If plotted together the curves in Figs. 1*b* and 4*b* coincide within the scatter of the measurements. This confirms that these multilayers begin to fall substantially below predicted performance near d = 15Å and that, even though it is measured at a much different wavelength where the optical constants of the materials are different, the CuK_α reflectivity is a reliable measure of multilayer optical quality. Fig. 5 shows the actual first-order reflectivity peaks vs. λ for the 45° measurements. In this case few higher-order peaks are available so the regions away from the peaks are not of interest. Few comparable measurements are described in the literature but the reflectivity at d = 25.2Å can be compared to a value of about 3% published by Seely *et al.*[4] for a W/B_4C multilayer of 100 periods.

Finally, the normal-incidence reflectivities for the same specimens are shown in Fig. 6. Because of the width of the detector the highest incident angle available is actually 85° but angles within 5° of the perpendicular are commonly reported as normal incidence reflectivities. Values from the literature for W/B_4C multilayers by Gutman[5] are included on the graph for comparison. The higher reflectivity measured by Gutman may be attributable to the much lower sputtering pressure used: 1mtorr instead of 2.5mtorr used in this study.

3.3 Blue Multilayers

Several short-period W/B_4C multilayers, made for use as polarizers before this systematic study was begun and stored in air for several months, were found to have taken on a brown or deep blue color, in fuzzy-edged regions covering the wafer area but often darker at the edges. Though no reflectivity measurements were made before and after, it was clear from their performance as polarizers that the average d-spacing had not changed substantially and no gross loss of reflectivity had occurred. One of the tungsten oxides, W_2O_5, is known as "mineral blue" for its color and it is plausible that oxidation of the top few W layers formed this oxide and gave the blue color. The oxidation must not have penetrated deep into the stack, however, since it is unlikely that such oxidation could occur without affecting the period. Because of this experience the multilayers in this study were stored in small vessels evacuated with a mechanical pump. No blue color was found on any of these specimens up to 18 months after they were

made. Since their reflectivities were also stable over several months it is reasonable to conclude that no substantial oxidation occurred.

3.4 Motivation for Further Study: Understanding Microstructure Limits on Performance

It is clear that W/B_4C can form multilayer structures down to extremely short periods. The thinnest multilayer found here, 4.7Å, is the shortest period ever presented in the literature, to this author's best knowledge. This distance is little more than the combined diameters of one W atom and one B atom, yet the x-ray peak widths imply that strong long-range order still exists over many periods. The data raise two deeper questions: What is the atomic-scale microstructure of the short-period multilayers - to what extent can they retain a layered structure, without epitaxy, when the layers are of atomic dimensions? And what is the ultimate mechanism limiting reflectivity at these short periods? The rest of the experiments set forth in this work attempt to answer these questions.

3.5 Possible Mechanisms Limiting Reflectivity

Reflectivity at an interface depends on the optical contrast between the materials and the abruptness of the interface. In seeking to explain the loss of reflectivity we must look to mechanisms that can degrade either of these. Alternatively, with the period being of atomic dimensions but without epitaxy to assist in precise placement of the atoms, it is reasonable to say the layered model must break down and the multilayer must be considered as a composition modulation in a single thick amorphous film. In this case the reflectivity depends on the amplitude of the modulation, analogous to the optical contrast in the layered-structure case. We may consider three mechanisms that can degrade the "squareness" or the amplitude of the composition modulation: *interdiffusion* of the two materials, *roughness* of the interfaces (either intrinsic to the layers or replicated from the substrate), or *discontinuity* of the layers from incomplete layer growth.

The first multilayer structures detected with x-rays[6] lost their measurable reflectivity in a few months because of interdiffusion, and, as described in the Introduction, multilayers have often been used to

study diffusion. The diffusivity in multilayers is usually non-linear, because the steep concentration gradient makes the diffusivity sensitive to the changing local chemical environment and therefore concentration- and time-dependent. Nevertheless estimates of the diffusivity are useful. The diffusivities in this system are expected to be very low at room temperature, because the reactivity of W with B and C tends to stabilize the structure and reduce the free-energy gradient that drives diffusion. This is borne out by the annealing study of Jankowski[3] which found in one case an increase in reflectivity of a W/B_4C multilayer after annealing at 500°C, indicating that other thermodynamic effects were drowning out any interdiffusion. Nguyen[7] compiled experimental diffusivity values in a study of W/C and WC/C multilayers, among others. Extrapolating from measurements at 1200°C to 1600°C, the room-temperature diffusivity of C in W is about 10^{-34} cm^2/sec, with W in W and W in C expected to be still lower because of the large size and mass of the W atom. This is probably a reasonable estimate for B as well, because of the similar size of B and C and the similar chemical interactions in the B-W and C-W systems. Using a characteristic diffusion distance of $x = 2\sqrt{Dt}$ this gives x = 10^{-14}cm, or 10^{-6}Å, for a time of 1 year. A second measurement of the CuK_α reflectivity of a 5Å multilayer about a year after it was made showed no significant loss of reflectivity, indicating that room-temperature diffusion is a negligible factor in this system. Intermixing during growth, from energetic collisions in the sputtering process, as described in Chapter 2, is a significant effect, and its contribution will be considered more thoroughly in Chapter 6.

Roughness will reduce reflectivity for the same reason as interdiffusion - when averaged along the plane of the layers it presents a less abrupt interface which reduces reflectivity. In addition it presents regions of the interface meeting the beam at different angles than the layer as a whole, producing diffuse scattering. Roughness in multilayers is expected from many sources. The silicon substrate has some roughness despite its high polish. This value is often quoted as 0.5Å rms or less by the manufacturers, as measured by optical profilometers, but measurements more sensitive to the higher spatial frequencies, such as scanning-probe microscopes or x-ray scattering, put the figure closer to 2.5Å-3.5Å. Much of this is of spatial wavelengths still large compared to the layer thicknesses and to the diffusion distances of the energetic adatoms arriving on the growing film, so much of this roughness is expected to be replicated by the growing multilayer. Also, the layers themselves have roughness, from shot noise of the growing film, shadowing effects in sputtering, and in many cases crystallinity. In crystalline multilayers, faceting and

grain-boundary grooving in the grains themselves can contribute to roughness, and the crystallinity also allows the multilayer to respond to thermal or growth stresses with slip or twinning on primary shear planes, producing faulting at the interfaces. This effect has been investigated by Cao.[8] In the case of amorphous multilayers, these mechanisms are not available and any strain is probably accommodated elastically. No evidence of such deformation was found in the TEM images.

A meaningful measurement of roughness is generally not a simple matter, because the roughness exists over many orders of magnitude of spatial frequencies. A given measurement is sensitive to a limited frequency range and will give a value of roughness for those frequencies, which may not be comparable to values measured over different ranges. The different results for substrate roughness cited above are an example of this. A way of representing the roughness that is more meaningful than a single number is the power spectrum of the surface, which gives the "power" (proportional to the square of the amplitude) as a function of spatial frequency. For many rough surfaces in nature a simple power-law spectrum of the form

$$S(f) = \frac{K_n}{f^n} \tag{1}$$

describes the roughness over a wide range of frequencies. The decrease of S(f) with increasing frequency reflects the lower height of roughness features at shorter spatial wavelengths, and for certain ranges of the exponent n this power spectrum represents a fractal surface with geometrically similar features at all size scales. Using the power spectrum different roughness measurements can be compared because they represent known frequency ranges of the power spectrum. A detailed characterization of the roughness of these multilayers and its effects on x-ray reflectivity will be presented in Chapters 6 and 7.

Finally, for films a few atoms thick or less, it is common that the films do not yet cover the substrate but still have an island structure or incomplete layers. While from an x-ray standpoint this has the same effect as roughness, it will be considered separately here because it has a different origin from the sources of roughness mentioned above. In the thin film literature the problem is generally divided in two cases depending on the bond energies involved. When the cohesive energy of the atoms in the film to each other is greater than the adhesive energies of the film atoms to the substrate atoms, the film undergoes *island growth* and forms out of islands which become many atomic layers thick before eventually

coalescing. When the adhesive energy is greater, the film forms regions only a few atomic layers thick, which quickly cover the substrate and become continuous (*layer growth*). W/B_4C is a good candidate for this growth mode, since at equilibrium W will react with B_4C to form borides and carbides, and therefore the growing film of one material on the other will find it energetically favorable to bond with the film beneath rather than form its own islands. Even in layer growth, though, there are necessarily discontinuous films in the early stages. Evidence for such discontinuity will be presented in Chapters 4 and 6. In later chapters the discontinuous thin layers will be referred to as consisting of "islands" but this will be understood to mean the thin W-rich regions in the layer growth mode.

The remaining chapters will give results of investigations of these multilayers by TEM, various absorption spectroscopies, and various x-ray scattering studies. The goal will be to synthesize the results from each into an understanding of the actual microstructure of the multilayers and the final limits on reflectivity.

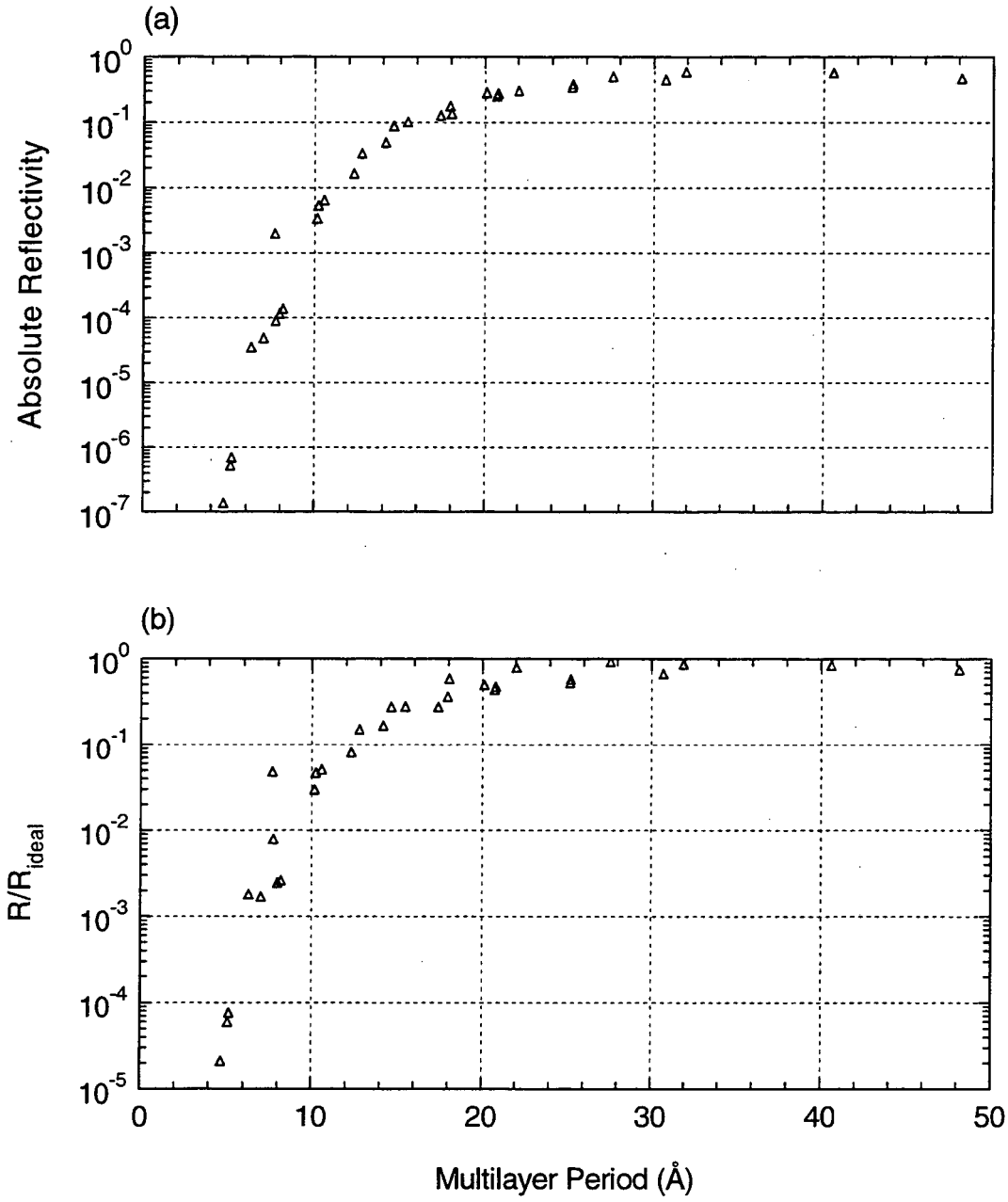

Fig. 1. *(a)* Peak absolute reflectivity at $\lambda = 1.54$Å (CuK_α) for many multilayers. *(b)* Peak reflectivity divided by calculated value for ideal structure. The calculations assume $\Gamma = 0.64$ and a lower density of the W-rich layers as described in the text.

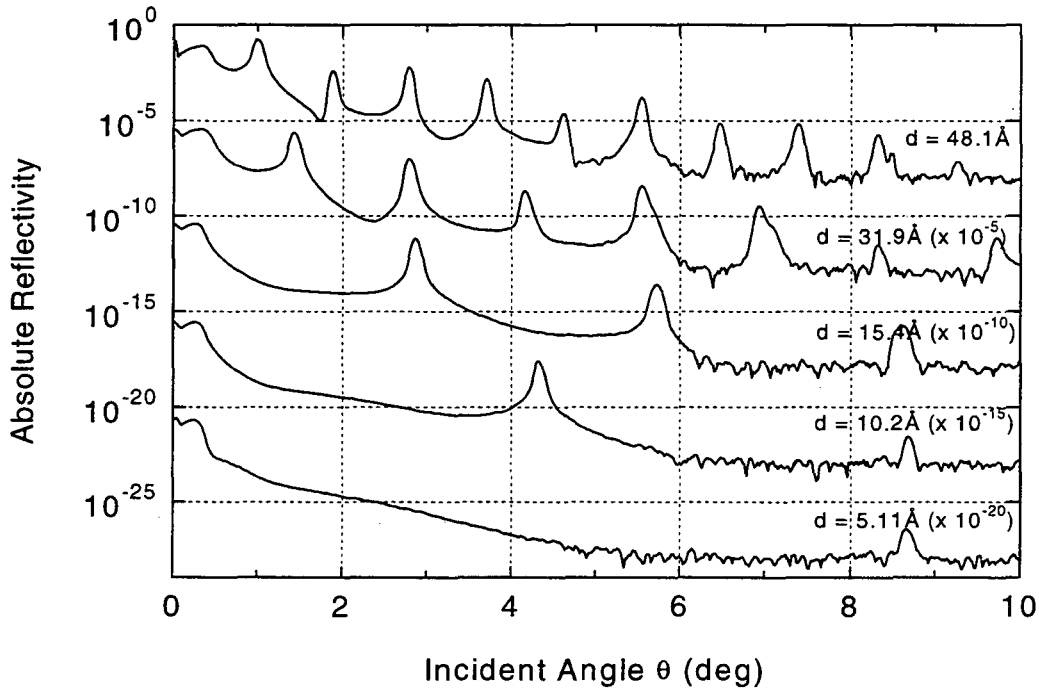

Fig. 2. Absolute reflectivity vs. θ at λ = 1.54Å (CuK_α) for multilayer periods as labeled. Diffuse background has been subtracted. At d = 15.4Å is an example of peaks widening slightly with increasing θ or **q**, indicating some variation of the d-spacing through the stack.

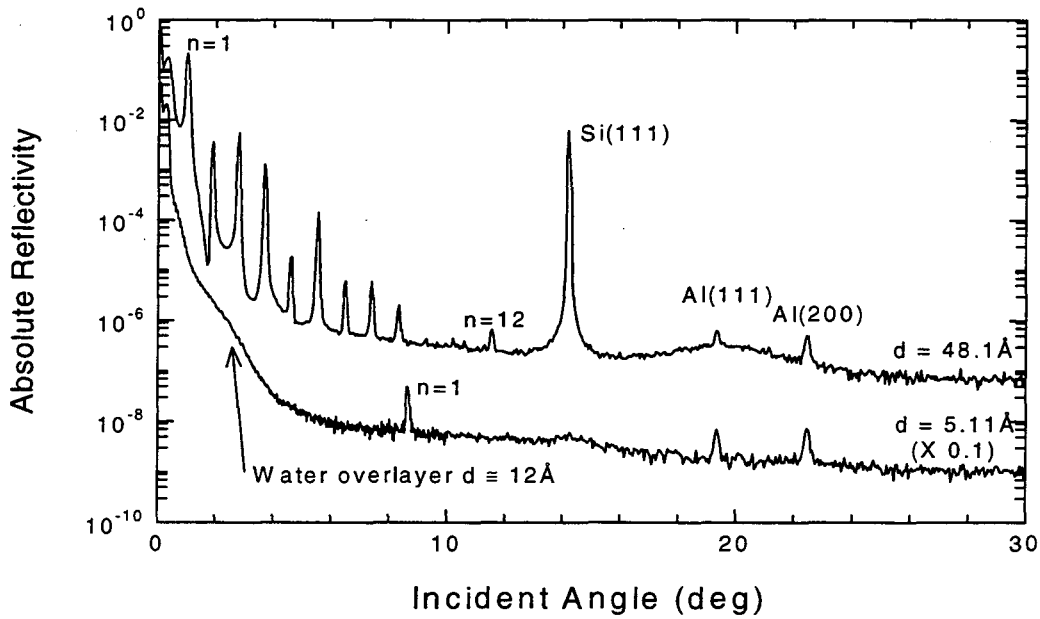

Fig. 3. High-angle x-ray scan on two W/B_4C multilayers, d = 5.11Å and d = 48.1Å, at λ = 1.54Å. The broad feature near θ = 3° is consistent with a thin water overlayer, which has also been observed in a study of bare Si wafers.[9]

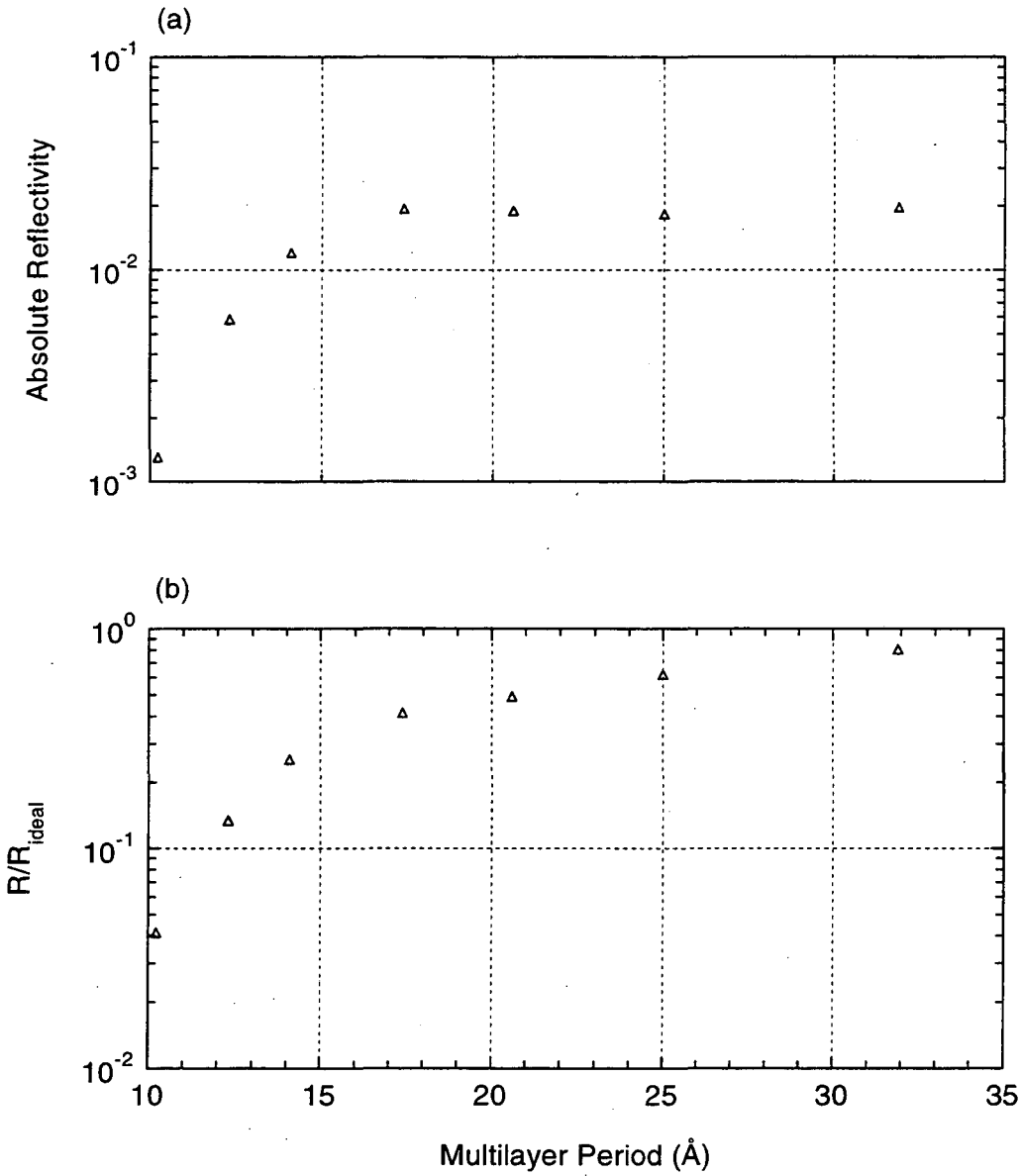

Fig. 4. *(a)* Peak absolute reflectivity at $\theta = 45°$ for several multilayers. (b) Peak reflectivity divided by calculated value for ideal structure. The calculation assumes the same expansion of the W-rich layer as in Fig. 1 and described in the text.

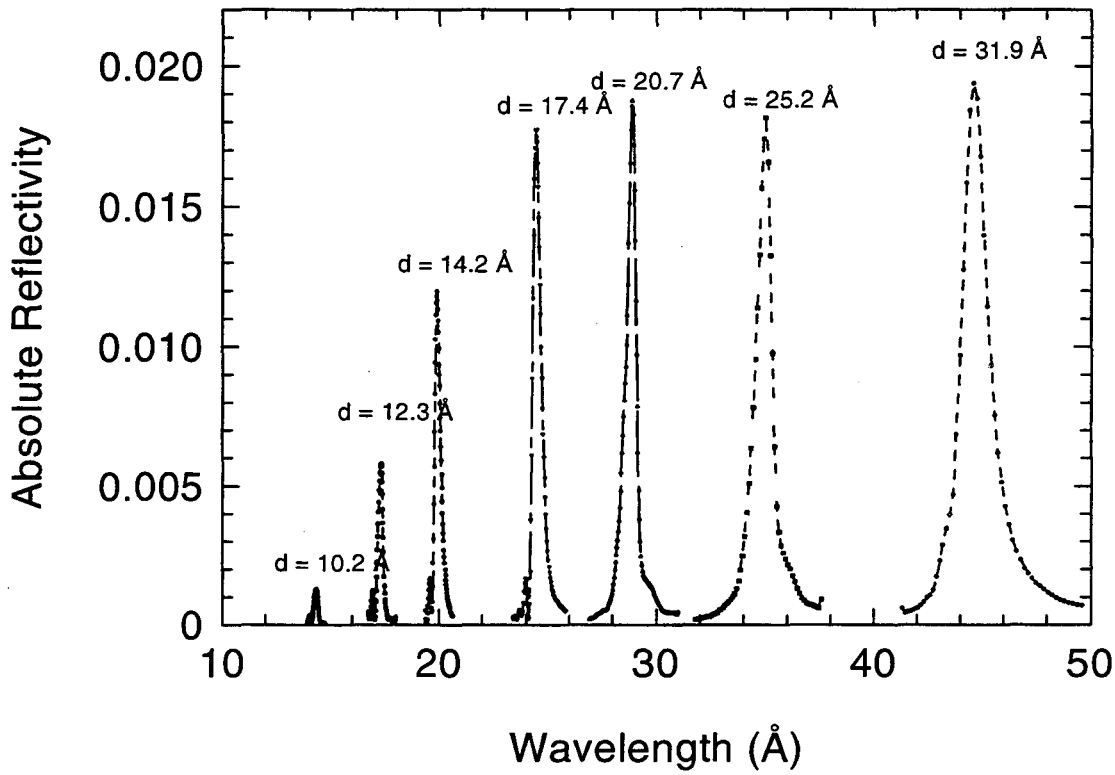

Fig. 5. Absolute reflectivity vs. λ at $\theta = 45°$ for multilayer periods as labeled. Some variation in reflectivity is due to the changing optical properties of the materials.

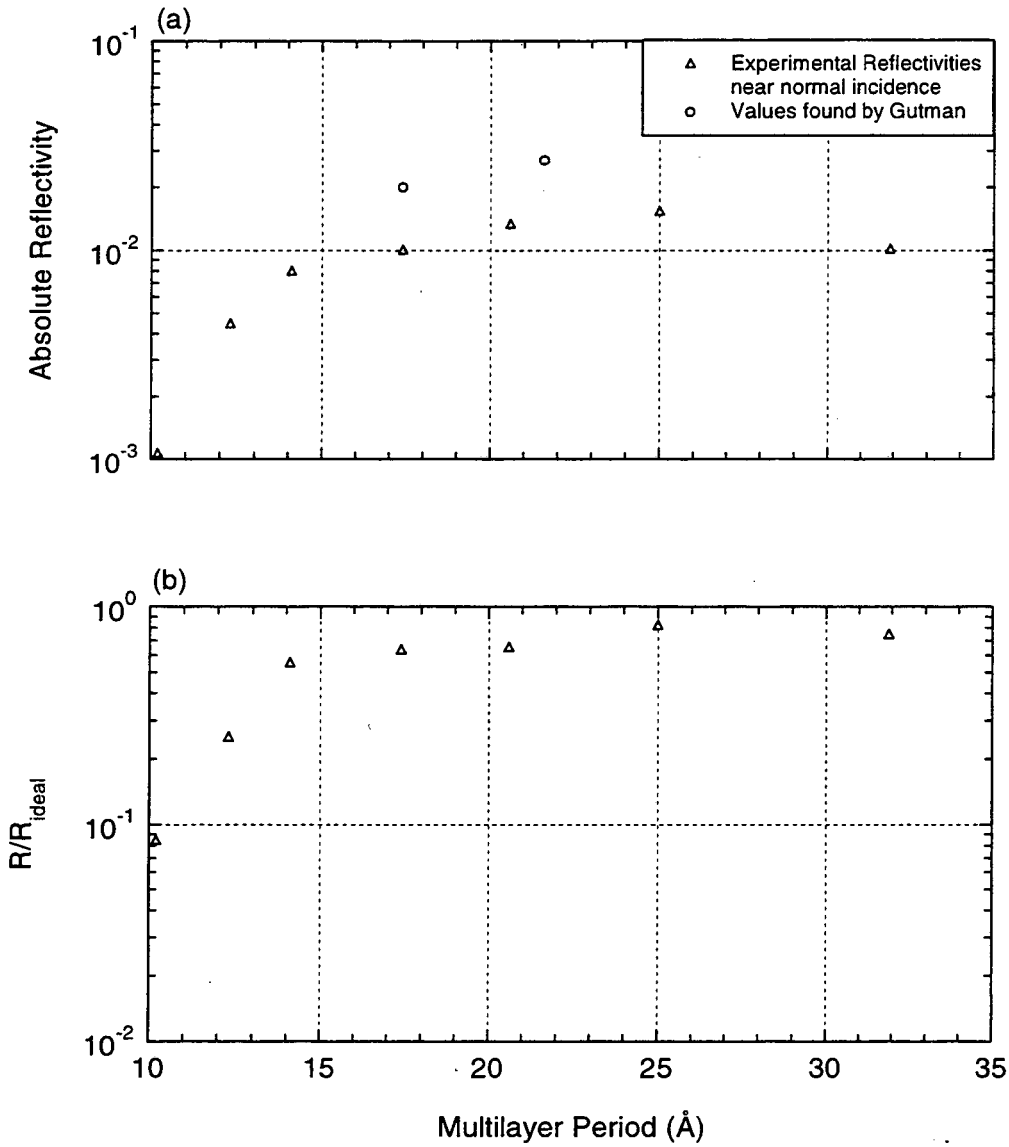

Fig. 6. *(a)* Peak absolute reflectivity at $\theta = 85°$ for several multilayers, with values found by Gutman[5]. *(b)* Peak reflectivity divided by calculated value for ideal structure.

References

[1]J.H. Underwood, E.M. Gullikson, M. Koike *et al.*, "Calibration and Standards Beamline 6.3.2 at the Advanced Light Source," Review of Scientific Instruments **67** (9), (available on CD-ROM only) (1996).

[2]J. B. Kortright, St. Joksch, and E. Ziegler, "Stability of tungsten/carbon and tungsten/silicon multilayer X-ray mirrors under thermal annealing and X-radiation exposure," Journal of Applied Physics **69** (1), 168-74 (1991).

[3]A. F. Jankowski, L. R. Schrawyer, and M. A. Wall, "Structural stability of heat-treated W/C and W/B_4C multilayers," Journal of Applied Physics **68** (10), 5162-8 (1990).

[4]J. F. Seely, G. Gutman, J. Wood *et al.*, "Normal-incidence reflectance of W/B_4C multilayer mirrors in the 34-50A wavelength region," Applied Optics **32** (19), 3541-3 (1993).

[5]G. Gutman, "High-Performance Mo/Si and W/B_4C Multilayer Mirrors for Soft X-Ray Imaging Optics," Journal of X-Ray Science and Technology **4**, 142-50 (1994).

[6]J. DuMond and J. P. Youtz, Journal of Applied Physics **11**, 357 (1940).

[7]Tai Dung Nguyen, "Microstructure-Interface-Property Relationships in Nanometer-Period X-Ray Multilayers," PhD, University of California, Berkeley, 1993.

[8]Wei Cao, "Magnetic properties and microstructures of Ni80Fe20/CoxNi1-xO exchange coupled thin films," Ph.D., 1995.

[9]R. A. Cowley and C. Lucas, "X-ray scattering measurements of silicon oxides on silicon," Colloque de Physique C **7**, 145-52 (1989).

Chapter Four

Microstructure by Transmission Electron Microscopy

4. 1 Introduction

X-ray reflectivity showed clearly that the multilayers deviate strongly from an ideal layered structure at the shorter d-spacings, and that some different effect such as microstructure was coming into play. The transmission electron microscope is a powerful tool to investigate microstructure on size scales as small as a few Angstroms, with both local and area-averaged information.

Many investigators have used TEM to study multilayer microstructure. Nguyen[1,2] has studied the similar W/C and Ru/B_4C systems in detail, on multilayers grown using the same facilities as this study. His W/C multilayers had periods from 10Å to 120Å, and showed crystallinity of the W layers at periods of 70Å and 120Å. Electron diffraction revealed that the crystalline phase was bcc W, though after vacuum annealing for 500°C for four hours a reaction had occurred and crystalline W_2C was present. At the 10Å and 20Å period, however, both materials were amorphous before and after annealing. At d = 10Å the layers appeared to be discontinuous but the effect on absolute reflectivity was not reported. In the Ru/B_4C system the results were similar: the multilayer remained amorphous at the shorter periods (26Å for this system). This was in contrast to the Ru/C system. The 20Å Ru/C multilayer was amorphous in the as-prepared condition, but after 30 minutes at 600°C the Ru layers had agglomerated into spherical particles and crystallized. The phase diagrams reveal that the Ru/B_4C system can form an equilibrium compound, RuB_2, while the Ru/C system is nearly immiscible in the solid state. Nguyen concluded that the ability to form the compound stabilized the layered structure by lowering the mutual surface energies of the two constituents, while the immiscibility of Ru/C raised the surface energy and made agglomeration favorable. The same effect would be expected to stabilize the W/ B_4C system, as W forms compounds with both B and C. More details on the thermodynamics of the W/ B_4C system are given in Chapter 2.

Evans *et al.*[3] have investigated several multilayer systems at short periods by plan-view TEM and have found agglomeration or discontinuity of the layers. For Ni/amorphous carbon multilayers they found a critical thickness of 8.7Å for the Ni layers, below which the multilayer Bragg peaks in the x-ray were split and the Ni layers were discontinuous. In their work the nickel islands were crystalline and atom-layer increments in their thickness could be observed, suggesting a different situation than in W/B_4C where amorphous layers form at any thickness. Nevertheless it is interesting to note that 8.7Å is approximately the thickness of the W layers in this study at the periods where reflectivity begins to fall sharply.

Jankowski[4-8] studied W/B_4C and W/C multilayers at short periods and found a diffraction peak in W/B_4C for periods as short as 6.7Å. He found that a 10Å multilayer had a weakened layered structure but did not comment on the reasons for it. His multilayers were also amorphous in both components and he termed the multilayers "amorphous crystals", since they show long-range order in their composition while having no short-range order in their atomic arrangements. He found that the W/B_4C system formed smoother layers and had greater stability during annealing (at 500°C) than W/C. The W/C multilayers showed crystallization and expansion of the period on annealing, with a resulting agglomeration of the thin W-rich layers as they formed rounded crystallites, where the W/B_4C multilayers showed no phase change and smaller changes in period. Other researchers[9] have observed compound formation in W/C multilayers even without annealing, but no compound formation has been observed in W/B_4C[10,11].
The studies cited generally do not study the very small d-spacings or relate the microstructure to reflectivity over a range of d-spacings. In order to systematically relate the x-ray performance to microstructure several of the samples were examined by HRTEM.

4.2 Experiment

Cross-section and plan-view specimens were prepared as described in Chapter 2. Because of concern about the annealing effects of thinning techniques like ion-milling on very thin multilayers of two materials that react, the specimens were small wedges cleaved directly from the Si substrates, or for plan-view work, free-standing multilayers on a thin carbon underlayer. For plan-view specimens the number of layer pairs was adjusted to give a total thickness of 400-500Å.

While examining multilayers in cross section, it is important that the beam be as parallel to the layer plane as possible. If the orientation of the specimen on the wafer is known, the crystallographic directions in the Si substrate can help this alignment – the (111) wafer has three <110> directions in its surface which can easily be found in electron diffraction. Nguyen[12] describes the use of this technique taking into account the wafer miscut. With the cleavage technique, however, the fragments are so numerous and so tiny that recording their orientation is not practical. Instead, the specimen was placed in the microscope such that the layer plane was within a few degrees of one of the microscope's tilt axes, and the sample was rotated until the layered structure could be seen as far as possible into the thick portion of the sample. This takes advantage of the wedge angle of the cleaved specimens, which is larger than that of a polished and ion-milled specimen and allows a large range of sample thickness to be seen in a small image area. The tilt operation was performed as fast as possible, then further adjustment of the microscope, such as stigmation and focussing, were done with the beam on the Si substrate to minimize radiation damage to the specimen. No beam damage was observed in the microscope, though specimens not examined within a few days of being made showed an amorphous layer at the thin edge indicating some oxidation or contamination occurs in that time.

4.3 Results and Discussion

4.3.1 Cross-section

The cross-section micrographs are presented in Figs. 1 and 2, with magnification adjusted to a common scale. Fig. 1*a* shows d = 31.9Å. The dark layers are the W-rich phase, and some distortion is visible near the thin edge, probably from stress in cleaving the specimen. The most obvious feature is the apparent value of Γ – while the nominal Γ for this specimen was 0.4, an average of several measurements for this sample gives $\Gamma = 0.64$. No internal variation of the layer density is visible, nor is there evidence of a reaction layer as has been observed in some multilayer systems, such as Mo/Si.[13]

The interfaces show some roughness on a size scale similar to the layer thickness. This is expected from thin film growth. [14-16] It is tempting to try to measure roughness from TEM images but this is not an

accurate method in practice. The range of available spatial frequencies is limited by the size of the image (for low frequencies) and the microscope resolution (for high frequencies). The image is a projection through the thickness of the sample, which is at least 2-3 multilayer periods for these specimens, so roughness with spatial wavelengths shorter than this is averaged in projection and cannot be measured. Finally, there is the difficulty of locating the interface precisely. The interface is expected to present a high electron density contrast, which is after all how x-ray multilayer components are selected, so in cross section strong Fresnel fringes will be present. The Fresnel fringe is an optical effect in the shadow of a high-contrast edge, and its importance in TEM examination of multilayers has been discussed by Nguyen[2,12] including theoretical simulations.

There is no evidence of crystallinity, consistent with the high-angle x-ray results which showed no W peaks even up to d = 48.6Å. The electron diffraction pattern also shows only amorphous rings for the multilayer, which must predominantly represent the W-W correlations because of their much higher scattering factor. Several orders of diffraction spots for the multilayer are visible, corresponding to the strong layered structure. The amorphous rings are somewhat narrower in the in-plane direction than the normal direction, indicating more variation in bond lengths in the normal direction and therefore some inhomogeneity in the layer composition. One explanation is a change in density during growth of the W-rich layers, with intermixing at the early stages from implantation of the heavy W atoms and a rising concentration of W with thickness. The amorphous structure of the films is likely stabilized by this intermixing, as B is a common glass-forming element. Covalent compounds are generally vitrified more easily than pure metals as a result of the more directional and localized bonding and consequent lower atomic mobility.

In Fig. 1*b* the d-spacing is reduced to 15Å. There is still a clear layered structure but the interfaces are less distinct. The value of Γ is more difficult to measure but several measurements taken near the edge give $\Gamma = 0.6$. Roughness of the interfaces is again visible on size scales similar to the layer. No strong vertical correlation or "columnar growth" of the layer defects is visible, indicating very smooth layer growth with high mobility of arriving particles, even for these very thin layers. The layers no longer show a very flat interface but have a lumpy appearance with thin regions, consistent with layers that are just continuous. Multilayer diffraction spots are still visible but only for two orders. For this specimen the

diffraction area included the substrate, and the strong crystalline reflections from the silicon overwhelm the amorphous rings from the W-rich layers. A slight tilt of the multilayer spots relative to the silicon reflections results from the miscut of the wafer – the wafer surface is a few degrees off the (111) plane. This miscut is made deliberately by wafer manufacturers to aid in growing devices on the wafers.

Fig. 2*a* shows the d = 10Å multilayer. A weak layered structure is still present but the layers are no longer continuous. A high variation in density is still present, suggesting the loss of reflectivity is not attributable to interdiffusion alone. Several features 10-20Å wide in the plane, consistent with an islanded layer structure, are visible. There is still no columnar growth, even though features from adjacent W-rich layers touch in several spots. Columnar growth has been observed[13,17] in cases of poor surface mobility of arriving atoms during sputtering and is a common source of roughness or low reflectivity. No crystalline reaction phases are visible, such as those Nguyen found in W/C multilayers after annealing. One multilayer reflection is still visible in diffraction, just off the pointer blocking out the transmitted beam (arrow).

Even if the discontinuous growth makes the layer thickness very irregular, it need not destroy the long-range periodicity of the structure. During growth, random variation such as the statistical noise of arriving particles or the growth of nuclei and islands tend to roughen the film, but competing processes, such as the mobility of arriving particles to find minimum-energy positions, tend to smooth the film. Sputtering at low pressures, as has been found to produce the best x-ray multilayers in many systems,[18] encourages this smoothing process by increasing the average energy of the arriving particles. A negative bias on the substrate attracts bombardment by Ar^+ ions from the plasma, which jostles atoms on the surface and similarly assists in growing smooth films.[19-21] If a growing W layer forms an irregular surface with islands, it is energetically favorable for the following B_4C layer to fill in the gaps, leaving a smoother surface for the next W film. As the layers get thinner, the W-rich islands would become smaller in width but likely not shorter in height since they are already near the thickness of minimal coverage. With thinner layers less smoothing can occur between W-rich layers and the islands begin to grow in the wells between the previous layer's islands. This results in more interpenetration of the W-rich layers. In this way the average composition modulation would gradually be weakened while long-range order in the vertical direction is preserved, giving x-ray peaks that are lower in intensity but not broader, and giving a microstructure consistent with the cross-section images here.

Finally, Fig. 2*b* shows an 8Å multilayer. Even though a Bragg peak is still present in the reflectivity results at this d-spacing, no layered structure is visible in the micrograph. This may be because the x-ray measurement has a greater dynamic range in measuring intensities, since it has an attenuation mechanism, than the film does in the TEM. Also, with no layered structure visible during the microscope session, there was no way to be sure of the sample tilt except to use the surface of the silicon substrate wedge as an indicator, so the viewing direction may be several degrees away from the plane of the "layers". This image is consistent with the above model if the layers penetrate each other enough that the average composition modulation is very weak, even though large composition differences still exist locally. In electron diffraction there is no sign of a layered structure, only a streak resulting from the overall shape factor of the thin film.

4.3.2 Plan-view

The plan-view specimens contained at least 13 layer pairs even for d = 30Å, so the full thickness of the specimen would average over many periods and would not show the structure of individual periods. To see this structure better, areas were found where the film had broken and a thinner region near the edge could be examined. Fig. 3*a* shows the d = 30Å multilayer near such an edge. No islanding or discontinuity is visible, consistent with the cross-section image, and there are steps or ledges visible where the film has broken at the layer interface, then through some layers to another interface (arrows). This suggests that the films are stronger than the interfaces and a continuous layered structure is present. The diffraction pattern shows an amorphous structure completely isotropic in the plane, as would be expected since the samples spin rapidly during growth and there can be no epitaxy with amorphous layers. Two clear diffraction rings are visible, much like the rings from the amorphous W-rich layers in the 30Å cross-section diffraction pattern.

Fig. 3*b* shows a multilayer with period 17.4Å. It is similar to the 30Å multilayer but is slightly mottled, indicating uneven layer thickness or small pinholes in the individual layers. This is consistent with the cross-section image at d = 14Å, which averages through the thickness of the sample, making the layers appear more continuous than they really are, but nevertheless shows irregularity in the layer thickness. No

steps are visible, either because the layers are too thin to hold together well or because they are too thin to give enough contrast to see the steps. The diffraction pattern is nearly identical to that at d = 30Å, but the first ring is somewhat wider, indicating a greater disorder of bond lengths and a greater variation in bonding within the film.

Finally, Fig. 3*c* shows a 6Å multilayer. The image shows a clear discontinuous structure, with several islands visible (arrows). The islands are 10-20Å across and irregular in shape, consistent with random growth of a film that is not yet continuous. In the thicker region away from the edge more periods overlap and the individual islands are not visible. The diffraction pattern shows the same isotropic structure but with still greater width of the first ring. The film must now have a greater variation of in-plane distances for W-W correlations, since some are in the middle of an island and some are at the edges, consistent with more diffuse diffraction rings.

4.4 Summary

The W/B_4C multilayers show a smooth layered structure at d = 30Å, but progressively lose the layer smoothness and continuity at smaller d-spacing. Cross-section images show the onset of discontinuity between 14Å and 10Å, while the plan-view images show mottled or barely-continuous layers at d = 17Å. The difference can be attributed to the averaging through the specimen thickness in the cross-section images, which blurs together the features varying along directions in the plane of the multilayers. The microstructure is consistent with a model of incomplete or discontinuous layers below about 14-17Å, with the layers retaining discrete W-rich regions but losing their average layered structure with decreasing period. Even at the very short period of d = 6.3Å the islanded structure is visible in plan-view though no composition modulation is visible in cross-section, demonstrating that complete homogenization has not occurred.

The apparent thickness of the W-rich layers is some 30-40% greater than the nominal thickness expected from the sputtering times. As described in Chapter 2, the expected energies of the much heavier W atoms under the sputtering conditions used are sufficient implant them several atomic diameters into the B_4C layer beneath, causing a churning of the growing W layers. This churning, and the tendency of W to

form stable borides and carbides of lower density than bulk W, explain the observed expansion of the W-rich layers. The W-rich and B-rich layers (or regions) are amorphous at all d-spacings, consistent with the mixing of W into a compound which is stable in the amorphous form. The density of the layers will be considered further in Chapter 6.

No strong correlation of roughness features from layer to layer is seen at any d-spacing, consistent with growth of very smooth layers from the bombardment during the sputtering at low gas pressure.

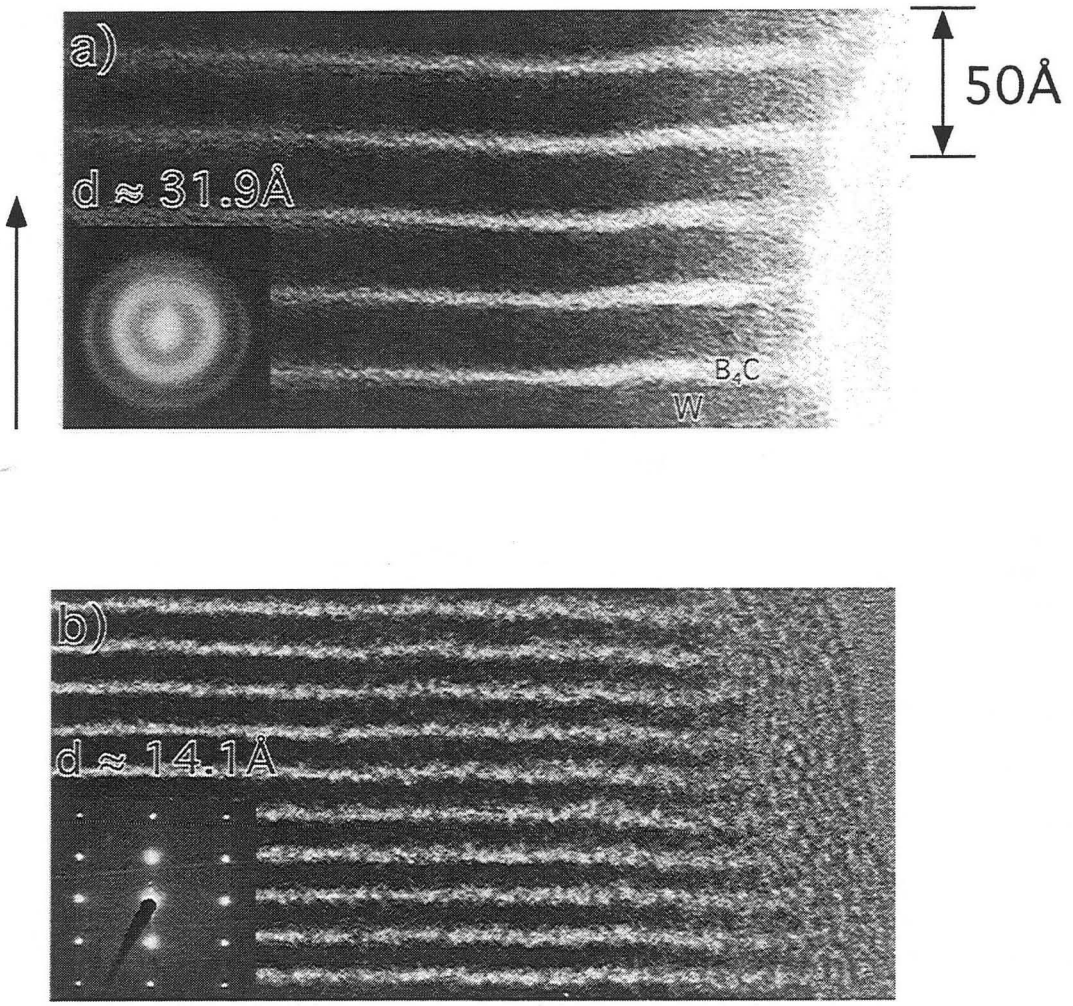

Fig. 1. HRTEM in cross section of two W/B_4C multilayers: *a)* d = 31.9Å and *b)* d = 14.1Å. The arrow at left shows the growth direction. Electron diffraction pattern shows diffuse rings for amorphous W even at the largest d-spacing. Reflections for the multilayer periodicity are visible, and crystalline reflections from the Si substrate at d = 14.1Å.

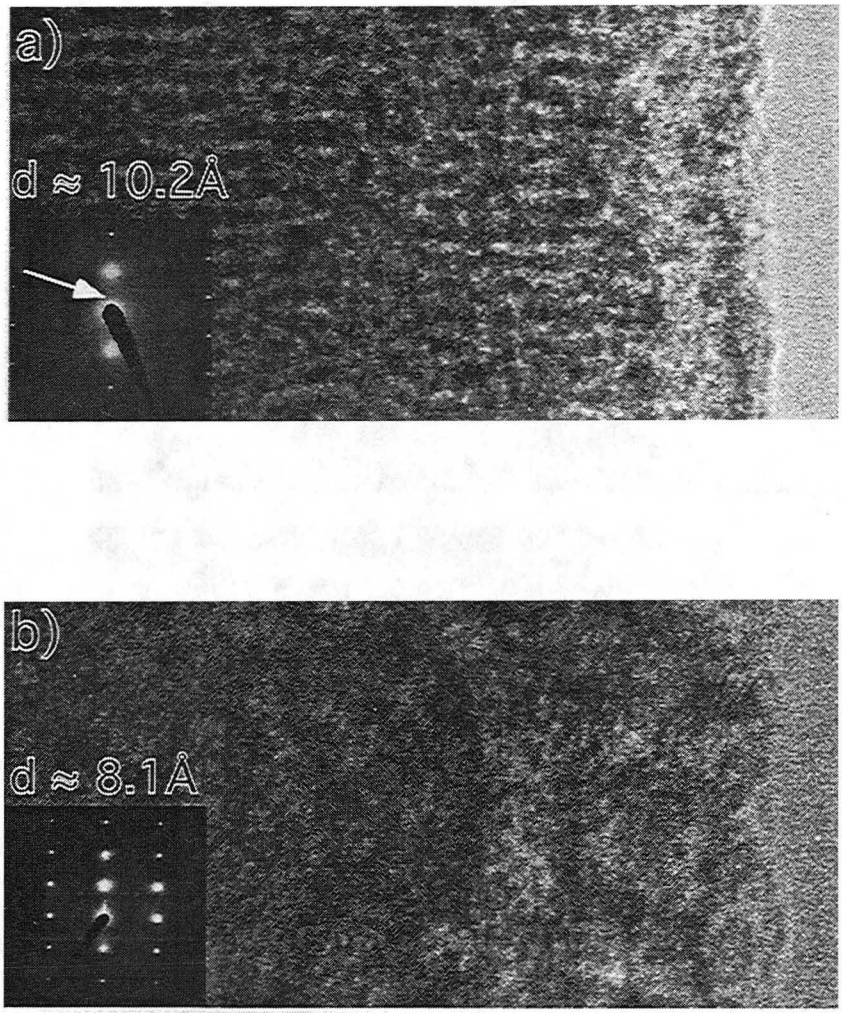

Fig. 2. Cross section HRTEM of shorter-period multilayers: *a)* d = 10.1Å and *b)* d = 8.0Å. Weak periodicity and discontinuous layers are visible at d = 10.2Å, and the white arrow shows the multilayer spot in the diffraction pattern. No layered structure is visible at d = 8.1Å, though Bragg peaks still exist in x-ray reflectivity.

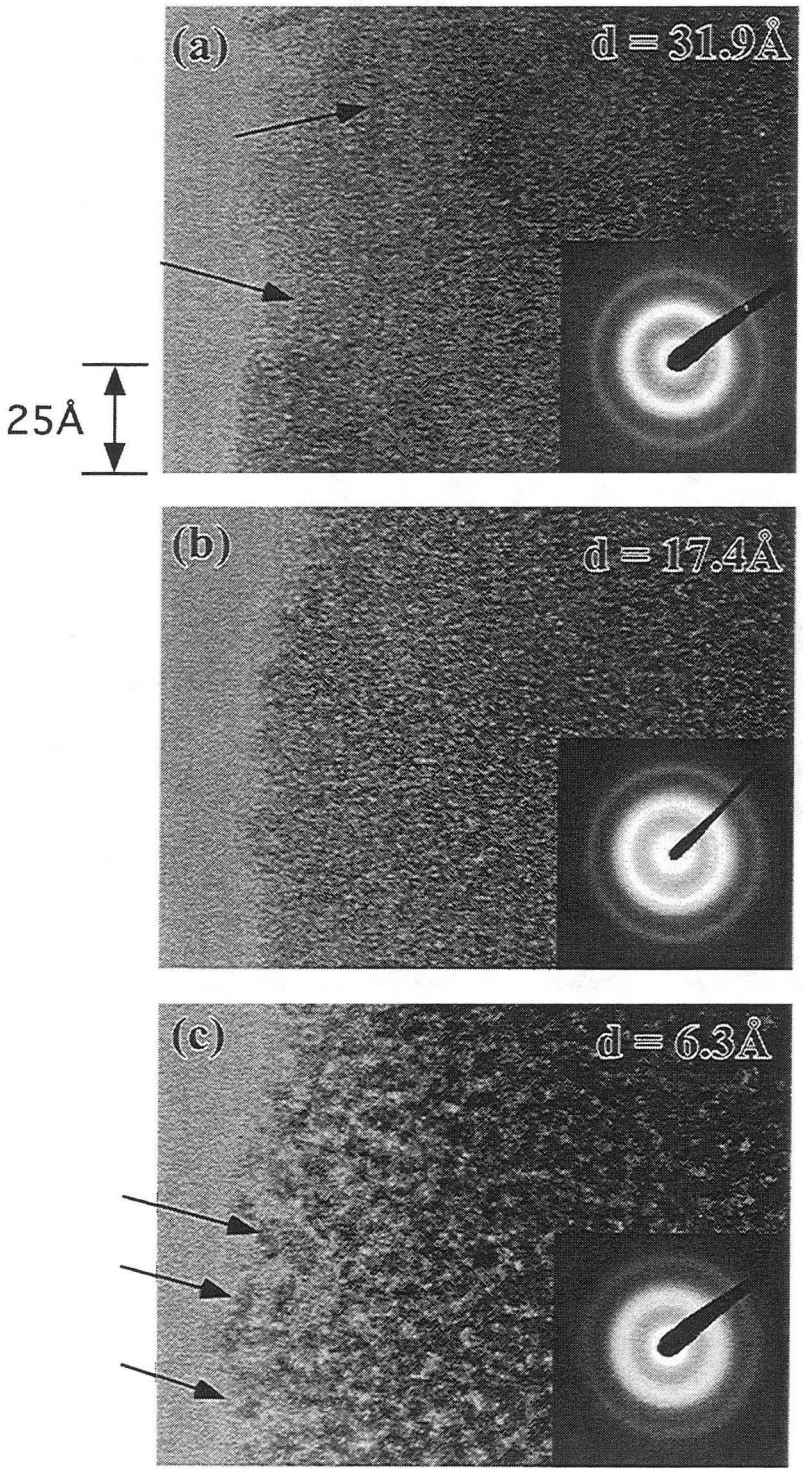

Fig. 3. Plan-view HRTEM of W/B_4C multilayers. Islands are visible from discontinuous layers at d = 6.3Å. Diffuse diffraction rings indicate amorphous W at all d-spacings.

References

[1]Tai Dung Nguyen, "Microstructural and phase stability studies of nanometer period metal/carbon multilayer structures for x-ray optics," MS, University of California, Berkeley, 1990.

[2]Tai Dung Nguyen, "Microstructure-Interface-Property Relationships in Nanometer-Period X-Ray Multilayers," PhD, University of California, Berkeley, 1993.

[3]B. L. Evans, A. I. Maaroof, and S. Xu, "Nucleation and growth of platinum and nickel films on amorphous carbon substrates," Journal of Applied Physics **76** (2), 900-7 (1994).

[4]A. F. Jankowski, L. R. Schrawyer, M. A. Wall *et al.*, "Interfacial bonding in W/C and W/B_4C multilayers," presented at the Topical Conference on Probing the Nanometer Scale Properties of Surfaces and Interfaces, Atlanta, GA, USA, 1988 (unpublished).

[5]A. F. Jankowski, "Short period multilayers: interface-dominated structures," presented at the Special Symposium on 'Interface Science and Technology', Seattle, WA, USA, 1989 (unpublished).

[6]A. F. Jankowski, D. M. Makowiecki, M. A. Wall *et al.*, "Subnanometer multilayers for X-ray mirrors: amorphous crystals," Journal of Applied Physics **65** (11), 4450-1 (1989).

[7]A. F. Jankowski, L. R. Schrawyer, and M. A. Wall, "Structural stability of heat-treated W/C and W/B_4C multilayers," Journal of Applied Physics **68** (10), 5162-8 (1990).

[8]A. F. Jankowski and D. M. Makowiecki, "W/B_4C multilayer X-ray mirrors," Optical Engineering **30** (12), 2003-9 (1991).

[9]A. K. Petford-Long, M. B. Stearns, C. H. Chang *et al.*, "[High-resolution electron microscopy study of X-ray multilayer structures]," Journal of Applied Physics **61** (4), 1422-8 (1987).

[10]F. E. Christensen, Zhu Shou-Hua, A. Hornstrup *et al.*, "X-Ray Study of State-of-the-Art Small d-Spacing W/BC Multilayers," Journal of X-Ray Science and Technology **3** (1-13), 1 (1991).

[11]A. E. Yakshin, I. I. Khodos, I. M. Zhelezniak *et al.*, "Fabrication, structure and reflectivity of W/C and W/B/sub 4/C multilayers for hard X-ray," Optics Communications **118** (1-2), 133-42 (1995).

[12]T. D. Nguyen, R. Gronsky, and J. B. Kortright, "Cross-Sectional Transmission Electron Microscopy of X-Ray Multilayer Thin Film Structures," Journal of Electron Microscopy Technique **19**, 473-85 (1991).

[13]R. S. Rosen, D. G. Stearns, M. A. Viliardos *et al.*, "Silicide layer growth rates in Mo/Si multilayers (for soft X-ray optics)," Applied Optics **32** (34), 6975-80 (1993).

[14]W. M. Tong and R. S. Williams, "Kinetics of Surface Growth - Phenomenology, Scaling, and Mechanisms of Smoothening and Roughening," Annual Review of Physical Chemistry , 401-438 (1994).

[15]D. G. Stearns, "Stochastic model for thin film growth and erosion," Applied Physics Letters **62** (15), 1745-7 (1993).

[16]E. Spiller, D. Stearns, and M. Krumrey, "Multilayer X-ray mirrors: interfacial roughness, scattering, and image quality," Journal of Applied Physics **74** (1), 107-18 (1993).

[17]A. F. Jankowski, "Deposition optimization of W/C multilayer mirrors," Optical Engineering **29** (8), 968-72 (1990).

[18]D. G. Stearns, R. S. Rosen, and S. P. Vernon, "Multilayer mirror technology for soft-X-ray projection lithography," Applied Optics **32** (34), 6952-60 (1993).

[19]E. Spiller, "Enhancement of the reflectivity of multilayer X-ray mirrors by ion polishing," Optical Engineering **29** (6), 609-13 (1990).

[20]E. J. Puik, M. J. van der Wiel, H. Zeijlemaker *et al.*, "Ion etching of thin W layers: enhanced reflectivity of W-C multilayer coatings," Applied Surface Science **47** (1), 63-76 (1991).

[21]A. Kloidt, H. J. Stock, U. Kleineberg *et al.*, "Smoothing of interfaces in ultrathin Mo/Si multilayers by ion bombardment," presented at the 12th International Vacuum Congress, The Hague, Netherlands, 1992 (unpublished).

Chapter Five

Near-Edge Spectroscopies

5.1 Introduction

Evidence from cross-section HRTEM presented in the previous chapter shows that the W-rich layers are some 40% thicker than the nominal values indicated by the sputtering rates, at least for d-spacings of 20Å and 30Å. From arguments presented in Chapter 3, it is likely that this occurs from implantation of the heavy W atoms into the B_4C layer below during growth, resulting in intermixing and an expanded W-rich layer of a lower density than bulk W. It is also known, from the phase diagram of the W-B-C system, that very stable borides and carbides of tungsten exist. If the materials are intermixing on an atomic level some compound must be formed, though it may not be a stoichiometric one. Intermixing would also stabilize amorphous microstructures. The extent of this intermixture must affect the chemical bonding of the W, B, and C atoms, and the study of this bonding may give a measure of the intermixture and a better understanding of the real structure of the multilayers.

Measurements of absorption and scattering of x-rays by materials show absorption edges when the x-ray photon energy reaches the ionization energy for a core electron shell in the sample. While the gross shape of the edge is a jump in the absorption or scattering cross-section at the ionization energy, the excitation is sensitive to the surroundings of the excited atom, and this sensitivity results in a fine structure to the absorption edge whose features can be interpreted.

Two processes commonly contribute to this structure. First, the excited electrons can act as new radiation emanating from the atoms of the excited species, and can be scattered by the surrounding atoms. This adds a signal to the edge absorption curve extending about 50-600eV above the edge, since electrons

ionized with energy greater than the shell ionization can reach surrounding atoms and be scattered by them. This signal is the sum of oscillations from the photoelectrons backscattered by the various neighboring species. These oscillations depend on the bond lengths and can be analyzed for nearest-neighbor distributions about the excited species only, even if many other elements are present. This signal is called the extended fine structure of the edge, and its study, in the case of x-rays, is called Extended X-Ray Absorption Fine Structure, or EXAFS.

In the second process contributing to fine structure very near to the edge (from about 5eV below it to 50eV above), the photoelectron may have only enough energy to reach an empty bonding or antibonding state of the excited atom and its neighbors. In this case the probability of the excitation depends on the number of empty states available at the energy level the electron can reach. The fine tructure on the absorption edge then gives individual features such as sharp or broad peaks, which give information on the density of states at the given energies. The positions of these peaks depend on the surrounding species and the bond energies, since these are bonding or antibonding states. These features are nearer the edge than EXAFS oscillations, so they are called the near-edge structure, and the study of them is called Near-Edge X-ray Absorption Fine Structure, or NEXAFS. This technique can often detect subtle changes in bonding, caused by a change in neighboring species and resulting in shifts of peak energies.

The excitation of core electrons and its sensitivity to the atom's surroundings are largely independent of the method of excitation, so the absorption can be studied by various methods such as beams of x-rays or electrons. In the case of electrons the technique is called Electron Energy-Loss Spectroscopy, or EELS. W/B_4C multilayers have been studied with NEXAFS (by two measurement methods) and with EELS. While no extended fine structure was found, the near-edge structure can be compared between the three techniques. This chapter will present results and analysis of these experiments.

5.1.1 Theory of absorption spectroscopy

Fig. 1 shows a simple schematic of bonding in a diatomic molecule, after Atkins.[1] The 1s and 2s orbitals of the two atoms overlap to form σ bonds, which have rotational symmetry about the internuclear axis. The 2p orbitals also overlap: the $2p_z$ orbitals also have axial symmetry and form the $2p\sigma$ bond, and the

$2p_x$ and $2p_y$ orbitals form $2p\pi$ bonds away from the internuclear axis. The bonds are split into bonding and antibonding states, σ and σ^*, π and π^*, with the energy separation depending on the degree of overlap of the orbitals. There is also hybridization of the $2s\sigma$ and $2p\sigma$ because of their extensive overlap and shared axial symmetry. This gives the hybridized orbitals mixed s and p character and is denoted by the dashed lines. If the two atoms involved were B and B or B and C, a total of 10 or 11 electrons would fill the states up to partial filling of the $2p\pi$ bonds, leaving the $2p\sigma$, $2p\pi^*$ and $2p\sigma^*$ states empty to accept excited core electrons. Of course this is an oversimplified picture for bonding in the compound B_4C but it gives an approximate map of the energy levels.

In Fig. 2 the energy levels are related to the absorption spectrum for an isolated atom and for a model diatomic molecule similar to Fig. 1. In the atom, complete ionization of the s-electron brings it to the vacuum level, where there is a continuum of available states. This level defines the Ionization Potential, or IP, on the absorption spectrum, above which there is a smooth continuum of energies. At lower energies the s-electron can be excited to the various empty states still bound to the atom, giving Rydberg states of well-defined energy appearing as sharp peaks in the spectrum.

When the atom is bound in a molecule, its bonding still includes Rydberg states of well-defined energy below the IP and a continuum above, but the splitting of levels has produced antibonding states, some of which are also above the vacuum level. In this simple case the $\sigma*$ antibonding level is above the IP and gives the broad σ^* feature shown in the spectrum. The breadth of the feature results not from a spread in energy of the σ^* state but from the decay time of the electron from that state. While the matter is not entirely settled in the literature, one model holds that the centrifugal term in the potential produces an energy barrier for electrons decaying from the σ^*. The intensity, position and broadening of the peak depend on the length and energy of the highly-directional σ bond, and to some extent on the atomic number of the other atom. For this reason it is called a "shape resonance" and has been heavily investigated. A thorough review of the literature and theory for the x-ray absorption case is given in the book by Stöhr,[2]including a review of theory on interpretation of the $\sigma*$ feature. The π^* antibonding state also gives a peak in the spectrum. The π^* state is lower energy than the σ^* but gives a sharp peak whose energy is more easily measured and interpreted.

5.1.2 Application

These mechanisms relating the spectrum to bonding are independent of the method of excitation, which allowed different techniques to be used on these specimens. The boron K-edge at 188eV is accessible to electron energy-loss spectroscopy (EELS) and also to soft x-ray excitation at the Metrology Beamline 6.3.2 at the Advanced Light Source, LBNL. The average composition of the multilayers is near $WB_2C_{0.5}$, meaning B is the dominant element in mole fraction and a strong signal can be obtained. It is also reasonable to expect that the bonding state of boron would change if the multilayers became intermixed on an atomic size scale. The carbon K-edge at 284eV is also accessible, though the signal is much lower because of the smaller concentration. The W K-edge at 69.5keV is too high in energy for these measurements, and while the W L-edges at 10-12keV would be of interest because of their allowed transitions (in the dipole approximation) to tungsten's bonding d-states, they are also beyond the energy range of the techniques used here. For this reason these experiments concentrated on the boron K-edge.

Three type of spectroscopy experiments were performed: EELS, x-ray absorption (NEXAFS) measured in transmission, and NEXAFS measured by total electron yield (TEY). The results for each will be presented below.

5.2 Electron Energy-Loss Spectroscopy (EELS)

5.2.1 Experiment

EELS samples were made by the same method as plan-view HRTEM samples, with a copper grid embedded in wax and floated free after deposition. The optimal sample thickness was estimated at 400Å, based on the average composition and known absorption lengths, and the number of layer pairs giving the total thickness closest to this value was deposited, although through a deposition error the d = 18Å specimen was made 500Å thick. Samples were made at three d-spacings covering the range where the greatest change in the intermixing would occur: 6Å, 18Å and 30Å, and as a standard for comparison a

single film of B_4C sputtered from the same source was made, though it was made thicker (600Å) because of the lower density. The samples were stored in vacuum except for the few hours of the EELS session. As an additional standard, a sample of crystalline B_4C kept by microscope support staff was also examined.

The measurements were made on the JEOL 200CX Analytical Electron Microscope at the National Center for Electron Microscopy (NCEM) at LBNL, operated at 200keV by C. E. Escher. After the beam passes through the sample and an aperture which selects a small area of the image for analysis, the electrons are dispersed according to their energy by a quadrupole magnet apparatus manufactured by Gatan Industries. Intensities are counted in parallel by an array of detectors. The main beam, or electrons experiencing no energy loss, was recorded for each specimen. The width of this zero-loss peak also gives the energy resolution of the measurement, which depends on the energy resolution of the incident beam, the defocus condition, and the size of the selection aperture. With the 1mm selection aperture, these measurements gave an energy resolution of 2.2 eV. Since the plan-view specimens were of constant thickness, there was no need to carefully select a thin area for each specimen, although this was done for the bulk B_4C standard.

5.2.2 Data Reduction

The raw EELS spectrum shows an exponential decay with increasing energy loss, representing a sum of many random loss processes, and standing out from this curve are edges or jumps corresponding to atomic absorption by specific elements in the specimen. While the raw data are shown below, to compare the peak shapes better the exponential background was fit over the range before the B edge and subtracted. The height of the jump above the background depends on the concentration of B in the specimen and on the thickness, and for comparison this height was normalized to 1. The curves are then plotted separated by arbitrary additive factors to allow easy comparison.

5.2.3 Results

Fig. 3 shows a typical zero-loss peak. Near the main beam, at an energy loss of ~26eV, the first plasmon peak was also recorded for each specimen. The plasmon is a localized longitudinal oscillation of weakly-bound electrons, and the energy of the plasmon peak depends on the average electron density. A thicker specimen will show a stronger plasmon peak, and possibly 2nd and 3rd plasmon peaks from multiple plasmon excitations. In general, a single plasmon peak less than a tenth the intensity of the main beam indicates a sufficiently thin specimen, whose spectrum will be dominated by single scattering events and can be interpreted directly. If the specimen is too thick, the plasmon peak is added to all the other features as well, obscuring the true absorption spectrum.

The plasmon peak is less than 1/10 the intensity of the zero-loss in Fig. 3, indicating a thin specimen. Fig. 4 shows the raw EELS spectra for the range of energy loss 130-330eV. The range was extended far beyond the B edge to include also the C K-edge (284eV), though the signal there is much weaker because of the lower concentration. Fig. 5 shows the boron edge area with background subtracted as described above, and Fig. 6 the carbon edge area.

5.2.4 Discussion

The B-edge curves are very similar. No sharp features are visible on any of the curves, though a hint of a sharp π^* peak at 193.5 ±2eV can be seen on the bulk B_4C standard (top curve). This tiny feature has a width near the energy resolution of the measurement of 2.2eV. To investigate the possibility that this peak was being obscured by the instrumental broadening, a second set of measurements of the specimens was made on a Phillips CM200 microscope capable of an energy resolution of 1.1eV, but the results were essentially identical and are not presented. The lack of sharp features is consistent with a disordered average bonding environment for B[3]. The possible π^* feature in the bulk B_4C specimen is smeared out in the sputtered film, which is consistent with a greater disorder in the film causing an overlapping of many different bonding states. The multilayers do not show this feature at 193.5eV, but share a small shoulder at 196±2eV, which does not change with d-spacing. It is possible that this is the same feature, because the

EELS measurement has an uncertainty in the absolute energy due to drift over time of the magnetic field which spreads the beam over its energy range. Further interpretation of this feature will be given later with results of the other techniques.

The broad σ^* feature shows little change from the B_4C specimens to the multilayers, though in this the error in thickness of the d = 18Å specimen becomes apparent. A thicker specimen tends to obscure features in the spectrum, and this is apparent in the lower jump ratio of the d = 18Å specimen, as seen in the raw EELS curves in Fig. 4. However, the 6Å and 30Å curves are almost identical, indicating very little change through the range in which the multilayers go from disconnected islands a few atoms thick to a continuous layered structure.

The position of the σ^* feature is a sensitive measure of the bond length, though it is less sensitive when high-Z elements participate in the bond. In this case no shift in position is visible, even if the curves are superimposed. However, the uncertainty of the energy normalization in the EELS measurements makes this interpretation difficult, and it will be considered again in the x-ray measurement in the next section. Further interpretation of these results can be made, taking into account the results of the other techniques and work in the literature using them. The evidence thus far indicates a more disordered structure about the B atoms in the multilayers than in the bulk B_4C, but a very similar average bonding environment for the B atoms in all three multilayers. Evidence from the other spectroscopy techniques will now be presented, and the results interpreted together.

5.3 Near-Edge X-ray Absorption Fine Structure (NEXAFS)

5.3.1 Introduction

NEXAFS is the study of fine structure features near an x-ray absorption edge, resulting from changes in the bonding of the target atom to surrounding atoms. Unlike EELS it is usually measured with a tunable x-ray source, but aside from this the meaning of the experiment is the same, as the same electronic transitions are being excited. The x-ray energy is increased, crossing the absorption edge, and the absolute or relative absorption of the specimen is measured. In the same way there is a general exponential

background representing the gradual decrease of the scattering factor with energy, above which absorption edges for particular elements can be measured.

5.3.2 Experiment and Samples

For these experiments W/B_4C multilayers were grown on membranes of Si_3N_4, on silicon frames, which are produced by standard microfabrication techniques at LLNL. The membranes are about 1200Å thick with a free area of 3mm x 3mm and initially appear flat to the eye. From the average composition of the multilayer, calculations of the absolute absorption near the B edge were made, in order to choose a thickness such that the drop in transmissivity at the edge would be near $1/e$, and to give a sufficient signal/noise ratio. The total thickness of the multilayers was 1500Å, and specimens were made at 6Å, 14Å, 22Å and 30Å, and a single film of B_4C as a standard. After deposition the membranes were somewhat wrinkled, indicating that the multilayers and the B_4C film had a compressive stress. The sputtering conditions were identical to those used for the other multilayers, described in Chapter 2.

Measurements were made at the ALS Beamline 6.3.2. The beamline has a variable-line-spacing grating as a monochromator, whose higher harmonics had to be removed. This was done with a triple-bounce order-sorter of Ni, Ni and Si surfaces at 10°. This device takes advantage of the wavelength dependence of the critical angle for total reflection to remove higher-energy harmonics, which have a smaller critical angle and are not reflected. Before each measurement the calibration of the monochromator was checked at its "zero-order" peak. Because of the excellent collimation of the incident beam the energy resolution of these measurements is better than 0.1eV. The samples were translated carefully in the plane normal to the beam to ensure that the beam struck only the membrane, and the signal collected by a Si photodiode detector behind the sample. The beam energy was scanned through the B edge, taking three 1-second measurements at each step and 5 steps per eV energy. At each energy, the photoelectron current from one of the beamline's focussing mirrors was recorded as a nominal I_0, and after each measurement of transmission through a specimen the intensity of the full beam was recorded in a separate scan over the same energies. The beamline sample chamber was evacuated to 8×10^{-7} torr or better before measurement.

5.3.3 Results and Data Reduction

The absorption measurements at the synchrotron are subject to two normalizations. First, as the electrons in the ALS storage ring gradually lose energy, the overall beam intensity decreases, and this effect must be divided out to compare scans taken at different times or as a function of time. Second, to obtain the absolute absorption the intensity passing through the sample must be divided by the full-beam intensity over the same range of energies. For the first normalization, the intensity at the detector was divided through by the nominal I_0 signal from the beamline M3 mirror, both for the signal that passed through the sample and for the full beam, to divide out the gradual decrease of the beam intensity with time. Then the sample signal was divided by the full beam to obtain the absolute intensity I/I_0. Since transmission NEXAFS is a direct absorption measurement, the signal to the detector decreases when the photon energy reaches the B edge, unlike the EELS signal which shows the edge as an increase. In order to show the edge as an increase for comparison the absorption length $\mu t = -\ln(I/I_0)$ was calculated for each sample. The absorption length shows a gradual exponential decrease, representing the decrease of the average atomic scattering factor with increasing energy, and the absorption edge rises above this background. As with the EELS results the background was fitted and removed. Fig. 7 shows the background-subtracted NEXAFS spectra for the four multilayers and the B_4C film. The curves have been vertically offset in decreasing order of thickness of the B_4C films within. In this case the signal at the C edge was poor and was not recorded.

5.3.4 Discussion

The spectra are similar in their general features to the EELS spectra. No sharp peaks appear in any of the curves, though in this case subtle trends are visible with d-spacing. The σ^* feature shows a change of shape with decreasing d-spacing, from an apparent two-lobed hump for the pure B_4C film to a narrower hump for the 6Å multilayer. The interpretation of the width is complicated, even in the case of better-defined specimens like organic molecules where the bonding environment of a particular species is more uniform. In the model of widening of the σ^* by trapping of the photoelectron by a centrifugal barrier, the

width depends on the decay time of the quasi-bound state of the photoelectron, and is asymmetrically broadened by variation in the bond energy from atomic vibrations. A calculation of the shape of the σ^* peak for various bond lengths, for the simple case of the N_2 molecule is given by Dehmer.[4] In the case of a disordered bonding environment of unknown average composition the problem is not tractable theoretically. However, a systematic trend can be observed, with the 30Å multilayer retaining a shoulder of the higher-energy hump shown by the single B_4C film, which disappears as the d-spacing decreases, consistent with a gradual change from bonding similar to bulk B_4C to a different bonding state.

A small shoulder or peak also emerges at about 192eV. This feature becomes stronger in the multilayers as the d-spacing decreases, as can be seen by comparing the intensities for the four multilayers at E=192eV to the flat intensity below the edge at 186eV. The single B_4C film does not fit the trend as it shows this feature more strongly than the thickest multilayer, though the boron features are stronger in general in the curve for the single B_4C film and this may be an artifact of the normalization of the curves to have the same height after the edge. A study of energy loss of inelastically scattered x-rays by Manninen[5] found a similar shoulder in elemental B and identified it with a π^* state not strongly resolved from the edge structure.

Bullett[6,7] has studied the structure of boron and several of its compounds with electronic structure calculations. Pure B, like many of its compounds, has a complicated structure, often based on B_{12} icosahedra. B_4C has a rhombohedral lattice decorated by B_{12} icosahedra, where the C atoms inhabit three-atom B-C-B chains in the octahedral interstices and substitute for B in the B_{12} clusters. Bullett's calculated density of states for B shows a sharp peak just above the conduction band, corresponding to 192eV in these measurements. The calculations indicate that the peak corresponds to a π^* state in the B_{12} clusters, and should occur in B_4C as well since the same B_{12} clusters are present. Interpretation of why this peak is stronger for the shorter-period multilayers could be aided by comparison with a film of WB or WB_2, since the effect of adding W to the boron bonding environment is not known. However, a thin film specimen would be needed while no WB sputtering target was available.

A third systematic change can be seen in a weak pre-edge feature just at the initial rise of the absorption. This region of the spectrum has been expanded in Fig. 8*a*, with the derivative plotted in Fig. 8*b*. The weak feature appears at about 188.2eV as a shoulder in the absorption curve, and can be seen in the

derivative as a peak. The region where the feature decays at 189.2eV is a dip in the derivative. As the d-spacing increases this feature and the changes in slope associated with it disappear, and this trend continues through the single B_4C film (top curve). A feature before the edge represents an electronic transition to a state close to the Fermi energy. In the case of Cu-Zn solid solutions,[8,9] a similar pre-edge feature is associated with 4s states in Cu left empty by the filling of the 3d shell, and the feature becomes weaker with increasing addition of Zn, in which the 4s state is filled. The 1s-4s transition is not allowed in the dipole approximation, but the peak still appears in the K-edge spectrum. Various theoretical interpretations are possible, such as some "p" character in the 4s shell caused by hybridization, or a quadrupole interaction. In the case of these multilayers, B and W do not have such similar electron configurations as Cu and Zn, and an interpretation along these lines would require more detailed information such as a band-structure calculation for crystalline WB or WB_2. The weak appearance of a forbidden transition to an empty W 5d bonding state is a reasonable hypothesis.

The NEXAFS results show systematic changes in boron bonding with decreasing d-spacing, with the bonding becoming less similar to that in B_4C. There is increasing strength of a π^* feature at 192eV and a pre-edge feature at 188.2eV, and a narrowing of the σ^* feature. Further interpretation will be given in a general discussion of the three techniques.

5.4 X-Ray Absorption by Total Photoelectron Yield (TEY)

5.4.1 Introduction

This technique consists of making a NEXAFS measurement but using a different method of collecting the signal. Instead of measuring the absorption of the specimen in transmission, the specimen is electrically isolated and attached to a sensitive ammeter. Since the electrons excited from the k-shell are ionized to the vacuum level, they are freed from the boron atom. If the excited atom lies near the surface, the electron has some chance of escaping the sample entirely. If this happens the sample acquires a net electric charge, which the ammeter will neutralize and record as a current. In absorption spectroscopy by

total yield the beam energy is scanned through the absorption edge as before and the photoelectron current is recorded at each energy.

5.4.2 Experiment

These experiments were set up at the Metrology Beamline like the previous NEXAFS work, but the slotted aluminum plate holding the specimens was insulated from the holder in the sample chamber. The holder was connected to a Keithley pico-ammeter with a shielded cable, by way of a feed-through in the chamber walls. To improve electrical contact between the samples and the aluminum plate, the samples were fixed to the plate with a stainless steel slat as usual, but a small dab of a conductive paint containing silver particles was applied to the edge of the slat and the sample. With this arrangement a clean signal was attainable even for the highest gain settings of the ammeter. As with the previous absorption measurements, the signal from the beamline mirror was recorded as a nominal I_0 to normalize for the change of intensity with time. For this measurement the full intensity of the beam was not recorded since no "absolute" measurement is meaningful in this case. The measurements of the full beam from the absolute absorption experiments show that the intensity of the beam itself has little structure in the range 170-230eV.

5.4.3 Results

The total yield absorption scans are plotted in Fig. 9. As with the previous results the background has been subtracted to isolate the boron data, and the heights after the B edge normalized to unity. In this case the current measured by the ammeter is a direct measure of the absorption so the current itself was plotted.

5.4.4 Discussion

The results are quite different from the previous two techniques, in that sharp absorption features are now visible above the IP, even though the scans are on the same specimens as the above NEXAFS

measurements and were taken in the same session. Two sets of peaks are visible: one at 192.3eV and one at 193.8eV. The smaller peak, at 193.8eV, increases slowly in intensity as the d-spacing shrinks, the trend including the single B_4C films as well. The larger peak also becomes taller through the range of specimen thicknesses. The broad σ^* feature is still present and shows a similar slight broadening with increasing d.

These results can be compared with those published by Jia *et al.*[10] Their results were measured by the same total-yield technique on the Metrology Beamline on a variety of boron compounds. A figure from their work is reproduced in Figure 10. For their B_2O_3 specimen, the only feature is a strong peak at 193.8eV, indicating that a peak at this energy comes from a π^* state in B_2O_3 and that the peaks at this energy in this study may be a surface oxide. The other peak at 192.3eV occurs in Jia's results for the B_4C sputtered film, but not for bulk B_4C. The powder specimen was bulk B_4C though it is labeled as B_4C_6 in the figure.

The total-yield NEXAFS technique is often used in absorption spectroscopy because the experiment is simpler to set up than transmission NEXAFS – there is no need to fabricate a thin film specimen of the proper thickness, but bulk specimens can be used instead. However, the results become more difficult to interpret, because the signal is only recorded when the photoelectrons escape the sample. The signal includes all electrons leaving the sample: photoelectrons and Auger and secondary electrons. The energy of these electrons follows a distribution depending on the excitation processes, but it is dominated by a low-energy tail of secondary electrons, with energies below about 20eV, from inelastic scattering in the sample. Since these electrons have very small escape depths from a few atomic layers to 50Å, the majority of the signal is highly surface sensitive. This likely explains why this peak appears in all of the specimens in this study in the TEY results but in none in the EELS or transmission NEXAFS results – the samples all have an oxidized layer near the surface. It was previously observed that many W/ B_4C multilayers exhibited a blue color from oxidation of the W, as described in Chapter 2, so it is reasonable to expect some oxidation of the B as well in these specimens, though their exposure to air was limited to a few hours. This also explains why the peak at 193.8eV appears in all the curves in Jia's results, even though the other specimens are nominally oxygen-free.

While no studies in the literature address the peak at 192.3 eV in boron carbide, related work by Chaiken[11] and Terminello[12] on boron nitrides is relevant. They compare absorption spectra of different

structures of BN, and find a sharp peak near 192.1eV for hexagonal and incoherent BN but none for cubic BN. They and previous workers[13,14] have identified this feature with a transition from a σ to a quasi-bound π^* state. If a π^* state exists, there are unhybridized p-orbitals, and the sample has not fully hybridized to sp^3 but still has some sp^2 character, which is a reasonable interpretation in the case of disordered B_4C in a sputtered film as well. However, since this feature does not appear in the EELS or transmission NEXAFS scans it is reasonable to conclude it is also a surface signal. If these are surface states from the top 50Å of the specimens, it is not surprising that they are overwhelmed by the bulk signal from the entire sample thickness (400Å or 1500Å) in the other spectroscopy techniques.

Fig. 11 shows results from Jia *et al.* on three metal borides. All three curves show a peak near 193.9eV, very close to the oxide peak at 193.8eV in Fig. 10 and in the results of this study, suggesting surface oxidation of the specimens is responsible in every case. Of greater interest are the σ^* features in Jia's results, for bonding with three different metals. They are different in shape from those in his B_4C results and in this study, and show greater changes in the feature shape than were seen in the range of samples in this study. For example, the curves for ZrB_2 and TiB_2, which are both high melting-point transition metals, are distinctly different from the curves for B_4C. The σ^* features are narrower, beginning at energies significantly above the ionization edge (near 197eV), and have different shapes. By contrast, the edges found in this study are nearly parallel curves, beginning and ending at nearly the same energies (near 189eV) and showing similar shapes. The lack of large changes in the σ^* feature in this study is consistent with boron bonding in WB that is very similar to that in B_4C and different from that in ZrB_2 or TiB_2, or with only small changes in the degree of intermixture with d-spacing.

Aside from the sharp features, the TEY NEXAFS spectra are quite similar to the transmission NEXAFS spectra. The single B_4C film shows a wide σ^* feature with a 2-lobed shape, though in the TEY case the low-energy lobe is taller. A slight narrowing of the σ^* feature can be measured, similar to that in the transmission NEXAFS results, but because of the high surface sensitivity this is likely to contain a large contribution of B_2O_3.

The sharp features in the TEY spectra are totally absent in the NEXAFS spectra, despite the high signal/noise level of the measurements. Since the measurements were taken during the same session on the same specimens, it is reasonable to assume the surface phases were present for both, and the absorption

signal from them must be incorporated into both sets of results. The standard deviation of the transmission NEXAFS spectra near 192eV is about one part in 300, while the sharp features in the TEY curves are about 7% of the total signal or one part in 13. If the sharp features are present but fall within the noise, they can be estimated to represent less than 13/300 of the sample thickness. For the 1500Å multilayers in the x-ray transmission specimens this is about 66Å or a contaminated layer about 33Å on each side. This figure is comparable to the average photoelectron escape depth of 50Å or less mentioned earlier, so it is possible that the contamination layer runs deeper but the signal from it is limited by the escape depth. However, since the signal is also absent in the 400Å-thick EELS specimens, the thickness of the contamination layer must not be much greater. A similar calculation of the EELS noise level puts the thickness at 30Å or less. A detailed calculation of the expected energy distribution of the photoelectrons and Auger and secondary electrons could give a more quantitative interpretation, and the contamination layers could be as thin as a few atomic diameters.

5.5 General Discussion

Results from the three techniques are consistent in showing only subtle changes in the absorption spectra with d-spacing. Since there is significant intermixing at the largest d-spacing, as indicated by the apparent expansion of the W-rich layers, and there are still separate phases at the smallest d-spacing, as is clear from the plan-view TEM results, it is possible that the average density of the W-rich layers, and hence the amount of W-B bonding occurring within them, is similar through the range of d-spacings despite the large changes in layer thickness. Results in Chapter 6 of fits to specular reflectivity support this – the apparent expansion of the W-rich layers is similar over the whole range of d-spacings. Even if this density does not change, the boron atoms in the B_4C layers (on the average) become closer to the W-rich layers on the average as the d-spacing decreases, which will bring some change in the average boron bonding. Another interpretation is that the degree of intermixture increases significantly, but the bonding of B with W gives a similar boron absorption spectrum to that of B in B_4C. Some support for this possibility is given by the fact that there is significant intermixture of W and B_4C even at the largest d-spacing, indicating that W-B bonding is already present, but the spectra for this d-spacing are similar to those of pure B_4C. In this

case the subtle changes in the spectrum reflect significant differences in the bonding configurations. The π^* feature represents unhybridized p orbitals, so a stronger π^* peak with smaller d-spacing is consistent with less hybridization, and with boron forming bonds with W with a more ionic character and lower coordination than its bonds in B_4C. The introduction of some d character, from the tungsten 5d bonding, to the nearly sp^2 bonding in B_4C is likely. Comparison with experimental absorption curves or electronic structure calculations for tungsten borides would give insight here.

The techniques have different advantages which might be commented on here. The EELS results had a lower energy resolution than the x-ray techniques, though the higher resolution of the Philips CM200 (1.1eV) is sufficient to detect most absorption features, which are about 1eV wide or more. The flattening of the EELS curve for the 14Å multilayer demonstrates the high sensitivity of the technique to the sample thickness, which presents difficulties in comparison of results from different samples. The absolute energy calibration must also be checked frequently if the energies of features on different curves are to be compared, as shown by the energy offsets of 1-2eV in Fig. 4. The EELS measurement has much higher spatial resolution than the x-ray techniques, however.

Results from the x-ray techniques showed a very good signal/noise ratio with sufficiently long counting times, which is essential for interpretation of subtle systematic changes between specimens. These measurements also had a high accuracy and resolution of the energy. When sharp peaks are present their position can be measured to 0.1eV or better, allowing detection of small energy shifts. It is clear that the issue of where the signal originates in the sample is important however. The extreme surface sensitivity of the TEY technique clearly shows that its results must be interpreted more carefully than they often are in the literature. While the transmission NEXAFS measurement avoids this difficulty, the preparation of a transmission specimen is not suitable for all investigations.

5.6 Conclusions

Measurements of the boron near-edge fine structure by electron energy-loss spectroscopy (EELS), near edge x-ray absorption fine structure (NEXAFS), and absorption edge total electron yield (TEY) are consistent with a highly disordered bonding environment for the boron atoms. Multilayers of periods from

6Å to 30Å showed similar spectra in all three techniques, with a π^* feature near 192eV and a broad σ^* feature from about 195eV to 205eV. Sharp peaks detectable with TEY were not verified by the other techniques and are likely attributable to a surface oxide B_2O_3 and another surface phase, showing a high surface sensitivity to the TEY technique.

The most reliable results, in bulk sensitivity and signal/noise ratio, were those of transmission NEXAFS. These showed subtle systematic changes through the range of multilayer d-spacings. Increasing intensity of a π^* feature at 192eV with decreasing d-spacing is consistent with an increasing presence of unhybridized boron p-orbitals, which can be interpreted as the B forming fewer bonds or bonds with more d-character as it forms bonds with W. A gradual narrowing and change of shape of the broad σ^* feature with decreasing d-spacing is consistent with a progressive change from the bonding state of B in B_4C to a different state, presumably like that of B in W_2B or WB. Though a definitive interpretation is difficult without comparison with results from tungsten borides, taking into account the microstructure information from TEM the results are consistent with a model in which significant intermixing of W and B_4C occurs at all d-spacings and the degree of intermixture increases with smaller d-spacings. The increase in intermixture may result from incorporation of more boron in the W-rich layers or simply from increasing proximity as the individual layers get thinner.

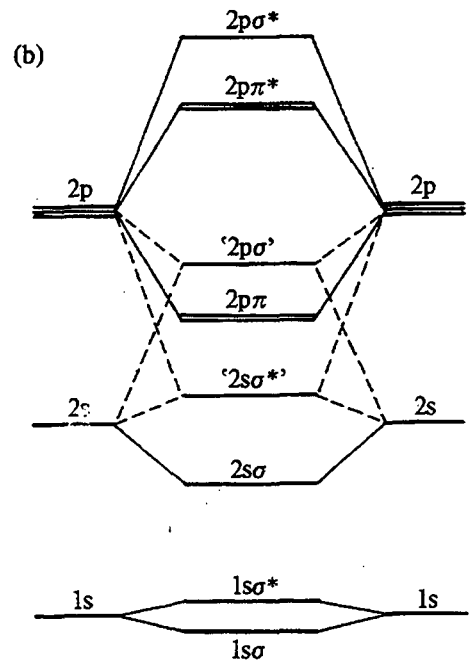

Fig. 1. Schematic of two-atom bonding, including hybridization between the 2sσ and 2pσ, after Atkins[1]. For bonds between B and C the levels are filled through part of the 2pπ.

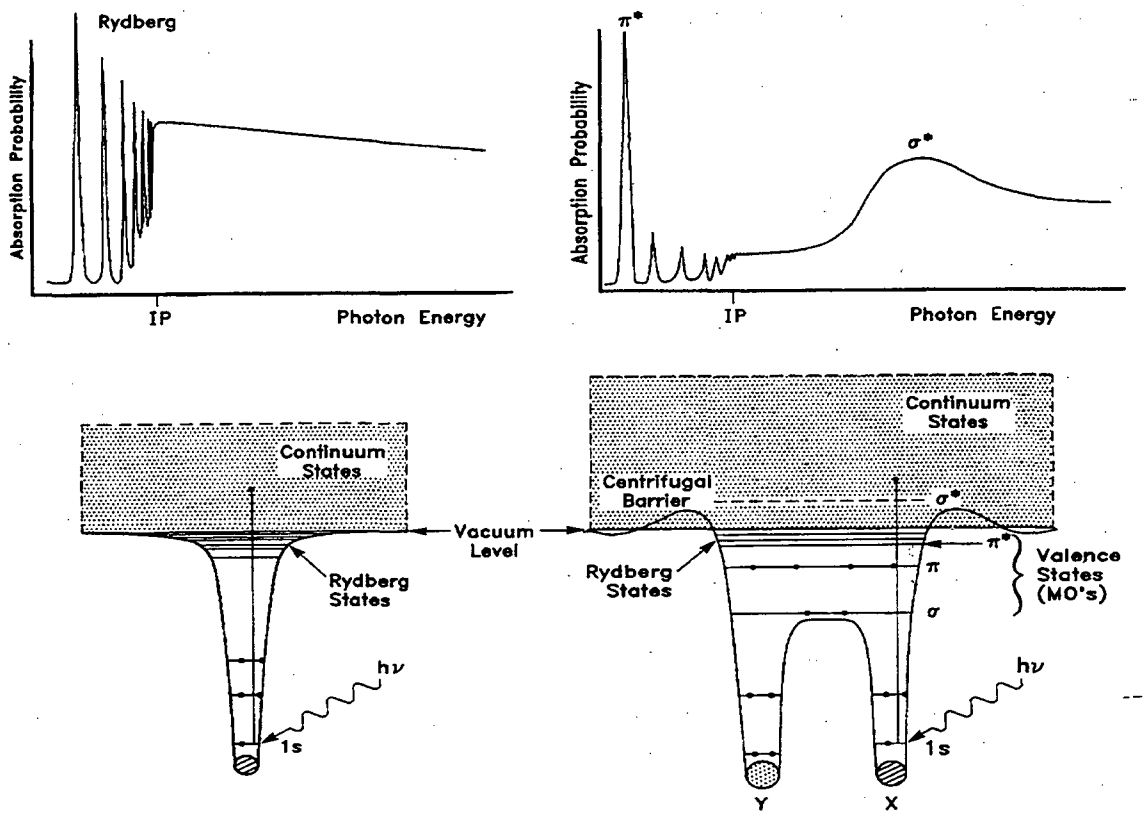

Fig. 2. Schematic of bonding levels (bottom) and absorption spectra (top), after Stohr[2]. Illustrates the displacement of Rydberg states and formation of hybridized antibonding states π^* and σ^* by the transition from isolated atom energy levels to diatomic molecular levels, and by extension to larger molecules and solids. The IP or ionization potential is defined as the energy to excite the 1s electron to the vacuum level. The π^* and σ^* states are normally above the vacuum level for a diatomic molecule but a Coulombic electron-hole interaction can shift them down, bring the π^* below the vacuum as shown.

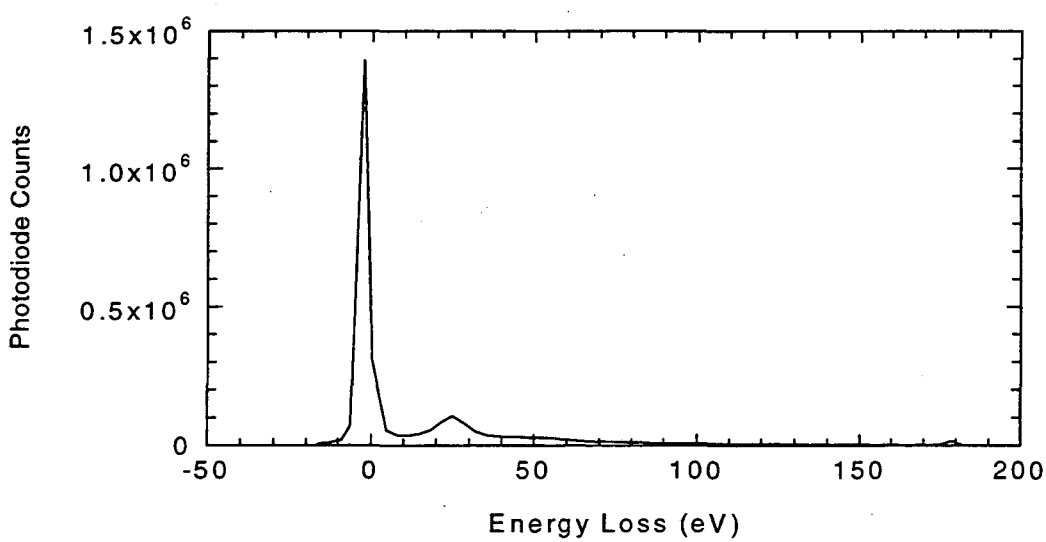

Fig. 3. Zero-loss peak and first plasmon peak in Electron Energy Loss Spectroscopy (EELS) signal for 6Å multilayer.

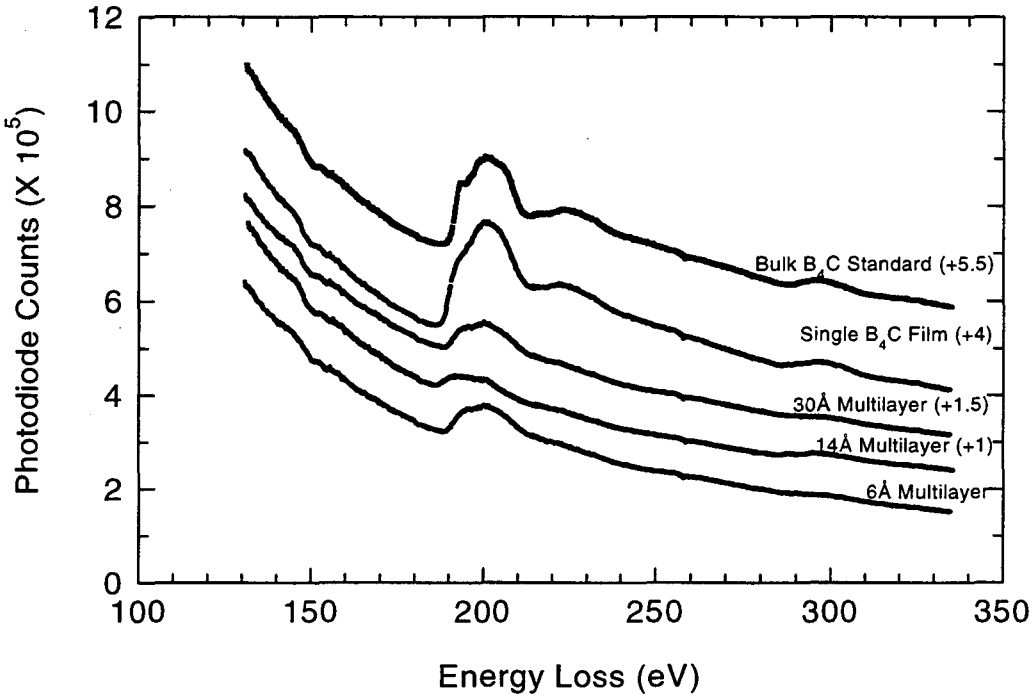

Fig. 4. Raw EELS spectra for three W/B_4C multilayers, and two B_4C standard specimens.

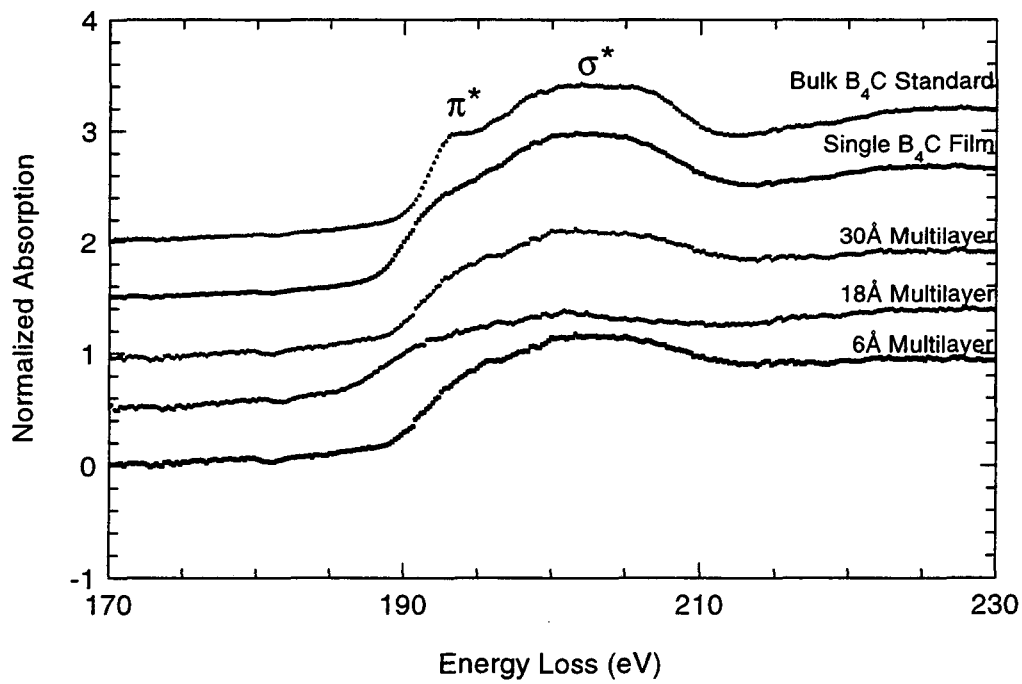

Fig. 5. Boron K-edge EELS for three multilayers and two B_4C standards, normalized from Fig. 4 by subtraction of exponential background and normalizing post-edge intensity to unity.

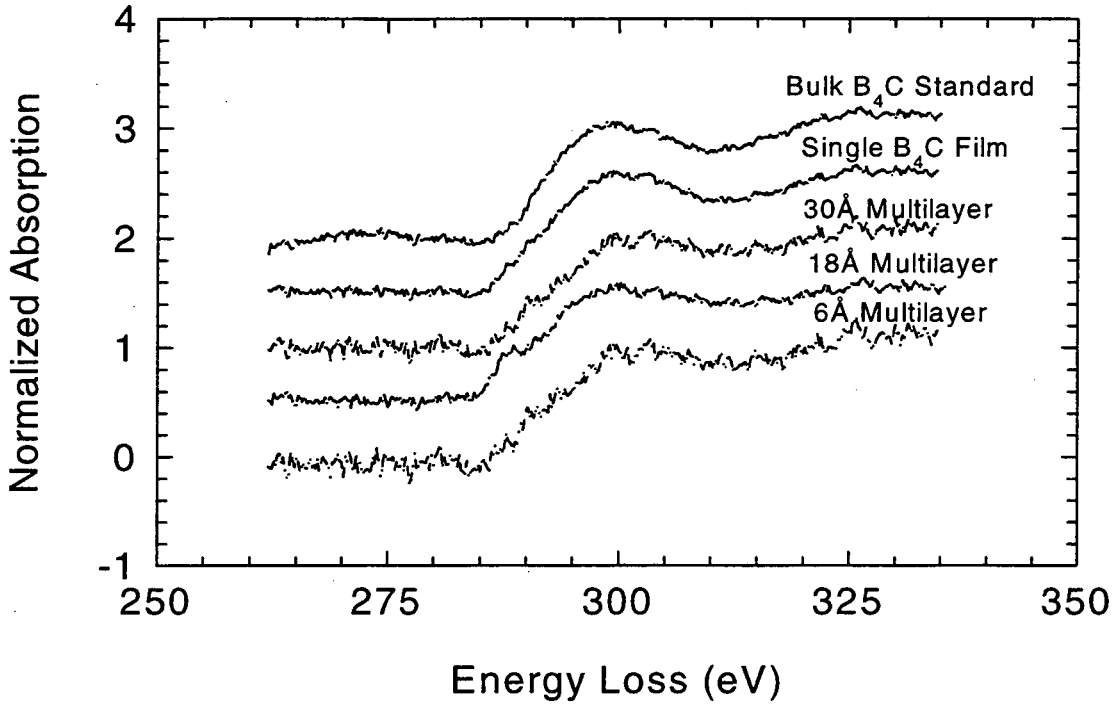

Fig. 6. EELS spectra at the C edge for three W/ B_4C multilayers and two B_4C standards.

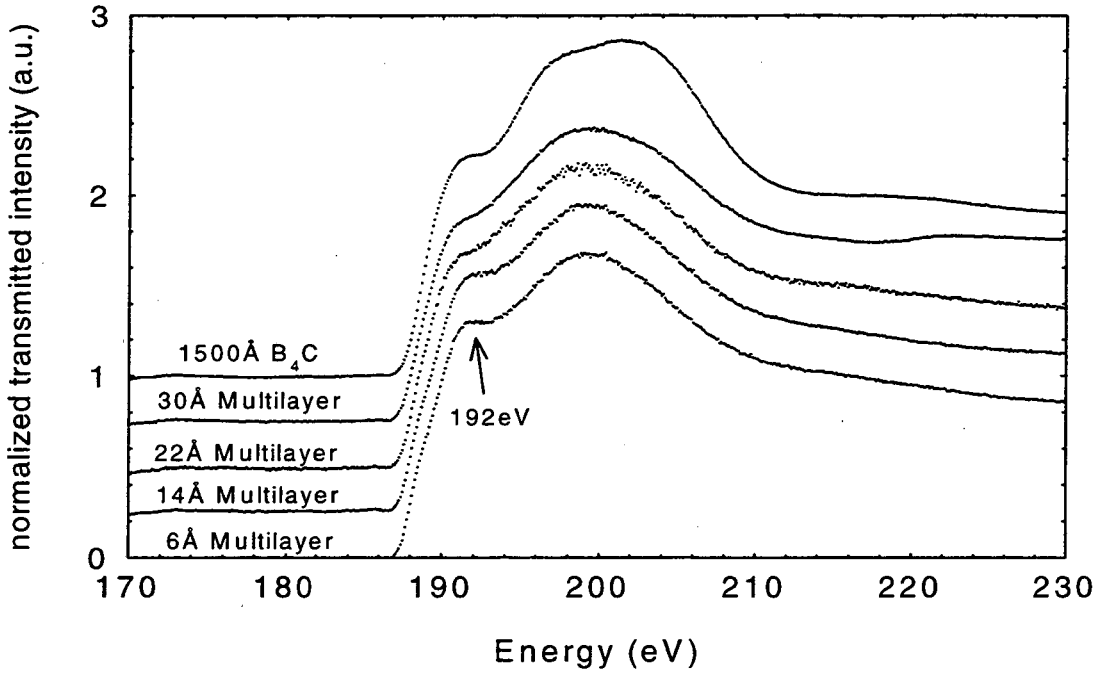

Fig. 7. NEXAFS results for four W/ B_4C multilayers of different periods, and a sputtered B_4C film grown under the same conditions.

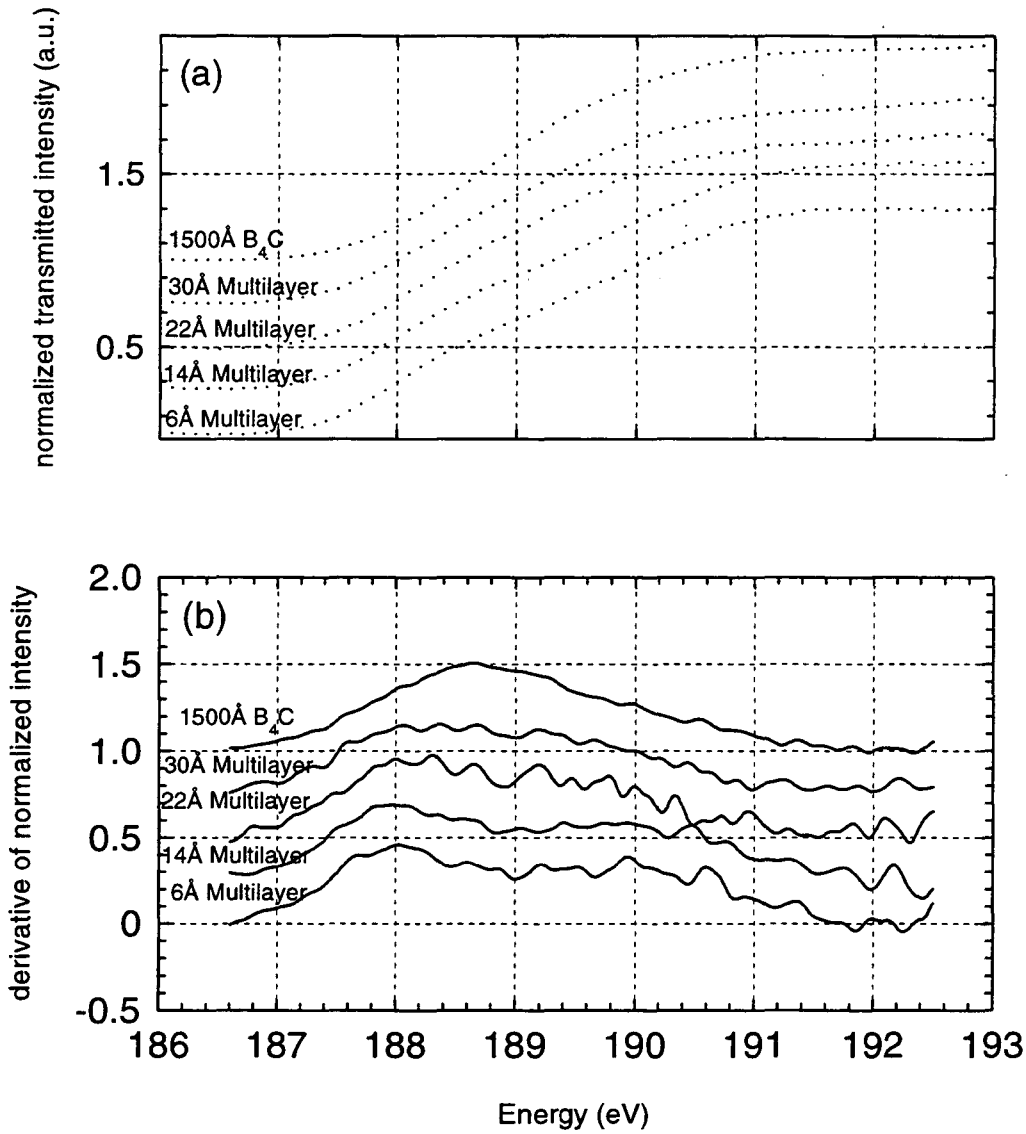

Fig. 8. *(a)* Expanded plot of NEXAFS results from Fig. 7 near 192eV. Weak feature can be seen for smaller d-spacings near 188eV, reducing in intensity as d increases. *(b)* Derivative curves of above. The derivatives are calculated from a spline of the experimental curves with extra points interpolated, and have been smoothed by a window of width 0.15 eV.

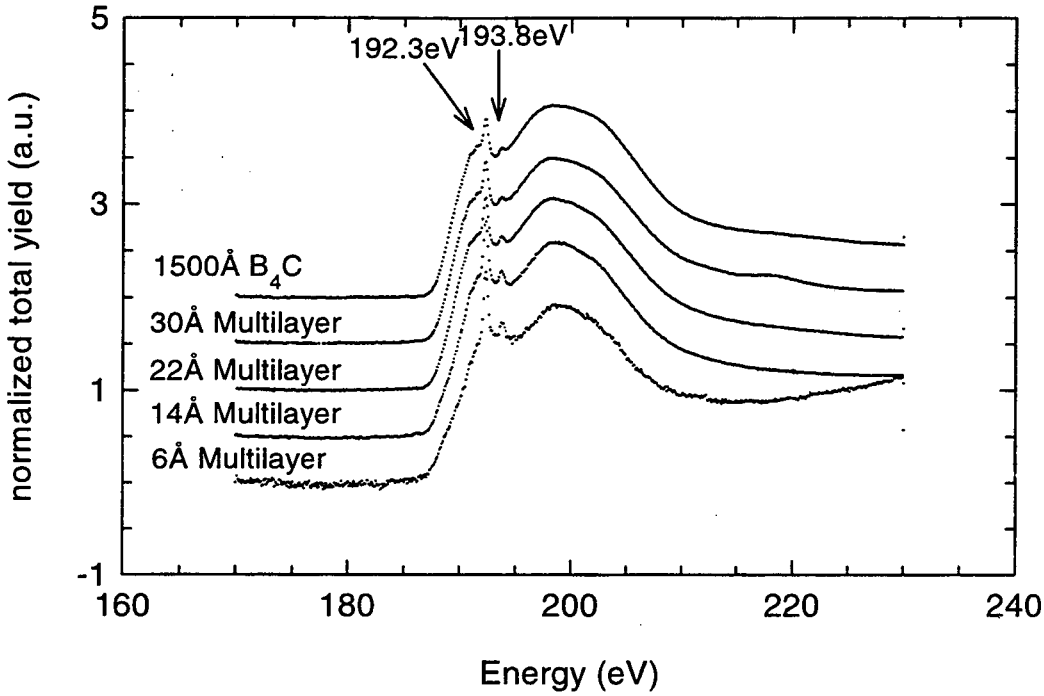

Fig. 9. Near-Edge X-ray Absorption Fine Structure by total yield (TEY), for four W/ B_4C multilayers and single B_4C film.

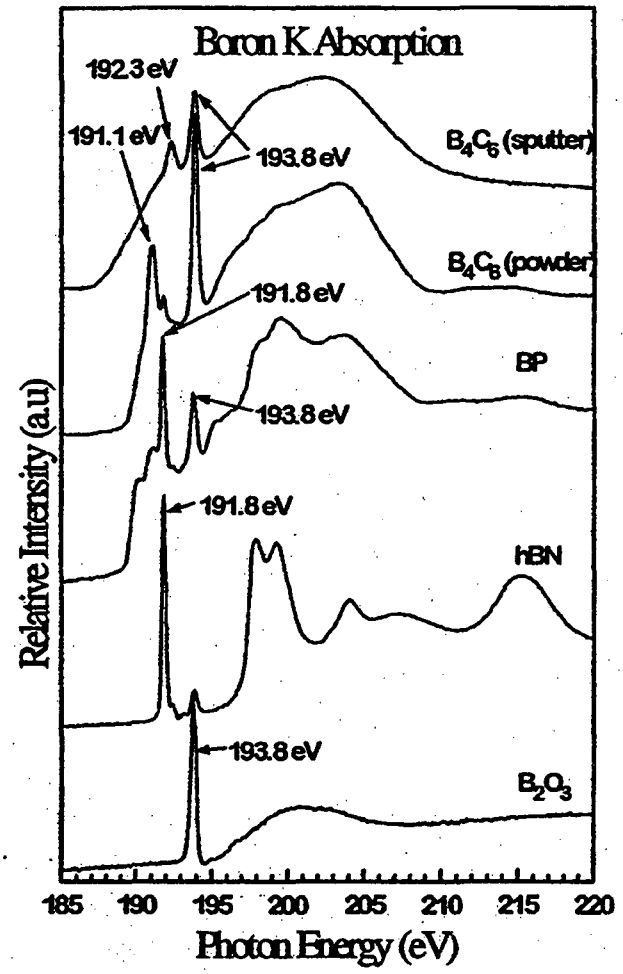

Fig. 10. Boron k-edge results by Jia *et al.* [10]

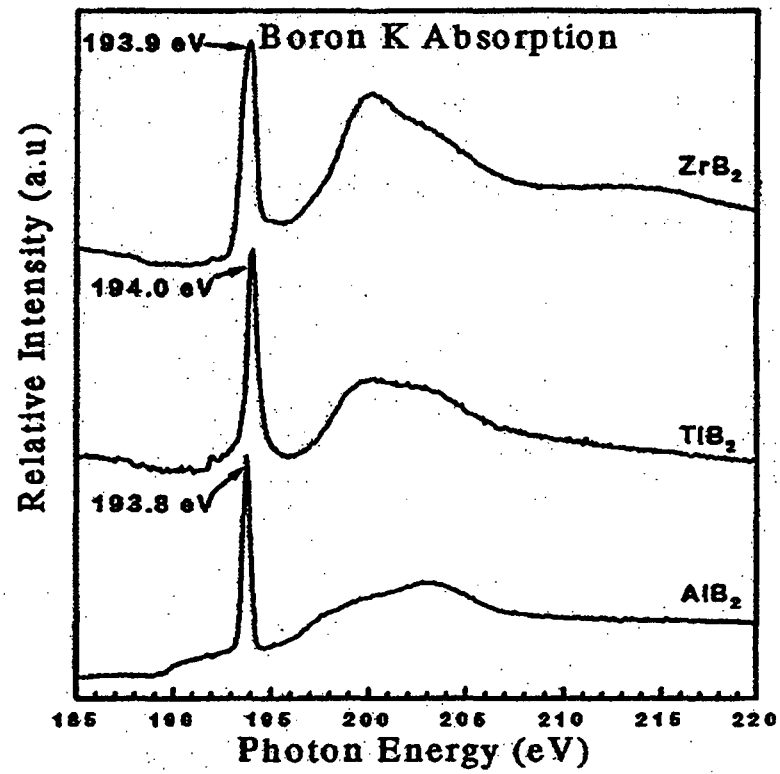

Fig. 11 Boron k-edge results from metal-B compounds by Jia *et al.*[10]

References

[1]P. W. Atkins, *Molecular quantum mechanics* (Oxford University Press, Oxford [Oxfordshire] New York, 1983).

[2]Joachim Stohr, *NEXAFS spectroscopy* (Springer-Verlag, Berlin New York, 1992).

[3]David B. Williams and C. Barry Carter, *Transmission electron microscopy : a textbook for materials science* (Plenum Press, New York, 1996).

[4]J. L. Dehmer, D. Dill, and S. Wallace, "Shape-resonance-enhanced nuclear-motion effects in molecular photoionization," Physical Review Letters **43** (14), 1005-8 (1979).

[5]S. Manninen and K. Hamalainen, "High-resolution inelastic X-ray scattering study of the boron K absorption edge," Physical Review B (Condensed Matter) **45** (7), 3878-81 (1992).

[6]D. W. Bullett, "Structure and bonding in crystalline boron and $B_{12}C_3$," Journal of Physics C (Solid State Physics) **15** (3), 415-26 (1982).

[7]D. W. Bullett, "Further Electronic Structure Studies of Boron and Boron-Rich Borides," in *The physics and chemistry of carbides, nitrides, and borides*, edited by R. Freer (Kluwer Academic Publishers, Dordrecht Boston, 1990), pp. xii, 734.

[8]H.C. Yeh and L.V. Azaroff, "X-Ray K Absorption Edges of Alloys. III. Copper-zinc and Nickel-zinc systems," Journal of Applied Physics **38**, 4034-38 (1965).

[9]H.C. Yeh and L.V. Azaroff, "Electronic Structure of Copper-Zinc Solid Solutions Deduced From Their X-Ray K Absorption Spectra," Applied Physics Letters **6**, 207-8 (1965).

[10]J. J. Jia, J. H. Underwood, E. M. Gullikson *et al.*, "Soft X-ray absorption spectroscopy in 100-1000 eV region at the ALS," presented at the 11th International Conference on Vacuum Ultraviolet Radiation Physics, Tokyo, Japan, 1995 (unpublished).

[11]A. Chaiken, L. J. Terminello, J. Wong *et al.*, "Electronic and atomic structure of metastable phases of boron nitride using core-level photoabsorption," Applied Physics Letters **63** (15), 2112-14 (1993).

[12]L. J. Terminello, A. Chaiken, D. A. Lapiano-Smith *et al.*, "Morphology and bonding measured from boron-nitride powders and films using near-edge X-ray absorption fine structure," presented at the 40th National Symposium of the American Vacuum Society, Orlando, FL, USA, 1993 (unpublished).

[13]A. Mansour and S. E. Schnatterly, "[Anisotropy of BN and Be X-ray-emission bands]," Physical Review B (Condensed Matter) **36** (17), 9234-40 (1987).

[14]B. M. Davies, F. Bassani, F. C. Brown *et al.*, "Core excitons at the boron K edge in hexagonal BN," Physical Review B (Condensed Matter) **24** (6), 3537-46 (1981).

Chapter Six

Analysis of X-Ray Reflectivity

6.1 Introduction

At the same time as being the primary function of these multilayers, the scattering of x-rays by them provides a powerful probe into their structure, as it does in other studies of materials structure. The scattered signal averages over the width of the beam, much larger than the multilayer period and any microstructure effects characteristic of the thin film growth, and therefore complements the local structural information from the TEM.

The reflectivity is sensitive to many aspects of the multilayer structure. The density of the films determines the reflectivity at the individual interfaces, and the precision of the layer thickness affects the width of the interference peaks. The abruptness and roughness of the interfaces also has a strong influence on reflectivity, and careful analysis of the reflectivity can give information on all of these factors.

The x-ray analysis can be divided in two parts, the *specular reflectivity*, meaning elastic scattering recorded at a symmetric condition of equal incident and exiting angles, and the *diffuse scattering*, meaning all scattering events away from the specular condition. This chapter will present analysis of the specular results in Chapter 3, and the next chapter will cover diffuse scattering studies.

6.2 Theory and Methods of Reflectivity Analysis

6.2.1 Example Case

The specular reflectivity over the range of incident angles contains much useful information besides the multilayer period and peak reflectivity. To summarize this a simulated curve is shown in Fig. 1. The solid curve is the reflectivity of a W/B_4C multilayer of 100 periods with d = 20Å and $\Gamma = 0.45$. For illustration the dotted curve is a homogeneous film of the same total thickness with the average composition of the multilayer.

The refractive index of most materials is less than unity in the x-ray regime, but it is so close to unity that it is usually written as $n=1-\delta-i\,\beta$, where the optical constants $\delta(\omega)$ and $\beta(\omega)$ depend strongly on the photon energy, especially near absorption edges. Here the real part $1-\delta$ describes refraction in the usual use of the index, and the imaginary part $i\beta$ describes absorption. Since an x-ray beam entering a multilayer is passing from a denser to a rarer medium (from n = 1 to $n=1-\delta-i\,\beta$), it is refracted away from the surface normal, contrary to the usual refraction of visible light. The phase velocity of the wave is now greater than *c*, though the group velocity (at which the energy is transported) is still less than *c*. Below a critical incident angle the refracted beam is parallel to the surface. It no longer penetrates the multilayer but runs along the surface as an evanescent wave; this is the condition of *total external reflection.*

In the reflectivity shown there is total reflection from $\theta = 0°$ to the critical angle of about 0.4°. The evanescent wave actually has a slight penetration of the surface, with the electric field dropping off exponentially with depth. Because of the slight penetration there is also a slight absorption, which causes the small loss of reflectivity before the critical angle. The critical angle itself is a refractive effect and so depends on δ, and it can be shown[1] that to first order $\theta_c = \sqrt{2\delta}$. If the material is inhomogeneous, for example a multilayer, the effective δ is an average over the penetration depth. At the critical angle the penetration depth[2] is about $\beta^{1/2}/2\pi$, which for these materials at $\lambda = 1.54$Å is about 125Å, or at least 3 multilayer periods. Thus for short-period multilayers such as these the critical angle is a measure of the average δ of the stack, as demonstrated by the fact that the multilayer and the homogeneous film in Fig. 1 have the same critical angle. While the angle θ_c is a refractive effect, the rounding of the critical angle "shelf" results from absorption: the larger β is, the more the reflectivity falls before θ_c and the rounder the shelf at θ_c. Thus, from the shape of the critical angle and its angular position, we in fact have measures of both average optical constants, δ and β.

After the critical angle the reflectivity drops steeply. The beam now penetrates deep into the stack, so the slope of this dropoff also depends on the average optical density, and also on the film roughness, which will be discussed below. In the case of a multilayer the dropoff is heavily modulated by the multilayer's internal interference, as can be seen by the difference between the two curves in Fig. 1. Between the reflection maxima the multilayer can reflect less than the homogeneous film when it reaches destructive interference condition. There is also a fine modulation from the top and bottom surfaces of the stack, and for a multilayer of N periods there are N-1 of these between each Bragg peak. Similarly to the Bragg modulations for the multilayer, these features depend on the optical contrast at the top and bottom interfaces of the multilayer, and are weak if these surfaces are rough. This fine modulation is near the resolution limit of the reflectivity measurements, so it appears weakly in the experimental reflectivities.

Away from the critical angle, the reflectivity also shows some dependence on polarization of the incident beam. The polarization states are defined relative to the plane of incidence, which is the plane containing the incident ray and the reflected ray. The two states are customarily labeled s (from the German *senkrecht*, perpendicular) for radiation with the electric vector perpendicular to the plane of incidence, and p (*parallele*) if the electric vector lies in the plane. Any state of linear polarization can be written as a linear combination of these. At $\theta = 45°$, which is the polarizing angle since the refraction is negligible, the p-component is suppressed, which allows the use of these multilayers as linear polarizers.

The Bragg peaks themselves represent the Fourier components of the composition modulation, or alternatively, different order constructive interference peaks from the periodic interfaces. Since these multilayers are amorphous there are no strong Bragg peaks from interatomic scattering. If the layers were epitaxial, multiple scattering between the two periodic structures would give other multilayer peaks as satellites around the atomic Bragg peaks. For the amorphous multilayer the Bragg peaks can be considered satellites about the incident beam at $\theta = 0°$.

The heights of the peaks give information about the shape and strength of the composition modulation. In the multilayer in Fig. 1 the value of Γ is near 0.5, so the even-order peaks are partly suppressed. At $\Gamma = 0.5$ the composition profile would be a square wave which requires no even-order Fourier components. Or from the optics viewpoint, the extra interface exactly in the middle of the multilayer period would then be a second scatterer with half the path-length difference of the top and

bottom interfaces, which, taking into account the phase changes for reflecting from the different interfaces, would give destructive interference on the even-order reflections. In modelling the reflectivity the value of Γ can be measured from the relative peak heights if enough Bragg peaks are present in the experimental data. The strength of the reflectivity modulation is affected by any roughness in the buried interfaces, since this degrades their individual reflectivities. Finally, the widths of the peaks are determined by the number of periods in the stack, just as interatomic peak widths depend on crystal size. The peak widths are also affected by any change in the sputtering rates during growth of the multilayer, since this will cause a variation in the period.

Direct Fourier analysis of the reflectivity peaks is a powerful technique, which has been applied heavily in the use of multilayers in diffusion studies. For such studies, a multilayer is grown of two materials and annealed, and the decay of the peaks recorded with time. The peak heights may be satellites of an interatomic peak, in an epitaxial multilayer, or the fundamental peaks of the multilayer. Since the peak heights represent sinusoidal components of the composition modulation, with shorter wavelengths for the higher orders, they decay at different rates, and the results can be related to diffusion theory. In the case of non-linear diffusion, in which the diffusivity is a function of concentration, the decay of the peaks can show complex behavior in the higher orders. This technique has the advantage of sensitivity to extremely small diffusivities, as low as 10^{-27} m^2s^{-1}, because of the small length scales and the signal contribution from many interfaces at once. Study in this field began with the first detection of multilayer modulation by duMond and Youtz[3], and major contributions have been made by Cook and Hilliard[4] and Menon *et al.*[5,6]. A recent review is given by Greer.[7]

The application of this technique to x-ray multilayers is not common, largely because the intensity of the fundamental is already known, since the materials are chosen for low diffusivities and stable structure, and the interface information in the highest harmonics may not be measurable. Also, the full concentration profile, which is likely to be asymmetric for sputtered multilayers with large mass differences, cannot be reconstructed without the phase information of the peaks. Attempts have been made to record phase information but with limited success.[8]

A common assumption of this type of reflectivity measurement is that the inelastically-scattered component of the beam is small. The NaI scintillation detector has a low energy resolution, using a window

of output voltages as described in Chapter 3, which is sufficient to remove the inelastic scattering with large energy losses and the (333) reflection of the monochromator. The discriminator does not distinguish between elastic scattering and inelastic scattering with losses of up to a few hundred eV, so the measurement is largely of the total scattering. Models of the reflectivity, on the other hand, consider only elastic scattering at the interface. The assumption that the inelastic component is small is a reasonable one, and a large body of literature has analyzed diffraction from crystals and multilayers with this assumption and obtained good agreement with experiment. The inelastic component is detectable, however, and with detectors with high energy resolution it can be used with a monochromatic incident beam for spectroscopic analysis analogous to the EELS measurment with electrons, described in Chapter 5. One such study by Manninen[9] is cited in that chapter. The same considerations apply to the soft x-ray measurements.

6.2.2 Calculating Reflectivity

The reflectivity of a multilayer can be calculated from the well-known Fresnel equations for reflection at a single interface.[1] At an interface between two materials of indices n_1 and n_2, the amplitude reflectivities (from the n_1 side) for the *s* and *p* components are

$$r_{12}^{s} = \frac{n_1 \cos\phi_1 - n_2 \cos\phi_2}{n_1 \cos\phi_1 + n_2 \cos\phi_2} \quad , \quad r_{12}^{p} = \frac{n_1 \cos\phi_2 - n_2 \cos\phi_1}{n_1 \cos\phi_2 + n_2 \cos\phi_1} \qquad (1)$$

where ϕ_1 and ϕ_2 are the angles between the beam and the surface normal in the materials 1 and 2. These equations are derived by equating parallel electric field components at the interface and are therefore quite general. Since the indices are complex in the x-ray regime, the angles (related by Snell's Law) and the amplitude reflectivities are also complex, giving amplitude and phase information for the reflected wave.

For a multilayer structure the waves reflected at the various interfaces add, and to account for the multiple reflections a system of equations is written for the forward- and backward-running waves at each interface. These can be solved for the reflectivity of a generalized single film structure

$$r = \frac{r_t + r_b \exp(2i\varphi)}{1 + r_t r_b \exp(2i\varphi)} \tag{2}$$

where r_t and r_b are the amplitude reflectivities of the top and bottom interfaces, and $\varphi = (2\pi/\lambda)nt\cos\phi$ is the phase delay for a wave propagating through the film of thickness t and index n, and ϕ is the angle of the beam in the film, related directly to the original incident angle by Snell's Law. This reflectivity can be calculated for the bottom layer of a multilayer stack, then the result used as r_b for the next layer up, and so on until the top is reached. Since these solutions are exact this iterative method is valid for an arbitrary number of layers. However, since $n = 1 - \delta - i\beta$ is very close to unity (δ and β are of the order 10^{-5} - 10^{-8} for most materials at CuK_α) it is important to use high-precision variables for the computation. The values of δ and β are related to the atomic scattering factors by

$$n = 1 - \delta - i\beta = 1 - \frac{r_0}{2\pi}\lambda^2 \sum_j n_j f_j(0) \tag{3}$$

where the sum is over the elements present j with number density n_j and scattering factor f_j, ro is the classical electron radius 2.82 x 10^{-15}m and λ is the wavelength. The atomic scattering factor has been tabulated for the elements $1 \leq Z \leq 92$ by Henke *et al.*[10] for a wide range of the electromagnetic spectrum including the soft and hard x-ray. The Henke values neglect anomalous scattering near absorption edges which can significantly alter the scattering factor. This was not of concern for these measurements, except for the reflectivity at 45° for the d = 31.9Å multilayer, for which the multilayer peak at λ = 63.5Å (E = 195eV) is only 7eV above the boron k-edge at 188eV. In this measurement a small shoulder is visible on the reflectivity curve. Fits using the tabulated values were able to duplicate the rest of the curve so this shoulder is not significant.

6.2.3 Analyzing Real Multilayers

In calculating reflectivities to make quantitative comparisons with experimental data, several limitations and subtleties must be taken into account. These will be described briefly here.

a) Measurement range. At low incident angles the projected width of the beam on the sample may be more than the sample width - the beam overfills the sample. In this case some of the incident beam misses the sample entirely, and it is not meaningful to divide by the full beam intensity to obtain the absolute reflectivity. For these measurements the incident beam was set fairly wide at 0.5mm to obtain a large flux, so a 3-inch wafer sample does not fill the beam until $\theta \approx 0.7°$. This is larger than the critical angles of all the elements in the multilayers, so the apparent values of the critical angle are not reliable. At high incident angles the reflectivity falls below the dark-count level of the detector, and only peaks extending above that level can be considered real data.

b) Angular resolution. The x-ray beam has a finite width which determines an angular spread of incident rays, and likewise there are two collimating slits in front of the detector set to accept the full width of the incident beam and exclude any other signal. These set a limiting angular resolution of the measurement, within which features are averaged. This resolution is about 0.06° at the settings used. To account for this the calculated reflectivities were treated with a window smoothing function which averaged values for ± 0.03°.

c) Diffuse background. In addition to the true specular signal coherently reflected from the multilayer interfaces, each measurement includes incoherent or diffuse radiation which is counted by the detector but is not part of the signal to be measured. This is mainly elastic scattering from rough interfaces in the multilayer but includes contributions from interatomic scattering in the amorphous layers, Compton scattering, and detector noise. For reflectivity measurements this was measured separately by an offset scan, in which the $\theta/2\theta$ scan is repeated with θ offset by 0.3°. This offset is somewhat greater than the width of the specular peak in a rocking scan or the natural width of the multilayer reflectivity, so the offset scan provides a reasonable measurement of the diffuse contributions alone. This scan is then subtracted from the specular. This generally has only a small effect on the reflectivity except at high angles where the

specular reflectivity is weak. Fig. 2 shows a specular/diffuse pair of scans plotted together. Even at order 7 Bragg peak the diffuse is nearly an order of magnitude below the specular.

d) Variation in d-spacing. The low sputtering pressures used to obtain the best multilayers cause the sputtering rates to be low, and together with the large number of layers this makes the sputtering runs long , often 2 to 3 hours. Even with several minutes' warmup before beginning deposition on a specimen, variation in sputtering rates occurs from gradual warming of the apparatus, wear of the targets, and change of the sputtering gas atmosphere, resulting in changes of the d-spacing. A distribution of d-spacings broadens the peaks. In some cases a distinct splitting of the peaks is visible, indicating an abrupt change. Abrupt changes were sometimes observed in the sputtering voltage during runs. In other cases peaks are broadened and one cannot tell whether the change is abrupt or gradual. These errors were accounted for in the fitting by providing for gradual or abrupt thickness variations in the calculations. The functional form of the thickness variation was specified by the Taylor coefficients of a function giving the percent change of layer thickness as a function of the layer number, thus allowing any well-behaved analytic functional form to be used. In practice there is insufficient information in the peak shape to justify complicated forms and nothing above a linear variation was used. The variations, typically totaling 1 or 2 percent in the d-spacing, were estimated by matching the shapes of the highest-angle (and thus broadest) peaks. While the variation selected to match the peak shape may not be unique, the choice has little effect on the fit parameters so long as the width of the peak is matched. Even for the shortest-period multilayers near d = 5Å, the broadening was no greater than for the continuous multilayers at larger periods.

e) Value of gamma. While Γ is in principle known from the sputtering rates and times of the two materials, it can vary by a few percent in most multilayer systems, and, as discussed in Chapter 3, it is far from the nominal value in this system because of reaction of the two materials in the very thin layers. For the larger d-spacings it can by measured in the TEM image, but for purposes of x-ray analysis it is used as a fitting parameter.

f) Density of the layers. It is common for sputtered films to have lower density than the bulk, especially very thin films with much disorder. However, previous results from samples made in this sputtering system[11] have shown very thin films to have densities near the bulk values, such as 10Å Ru films that show an hcp crystalline structure. This indicates that the sputtering conditions themselves promote high-

density growth, which is consistent with the growth theory for the low sputtering pressures used. However, the materials may react, as W and B_4C appear to, and the resulting W-rich layer is certain to be less dense than W. The fitting accounts for this by adjusting the density of the W-rich layers in proportion to the expansion of the film from Γ_{nom} to the value of Γ being fit, or in other words letting the value of Γ change but conserving material. While this model is the most physically realistic it did not always produce the best fits as the results will show.

6.2.4 Treatment of Interface Roughness

For multilayers used at visible wavelengths, the model assumed by the Fresnel equations of homogeneous layers with flat and abrupt interfaces is usually a reasonable one because the layers have a thickness much greater than the size of most of their imperfections. The few imperfections which are as large as the layer thickness tend to be localized, and are better treated as separate structures. In the case of x-ray multilayers, however, the individual layers are a few atoms or a few tens of atoms thick, and defects inherent to the layers are relatively larger and are significant to the optical performance. These include roughness, interdiffusion, and inhomogeneities within the films in the vertical and lateral directions. Because of the difficulty of separating the effects of these, and the number of phenomena contributing to them, this area is the most difficult part of understanding optical performance of multilayers and will be treated in some detail. This section will concentrate on effects on specular reflectivity, and the related material on diffuse scattering from rough or inhomogeneous layers will be in the next chapter.

For the purpose of specular reflectivity, the scattering vector always lies by definition perpendicular to the average surface of the layers, so the measurement is only sensitive to the composition profile in this direction. The measurement also averages over the area illuminated by the beam, which is much larger than any of the microstructure defects of interest. Thus the specular x-ray measurements are sensitive only to an averaged concentration profile in the vertical direction, and the effects of roughness and interdiffusion are indistinguishable. They are often lumped together as "roughness" effects in the literature. For this section roughness will be understood to mean blurring of the interfaces from either of these effects.

The general problem of scattering from rough surfaces is a complex one and will be discussed in parts in the rest of the chapter and in Chapter 7. Roughness occurs at a wide range of spatial frequencies and with a distribution of surface heights, and can be generally described by specifying these. One statistical approach is to specify the power spectral density or PSD, which gives the power of the various spatial frequencies contributing to the roughness. The PSD is defined as[12]

$$S(f) = \lim_{L\to\infty} \frac{1}{L} \left\langle \frac{2}{L} \left| \int_{-L/2}^{+L/2} Z(x) \exp(-2\pi i f x) \right|^2 \right\rangle \tag{4}$$

where f is the spatial frequency, L is the the trace length of the measurement, and Z(x) is the height of the one-dimensional surface. The averaging is over a large number of measurements of the surface. The PSD contains implicitly the height distribution information, since the "power" is proportional to the square of the amplitude, i.e. the surface height, at a given frequency. Roughness is also commonly characterized by the correlation function (also called the height-height correlation function or the self-correlation function):

$$C(\tau) = \lim_{L\to\infty} \frac{1}{L} \int_0^{L-\tau} Z(x) Z(x+\tau) dx \tag{5}$$

The correlation function and the PSD are a Fourier transform pair.

When light hits the rough surfaces, it is dispersed at a range of angles by the range of surface orientations it sees. Each point on the surface can be considered a separate scatterer, and waves scattered from different points add with phase depending on the separation of the points. A measure of how two points separated by a distance Λ will scatter over various angles is given by the grating equation:

$$\lambda = \Lambda(\sin \Phi_{out} - \sin \Phi_{in}) \tag{6}$$

where λ is the wavelength of the incident beam. Thus the smallest separations, or highest spatial frequencies, scatter radiation at the highest angles away from the specular beam, and the lowest scatter close to the specular condition.

The total roughness σ^2 (or the variance of Z(x)) is the sum of all frequency contributions:

$$\sigma^2 = \int_0^{+\infty} S(f)df \tag{7}$$

The limits on this integral require some discussion. In practice, a real measurement has a nonzero lower limit and a finite upper limit. The lowest frequency any experiment can measure is given by the information limit for the sample area scanned - the longest spatial wavelength that can be measured in a scan of length Λ is $\Lambda/2$. For an x-ray scattering experiment Λ is the width of the beam, or the lateral coherence length of the radiation, whichever is less. The highest frequency is that which scatters 180° from the incident beam (back scattering), which is a spatial wavelength of $\lambda/2$. In practice the limits may be even narrower, as will become clear below. In any case any real experiment has a finite range of sensitivity; a measurement of roughness by a scanning-probe technique, such as an AFM, will have similar lower and upper limits given by the scan length and the size of the tip.

For analyzing specular reflectivity measurements, however, a simple approach is needed. To first order the reflectivity is sensitive only to the rms height variation, since this is what reduces the constructive interference of the scattered waves, and is much less sensitive to the spatial frequency distribution. It is also more appropriate to model specular reflectivity with a single roughness parameter, rather than different parameters for the different interfaces, since there are other uncertainties which may have to be fit, such as the value of Γ. The most common approach is use the single parameter σ for the rms roughness. While this model has flaws that will soon become apparent, its results will be presented since it is a simple way of comparing multilayer quality, and it is commonly used by many researchers. If the interface height distribution is assumed to be Gaussian it can be accounted for in a simple formalism. This is analogous to assuming thermal vibrations of atoms to be Gaussian in the temperature factor for Bragg reflections in crystals, since the multilayer is a one-dimensional synthetic crystal with the interfaces as the scattering particles. The parameter σ is then set as the standard deviation of the Gaussian. The static Debye-Waller factor[13,14] is multiplied onto the amplitude reflectivity:

$$r = r_0 \exp(-\tfrac{1}{2} q^2 \sigma^2) \tag{8}$$

where r_0 is the amplitude reflectivity for an ideal structure, q is the momentum transfer $4\pi n_1 \sin\theta/\lambda$ for a photon reflected at the n_1/n_2 interface, and σ is the rms roughness of the surface. Similarly to the temperature factor, the static Debye-Waller factor assumes σ to be small compared to the layer thickness. While this condition is not met for the shorter-period multilayers in this study, the values for all specimens will be presented for continuity.

The basis for assuming a Gaussian profile rather than some other also comes from the thermal analogue. If an atom is subject to many thermal vibrations of random amplitude and phase, its net motion will be a random walk which gives a Gaussian position distribution. A point on a multilayer interface is also subject to a superposition of many static spatial waves, so averaging over space (on the plane of the interface) gives a random walk just as averaging over time does for the atom.

If the multilayers are losing reflectivity because of roughness, this formalism provides a way of measuring the roughness. Roughness may be replicated from the substrate, or may come from effects intrinsic to the layers, such as statistical variations from growth, crystallinity of the layers, or shadowing effects during sputtering. To investigate this further the reflectivities were modeled with the Fresnel equations and Debye-Waller factor.

Many investigators in the literature have used the Debye-Waller roughness factor to analyze multilayers. Stearns[15] reviews the theory thoroughly and presents the Debye-Waller factor along with formalisms for interface profiles other than Gaussian, as well as a generalized treatment in the weak-scattering (kinematic) approximation. Payne and Clemens[16] consider the issue of Gaussian random roughness and degrees of correlation of roughness from one layer to the next in the evolution of roughness during growth.

Experimentally, Nguyen *et al.*[17] have investigated the roughness of Ru/C and Ru/B_4C multilayers and its evolution during annealing, though they do not give a value of the roughness. Kortright[18] reviews the performance of x-ray optical multilayers with $8Å \leq d \leq 130Å$ and finds a trend of Debye-Waller roughness increasing approximately linearly with d, but extrapolating to an apparent minimum value near 2Å, which may be attributable to the minimum available roughness of the substrates. Yakshin *et al.*[19] studied W/C and W/B_4C multilayers of periods 29-35Å and found values of the roughness from 4Å to 6Å,

and found that the roughness depended on a discontinuous microstructure whose island size depended on the sputtering power. Christensen *et al.*[20] studied W/B_4C multilayers of periods 16-21Å and found roughness of 2-3.5Å by fitting reflectivity at CuK_α, AlK_α and FeL_α wavelengths. Savage *et al.*[21] studied W/C multilayers of period 23Å –37Å and found roughness of 2-2.5Å, and through an analysis at different wavelengths at different penetration depths, they also concluded that the roughness did not change through the multilayer stack. These values are consistent with the trend found by Kortright, except those of Savage *et al.*, which are lower. This point will be revisited later.

6.3 Analysis of Reflectivity Results

6.3.1 Fitting methods.

The reflectivities given in Chapter 3 were modeled for roughness in this way, using the same roughness for both types of interface, W on B_4C and B_4C on W. It was found that two values σ_1 and σ_2 for the two interfaces typically gave σ_1 and σ_2 only 10-15% apart and did not give a substantial improvement in fit quality. The substrate was assigned a roughness of 3Å for all specimens, consistent with measurements in the literature.[22] Since the substrate is only one of 201 scattering surfaces in an N=100 multilayer, the accuracy of this number is not of great importance.

Fits were performed with the following error metric

$$E = \sum_{\theta} \frac{(\ln I_{meas} - \ln I_{calc})^2}{\ln I_{meas}} \qquad (9)$$

where the sum is over all values of θ (with the exclusion of the region below the critical angle and below the noise level of the detector as described earlier). The usual denominator would be the standard deviation of I_{meas} over multiple measurements, but since multiple measurements of the experimental intensity were not made, its standard deviation is not available. The best available estimate is that the standard deviation is

proportional to the value of the intensity. Here the constant of proportionality has been set to unity since the error is only used comparatively.

Rather than using a least-squares fitting procedure which adjusts the parameters to find the direction of fastest reduction of the error, fits were made for a full range of values of the roughness σ and Γ, and the error plotted as a surface function of the two parameters. This gives a clear view of the sensitivity of the fits to the two parameters and the uniqueness of the fits. The reflectivity calculations were performed in double precision in Fortran, and the error contours calculated in the IDL data processing environment (Research Systems, Inc.)

A typical error surface plot is shown in Fig. 3, along with the experimental curve and the best fit (Fig. 4). The ridges in the error surface result from the contribution of Γ to the multilayer structure factor. For $\Gamma = 0.5$ there is an interface halfway through each period reflecting with a $\pi/2$ phase difference, which suppresses all the even-order peaks. Since the experimental curve shows an even-order peak, $\Gamma = 0.5$ provides a poorer fit than neighboring values of Γ, giving a higher error. The roughness depends exponentially on q^2 and moves the entire calculated reflectivity down(more at the higher angles), so the dependence of the error on σ is more gradual. The range of Γ includes all physically reasonable values, $0.2 \leq \Gamma \leq 0.8$, where the nominal Γ from the sputtering times was 0.4.

6.3.1 Fit results

The best fits are shown with the experimental reflectivities in Fig. 5, and the corresponding values of σ and Γ are given in Table 1, labeled as Model 1. The fits duplicate the peak heights quite well but not always the regions between the peaks. The greatest uncertainty in the fits is the uniqueness of Γ, which typically has two minima, one near $\Gamma = 0.64$, (the value observed in the TEM at d = 20Å and d = 30Å) and one closer to the nominal Γ. Both can be seen in Fig. 3, and in several cases the best fit was at the lower Γ. The apparent expansion of Γ is greatest at the smallest d-spacings, consistent with more intermixing for the thinnest layers and the earliest stages of growth. The values of σ show no trend.

In order to improve the fits a second model with different film densities was tried. In this model densities of the W-rich layers were calculated assuming that the layers had expanded from their nominal value of Γ to $\Gamma = 0.64$, the value observed in the TEM images at d = 20Å and d = 30Å. This density was used for all fits, regardless of the value of Γ in the fit, meaning that the amount of W in the multilayer varied with Γ. The fits from this model are shown in Fig. 6, and the fit parameters given in the table as Model 2.

While this model is less physically realistic, since the amount of W in the multilayers was verified (with the x-ray fluorescence experiments in Chapter 2) to be close to the nominal value, this model gave better fits. With this model the values of Γ are generally close to the nominal values, in contradiction to the apparent expansion in the TEM images. Since the overall composition of the multilayer is known to be fairly accurate, this most likely means that the layered model does represent the sample well. One reasonable hypothesis is that the density of the W-rich layers is not constant through their thickness, but is lowest at the early stages of the growth of each layer when the most intermixing and implantation occurs, and is higher later on as more W is deposited on the intermixed film. This may result in an asymmetric composition profile that cannot be well represented by any combination of layer thicknesses and interface blurring, where denser parts of the layer dominate the scattering and give an appearance of a lower value of Γ. Some support for this can be found in results by Stearns *et al.* in the Mo/Si system.[23] A cross-section micrograph of their multilayer shows clear asymmetric interfaces, with an amorphous layer on the interfaces where Mo was deposited on Si that is not present on the Si on Mo interfaces. In their case this layer is distinguishable because the Mo layers are crystalline, though no density difference is apparent. A detailed simulation of the sputter growth might be able to verify this. The values of σ are not strongly affected by this uncertainty, however, as the values in the table show.

		Model 1 - CuK_α (full θ range)			Model 2 - CuK_α (full θ range)			first peak CuK_α	first peak θ=45°
d (Å)	Γ_{nom}	σ(Å)	Γ	error	σ(Å)	Γ	error	σ(Å)	σ(Å)
5.11	0.2	2.6	0.52	23.8	2.3	0.30	12.1	2.5	-
7.72	0.25	2.0	0.78	25.5	2.4	0.36	24.9	2.8	-
10.2	0.28	2.1	0.62	27.6	2.4	0.28	23.3	2.9	2.2
12.3	0.30	2.6	0.40	7.27	2.6	0.36	6.22	3.0	2.2
14.2	0.32	2.1	0.58	22.4	2.1	0.44	14.4	3.0	2.0
17.4	0.35	2.1	0.38	15.0	2.3	0.26	16.1	3.2	2.2
20.7	0.40	1.9	0.36	38.5	2.1	0.36	40.2	3.8	3.0
25.2	0.40	2.0	0.38	25.1	2.1	0.36	26.6	4.6	3.2
31.9	0.40	1.6	0.36	91.5	1.8	0.66	55.6	5.5	3.6
40.6	0.26	2.0	0.36	41.3	1.8	0.36	36.8	7.0	-
48.6	0.43	1.6	0.58	67.5	2.1	0.58	67.5	7.5	-

Table 1. Parameters used in reflectivity fits, as described in text.

The fits described above cover the entire range of θ, excluding only the very low and very high angles as described in Chapter 3. Many results in the literature give a fit of the first Bragg peak, in order to provide a simpler fit for an estimate of σ. A compilation of roughness values calculated in this way has been published by Kortright[18] for a wide range of multilayers made with different materials by many investigators. Similar calculations have been performed for these multilayers, and these results are included in Table 1. Note that it is not appropriate to fit for Γ in this case, since the main effect of Γ is to change the relative heights of the peaks and these are fits of one peak only. The values of Γ used were those that gave the best fits with Model 2.

Finally, roughness values calculated from the soft x-ray reflectivities are given in the last column. These were calculated in the same way, using density and Γ from Model 2. Plots of all the fits are given in Fig. 7.

Roughness values from Model 2 and the two first-peak fits are plotted together in Fig. 8 for comparison. The most remarkable feature is the lack of agreement, particularly between the two sets taken from the CuK_α measurements. These are ostensibly measuring the same quantity on the same specimens, yet give very different values.

The explanation for this lies in the sensitivity of the measurements to different spatial frequencies of roughness. The roughness is distributed over a wide range of frequencies according to its power spectral density, and a fit to a measurement finds a value of roughness equal to the integral of the PSD over its

range of sensitivity. In an ideal scattering experiment the low-frequency limit would be given by the longest spatial wavelength that can be sampled, or half the beam width. In a real scattering experiment there is a finite slit in front of the detector, and the lowest frequencies scatter at such small angles from the specular that the rays fall inside the slit and are counted as part of the specular beam, and therefore will not contribute to the value of roughness found by the measurement. This lower frequency limit can be calculated from the grating equation. Fig. 9 shows a diagram of specular scattering at an angle Φ (measured from the normal) and a half-angle subtended by the slit of $\Delta\Phi$. The true incident and exit angle may differ by $\Delta\Phi$ and still be counted as a specular reflection, giving a spatial wavelength Λ

$$\Lambda = \frac{\lambda}{\sin(\Phi_{out} + \Delta\Phi) - \sin\Phi_{in}} \tag{10}$$

which will scatter a ray just striking the edge of the slit. Thus spatial wavelengths shorter than Λ, or frequencies higher than $f = 1/\Lambda$, will contribute to the measured value of roughness.

It is clear that the lower limit of the frequency depends on Φ as well as $\Delta\Phi$, and this is the reason for the different trends in the value of σ in Fig. 8. As d increases from 5Å to 50Å, the angle θ of the first Bragg peak decreases from ~9° to ~1°. The lower limit of frequency, calculated from the known slit width and detector distance, also moves by nearly an order of magnitude over this range. This will change the measured value of σ even if the samples are identical. For measuring a wide range of samples, such as these multilayers, we must describe the samples by their PSDs, not by the value of σ. Analyzing these results further requires learning what we can about the PSD.

The PSD can be measured by scanning-probe techniques on the surface, such as a profilometer, an AFM, or an STM, or by scattering experiments. Scattering measurements will be discussed more thoroughly in the next chapter, but have been used very little to obtain PSDs of multilayers because of the complexity of interpreting the results.

Some results from the literature will be useful for discussion here. Fig. 10 gives the PSD of three Mo/Si multilayers A, B, and C, measured by Windt [24]. The measurements were made with a Wyko profilometer and an AFM on the top surfaces of the multilayers and cover a wide range of spatial frequencies. The PSDs show a power-law dependence on frequency, consistent with a fractal roughness

found to occur[12] on many sputtered films and polished surfaces such as the substrate used by Windt. Such a fractal roughness is consistent with stochastic growth models where geometrically self-similar roughness features occur over a wide range of size scales.

The bold lines in Fig. 11 show Windt's measurement, represented by a best-line approximation, with similar measurements by Tobben[25] and Spiller[26]. Superimposed on the figure are markers for the ranges of sensitivity of the specular reflectivities in this study. If the experiment is measuring the first Bragg peak of a 5Å multilayer, the incidence angle is near 9° and the experiment will be sensitive to roughness between $3\mu m^{-1}$ and $10^4\mu m^{-1}$. If the experiment is measuring the first Bragg peak of a 50Å multilayer, the incidence angle is near 1° and the experiment is sensitive to roughness from $0.3\mu m^{-1}$ to $10^4\mu m^{-1}$, with the area under the curve considerably larger. Based on this alone, a trend of σ increasing with d could be found by fitting first peaks, even if all the multilayers had the same PSD. Furthermore, the range of sensitivity changes with angle in a given measurement. For the 50Å multilayer the lower limit would move from the 1° marker to the 9° marker as the incident angle increased. This rapidly decreases the area under the curve because of the power-law shape of the PSD, so that the measurement is dominated by the shorter range of sensitivity that obtains at the higher angles. For this reason, a single value of σ that fits the entire reflectivity best will often be too low to fit the first peak. This can be seen in the fit in Fig. 4.

The specular reflectivity does not give enough information, given its other uncertainties, to determine the PSD. But if a simple form of the PSD is assumed an estimate is possible. A simple power-law can represent the experimental PSDs well:

$$PSD = S(f) = \frac{K_n}{f^n} \tag{11}$$

To estimate the PSD, values of K_n and n were calculated, such that the roughness σ^2, found by the integral on page 7 with appropriate limits, gives the first-peak values at the ends of the d-spacing range, $\sigma = 2.6$Å for d = 5.11Å and $\sigma = 7.5$Å for a d = 48.6Å. This PSD gave $K_n = 8.62\times10^{-8}$ and n = 1.78. If the intermediate values of roughness are calculated from this PSD, one obtains the curve in Fig. 12. The experimental values are plotted as circles and they do not agree well.

It was shown in Ch. 4 that the multilayers become discontinuous near d = 15Å-20Å, which can be expected from the thin-film growth. The values of roughness in Fig. 7 do not follow a single $\sigma \propto t$ or $\sigma \propto t^{1/2}$ but appear to turn a corner near d = 18Å. If we postulate that the multilayers are continuous above this period, it is reasonable that the continuous and discontinuous multilayers would have different PSDs, with the discontinuous samples showing higher spectral weight at the higher frequencies where the film islands contribute as extra roughness features. For islands on the order of 20Å across, as observed in the plan-view TEM, this contribution would be at $f \cong 1/20Å = 500\mu m^{-1}$.

As a simple test of this, the experimental roughness values were divided into two groups above and below 18Å. A PSD was calculated from the lowest and highest roughnesses in each range, then used to calculated the roughnesses in between. The results are shown in Fig. 13 and the agreement is good. These two calculated PSDs are plotted in Fig. 11 as the light dotted lines. The different slope of the two curves shows the extra spectral weight at the higher frequencies for the discontinuous multilayers. The PSDs are clearly in a reasonable range, as compared with the other experimenters' results. The measurement of Tobben was made on a bare Si substrate, presumably comparable to those used in this study. Windt's specimens were grown on super-polished optical flats of similar roughness to Si wafers, while Spiller's multilayer was on a curved surface machined as a telescope mirror, expected to be rougher. It should be emphasized that it is a very simplified model to assume that a single power-law PSD can represent a range of different multilayers, but these calculations do demonstrate that PSDs consistent with the measured values of roughness are in a reasonable range.

Measurements cited earlier by Savage *et al.* studied W/C multilayers of periods 23-37Å and found roughness of 2-2.5Å, which was somewhat lower than the values from other researchers and the trend of results found by Kortright. Savage's measurements fit the entire range of $R(\theta)$ to about $\theta = 12°$, while the other results were fits of the first peaks only. Thus the lower roughness values are in very good agreement with the results of this study, which find σ of 4-6Å for first-peak fits and about 2Å for full range fits at these d-spacings.

Also added to Fig. 11 is a PSD calculated by the same method from the reflectivity results at $\theta = 45°$. In this case only the d-spacings above 15Å were used, since fewer values were available below and the

σ values below were noisier. This curve is comparable to the PSD from measurements of the same multilayers in the hard x-ray range.

The postulated PSDs have also used the simple assumption that a single power law represents the PSD over the entire range of frequencies. This is the only reasonable assumption for this level of analysis, since the reflectivity fits give a constant value of the roughness and therefore provide measurements only of the integral of the PSD over certain ranges. The PSD of the multilayer is expected[24] to contain contributions copied from the substrate by conformal growth, and contributions from the intrinsic roughness of the films. If the multilayer is discontinuous the contribution from the film islands may deviate from the power-law shape of the substrate contribution. Under this simple model this only appears as a change of slope while the real PSD probably has a more complex shape.

A remarkable feature of the very short period multilayers is that despite the loss of any continuous layered structure clearly seen by TEM and the x-ray scattering evidence in this chapter and in Chapter 7, the Bragg peaks are the same width as for the longer periods which have smooth continuous layers. This shows that even the discontinuous multilayers have long-range order extending over many multilayer periods, where one might expect the discontinuity to destroy strong periodicity from layer to layer. A reasonable explanation for this is that as the thin layers become discontinuous the islands of one W-rich layer begin to grow in the wells between the islands of the previous one, but the structure continues to grow periodically, as described in Sec. 6.3.1. The existence of long-range average periodicity near monolayer film thicknesses is at least evidence of the very smooth nature of the growing films, expected from the low sputtering pressures and the lack of columnar microstructure found to strongly reduce reflectivity at higher pressures in work by Stearns *et al.* cited earlier.[27]

6.4 Summary

Analysis of the specular reflectivity of W/B_4C multilayers over a wide range of d-spacings has shown that representing multilayer roughness by a single parameter is not sufficient for comparison of different measurements, unless they are made with the same experimental geometry. Individual measurements are sensitive only to a limited range of spatial frequencies of roughness, and may not

correlate with multilayer performance in applications sensitive to different frequencies. A more complete representation of the roughness is its power spectral density, which describes the frequency dependence of the roughness and can allow meaningful comparison of different measurements.

The W/B_4C multilayers showed different trends of roughness evolution with multilayer period, depending on whether roughness was calculated by fitting the first peaks or the entire angular range or the measured reflectivity. This can be explained by postulating a simple power-law PSD, consistent with known PSDs of substrates and similar multilayers, and taking into account the changing range of frequency sensitivity with the angle at which reflectivity is measured. While single values of σ could give satisfactory fits to the data, the trend of the change of σ with d-spacing is consistent with different power-law PSDs for multilayer periods below about d = 17Å and periods above. The change between the two regimes is consistent with the multilayer periods at which layer continuity is lost, according to HRTEM microstructural evidence, and with the periods at which the reflectivity begins to drop substantially below the calculated values for ideal structures. The change in slope of the two PSDs is also consistent with greater contributions to roughness at higher spatial frequencies, brought about by the breakup of the layers into separate W-rich islands which act as scattering centers and degrade reflectivity. The thickness of the W-rich layers from the fits of reflectivity are sometimes in conflict with the apparent values observed by TEM. This may be attibutable to variations in density in the W-rich layers which are not visible in TEM but cause a change in the effective structure factor and reflectivity of the multilayers.

Fits of x-ray reflectivity can give limited information on the PSD, by taking into account the changing frequency sensitivity of the experiment. A more complete characterization of the PSD by other techniques, conversely, would permit better interpretation of the specular reflectivity.

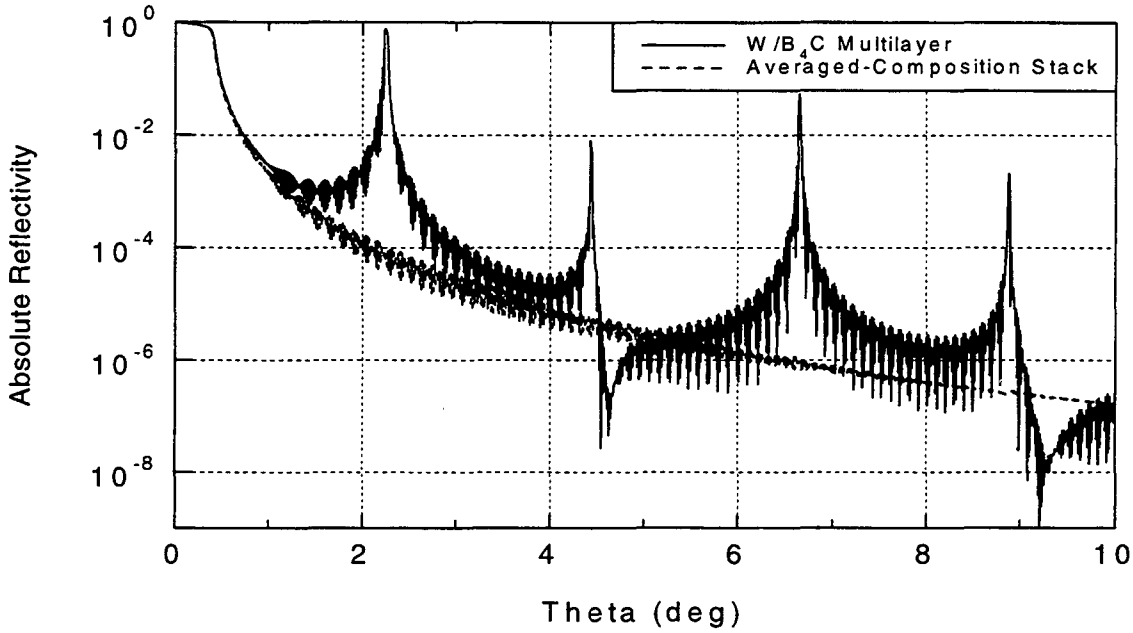

Fig. 1. Peaked curve: typical reflectivity vs. θ : calculated reflectivity (at λ = 1.54Å) for W/B_4C multilayer with 100 periods of 20Å, and W occupying 45% of the period (Γ = 0.45); other curve: reflectivity of same multilayer with composition modulation averaged out.

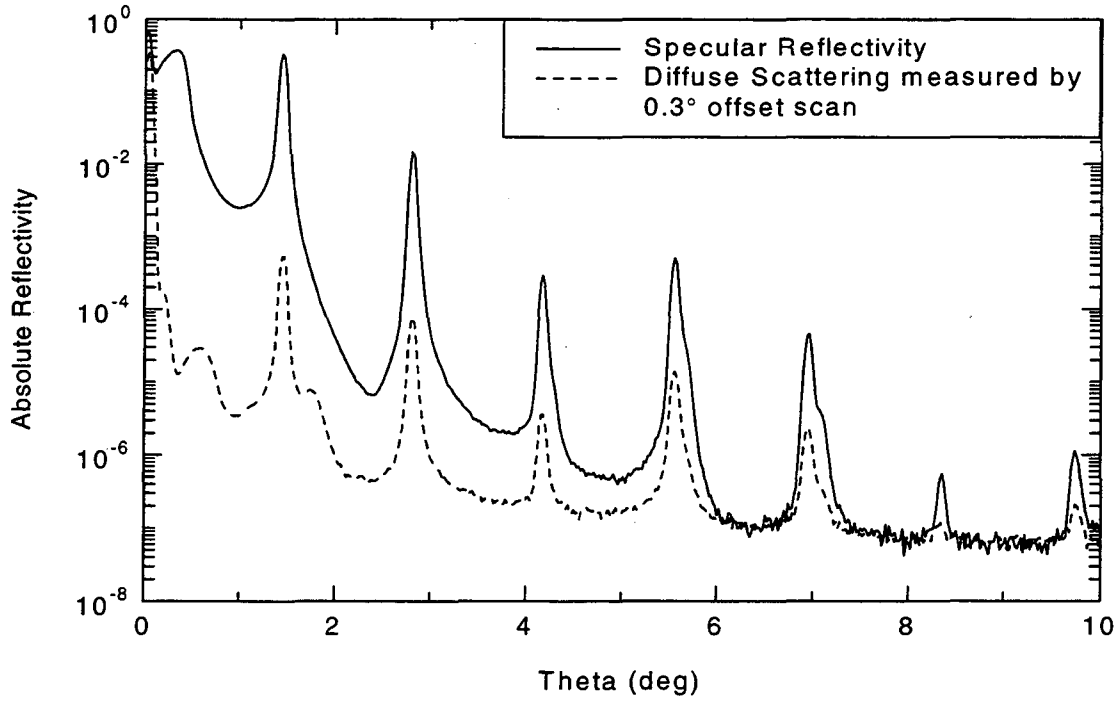

Fig. 2. Specular and diffuse reflectivity for 31.9Å W/B_4C multilayer. The noise level of both signals is near 10^{-7} – subtracting the diffuse extends the range significantly to near 10^{-8}. Note that the Bragg reflections appear in the diffuse scan, indicating that correlated roughness is present.

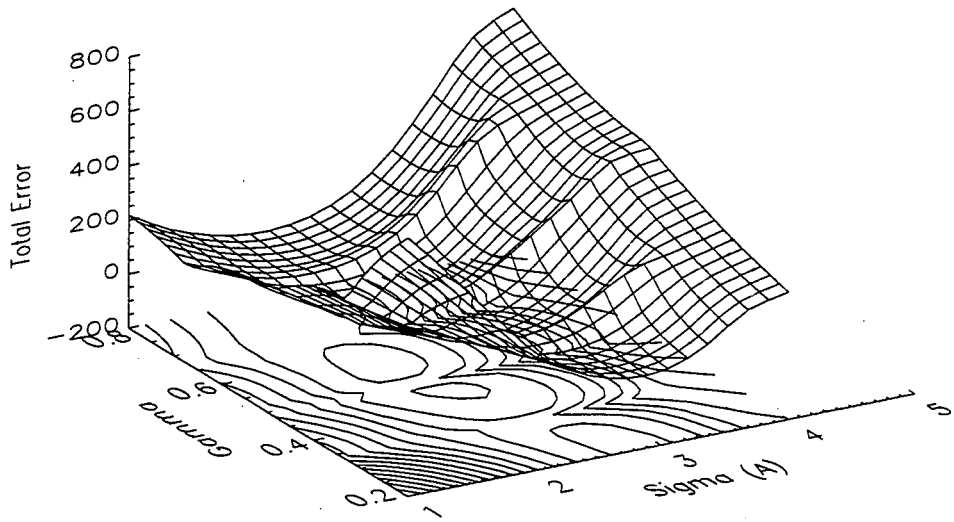

Fig. 3. Contour plot showing total error of fit (the error metric in Eq. XX summed over all q) as a function of the fit parameters Γ and σ. Ridges represent values of Γ which eliminate a Bragg peak and make a poor fit. The bottom plane shows contour lines of the fit surface.

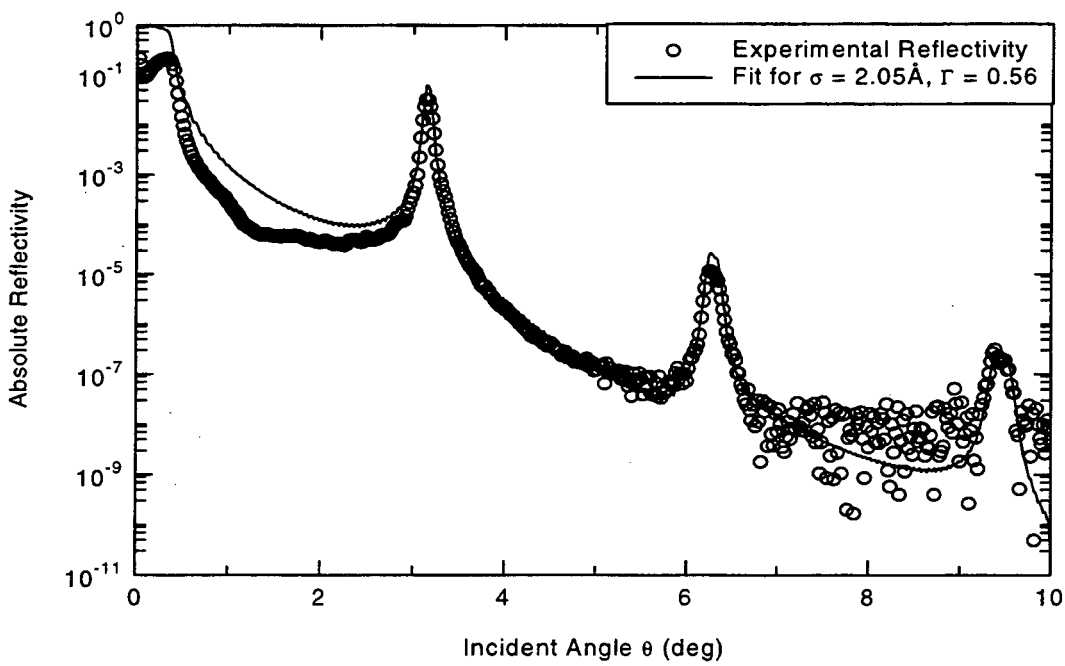

Fig. 4. Experimental curve fit in Fig. 3, with the best fit curve at σ = 2.1Å, Γ = 0.58. The period is d = 14.2Å. Near the critical angle the beam overfills the sample and the experimental values are inaccurate. The fit is above the data at the first peak, reflecting the higher value of σ that would be needed to fit the first peak only, as described in the text.

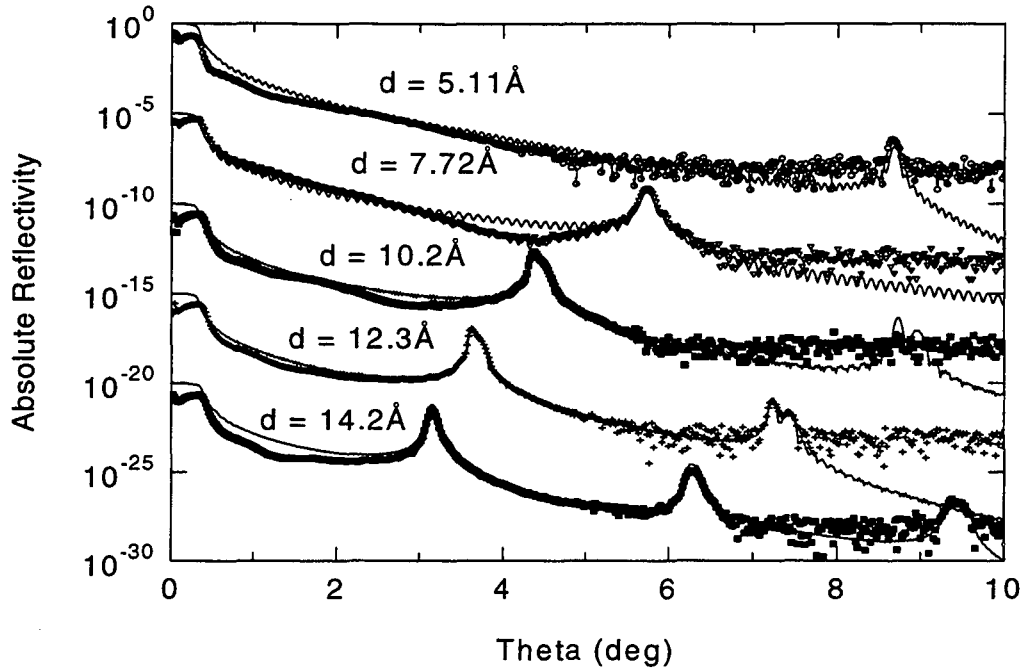

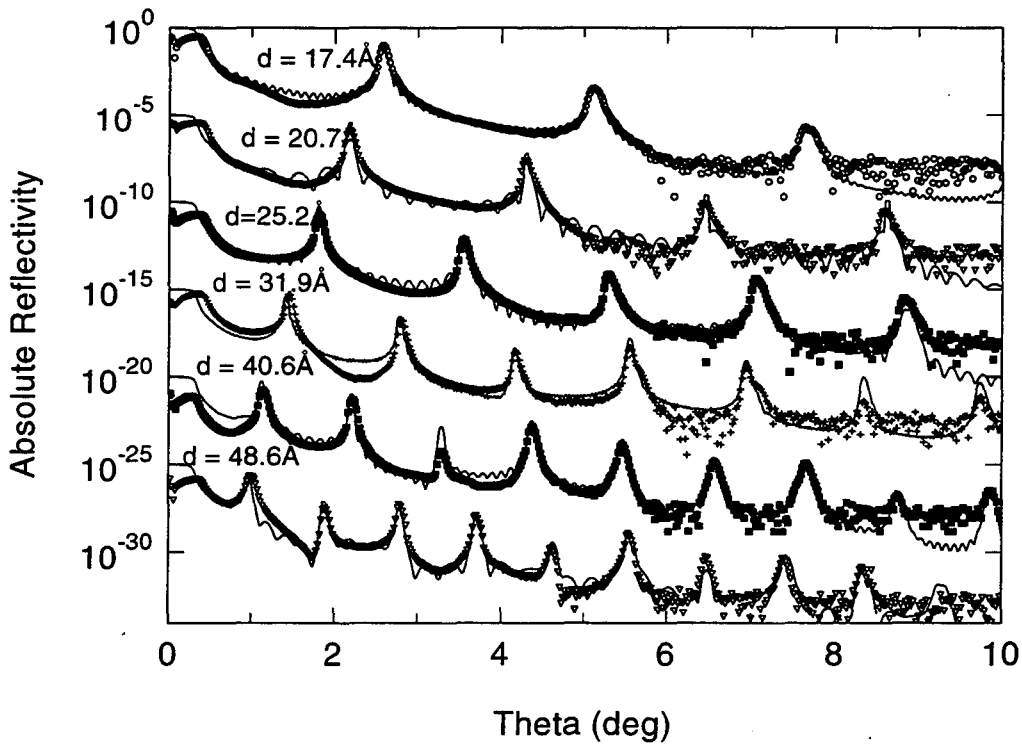

Fig. 5. Reflectivity of W/B_4C multilayers, 5Å ≤ d ≤ 50Å (points), and fits with Model 1 (lines). Splitting of the peaks can be observed in some samples, such as at d = 12.3Å.

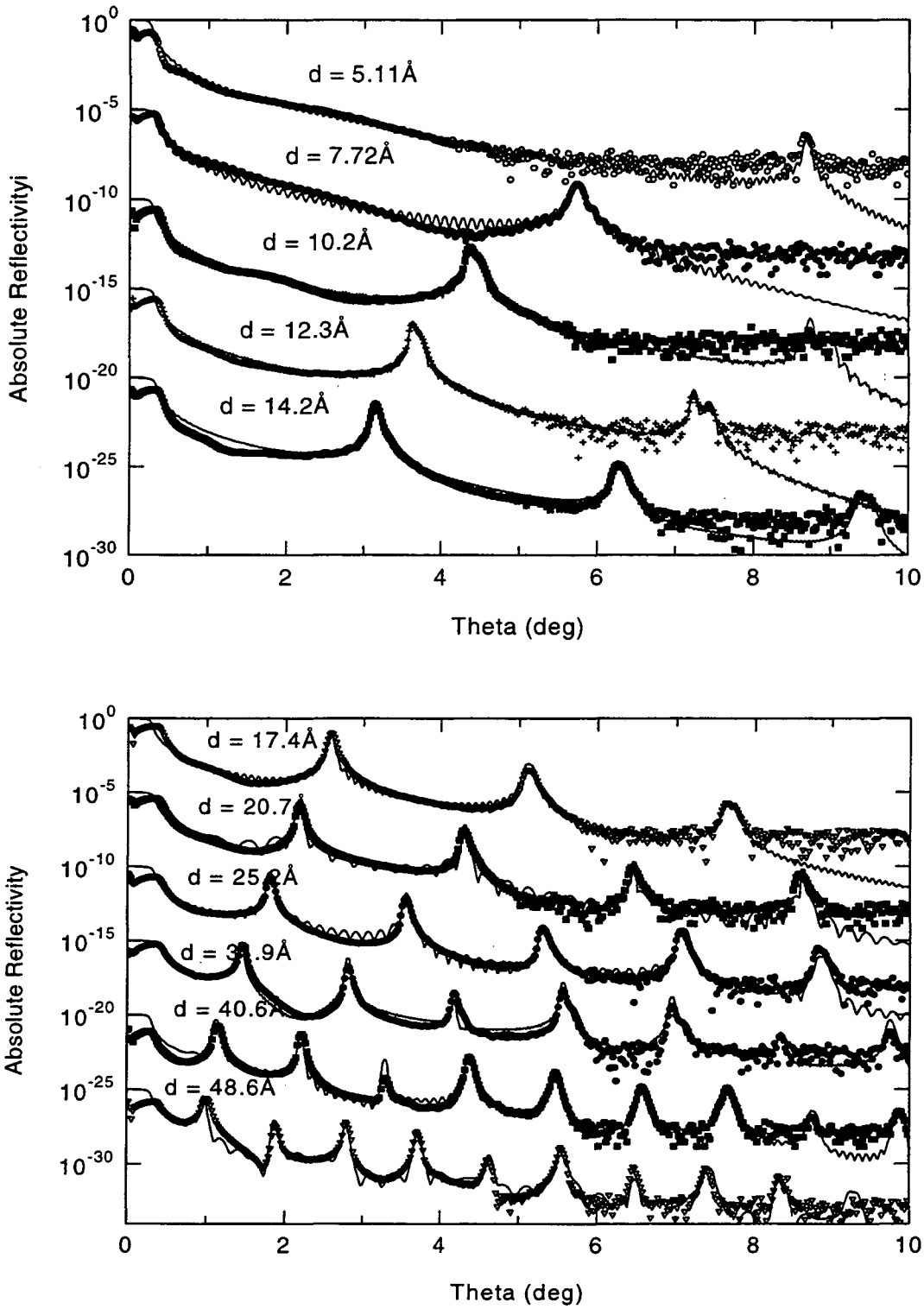

Fig. 6. Reflectivity at $\lambda = 1.54$Å of W/B_4C multilayers, 5Å ≤ d ≤ 50Å (points), and fits with Model 2 (lines).

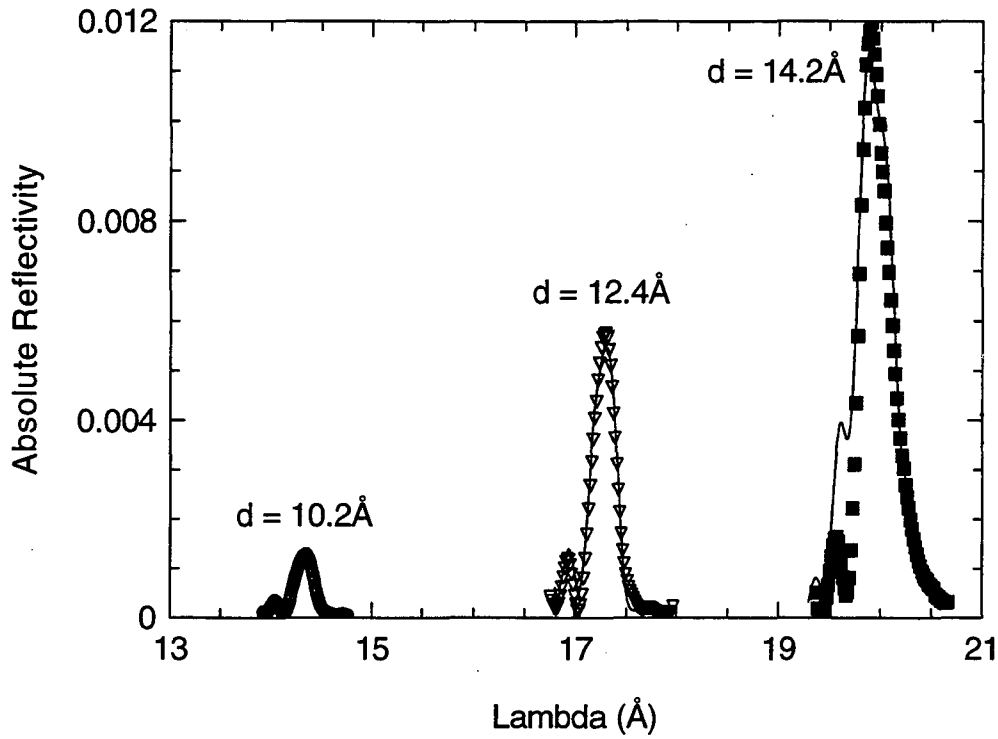

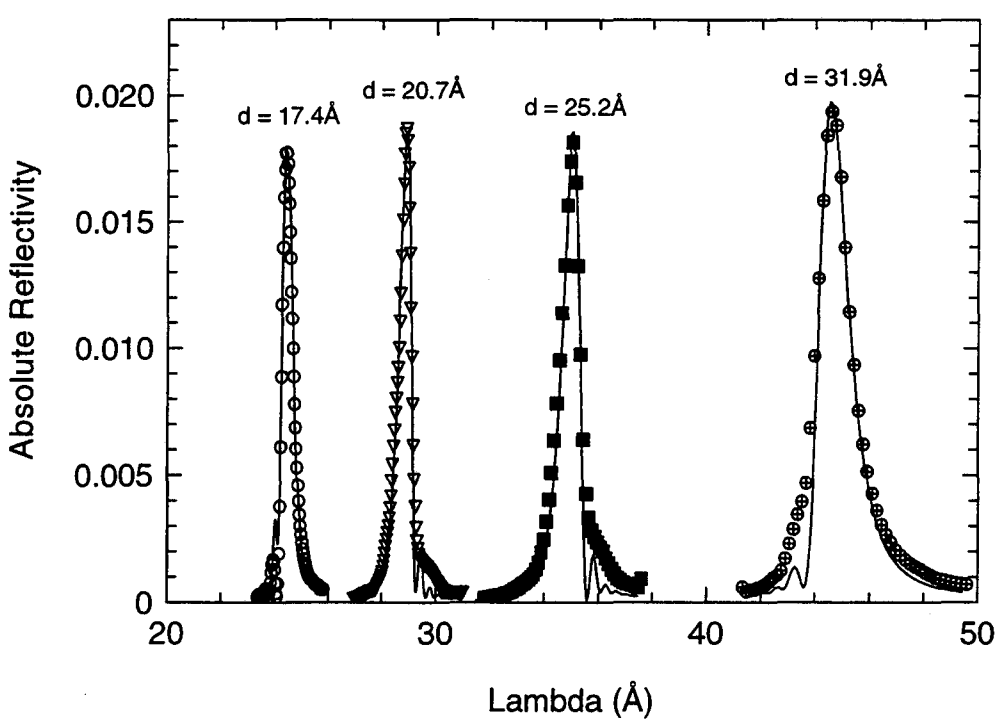

Fig. 7. Absolute reflectivities (at $\theta = 45°$) of W/B_4C multilayers (points) and fits (lines).

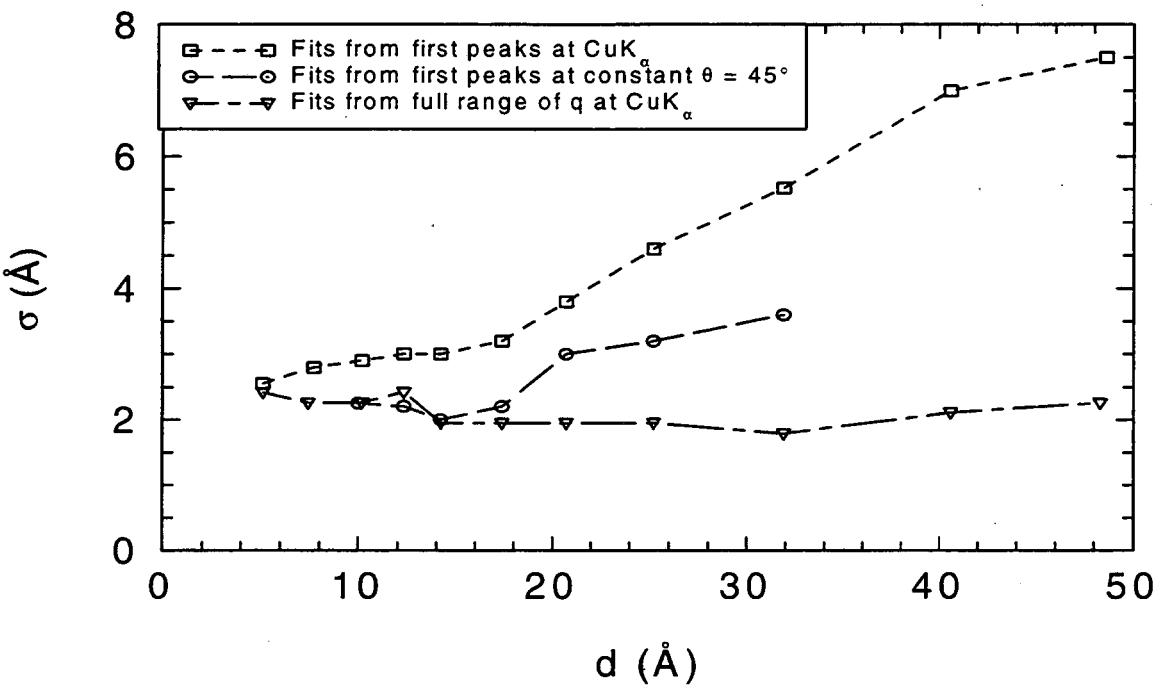

Fig. 8. Values of σ from fits at CuK_α (first-peak only and full-range) and at constant θ = 45°.

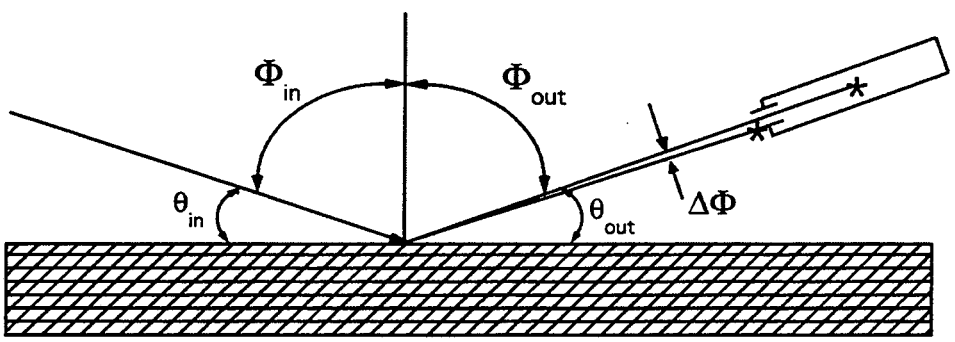

Fig. 9. Schematic of reflectivity measurement with a finite slit. Rays scattered within ±ΔΦ of specular condition pass through the slit and are counted as part of the specular signal.

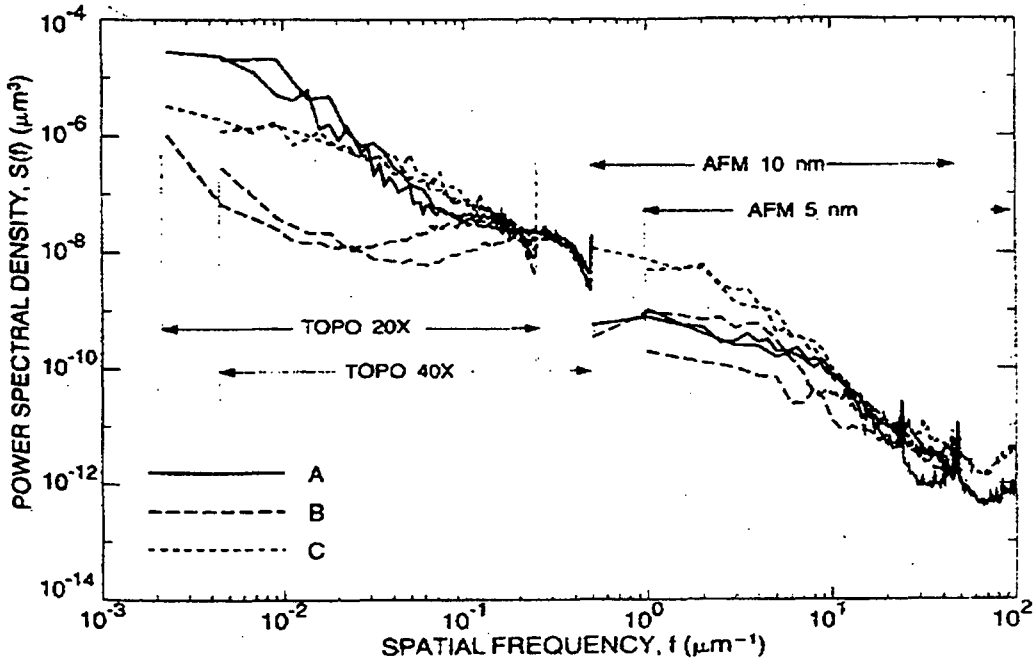

Fig. 10. Measurements of surface roughness of Mo/Si multilayers by Windt[24]. Two sets of measurements with a Wyko profilometer and an Atomic Force Microscope cover different ranges of spatial frequencies. The length scales given in the annotations give the scan lengths used in the measurements, which determine the lower limit of frequency sensitivity.

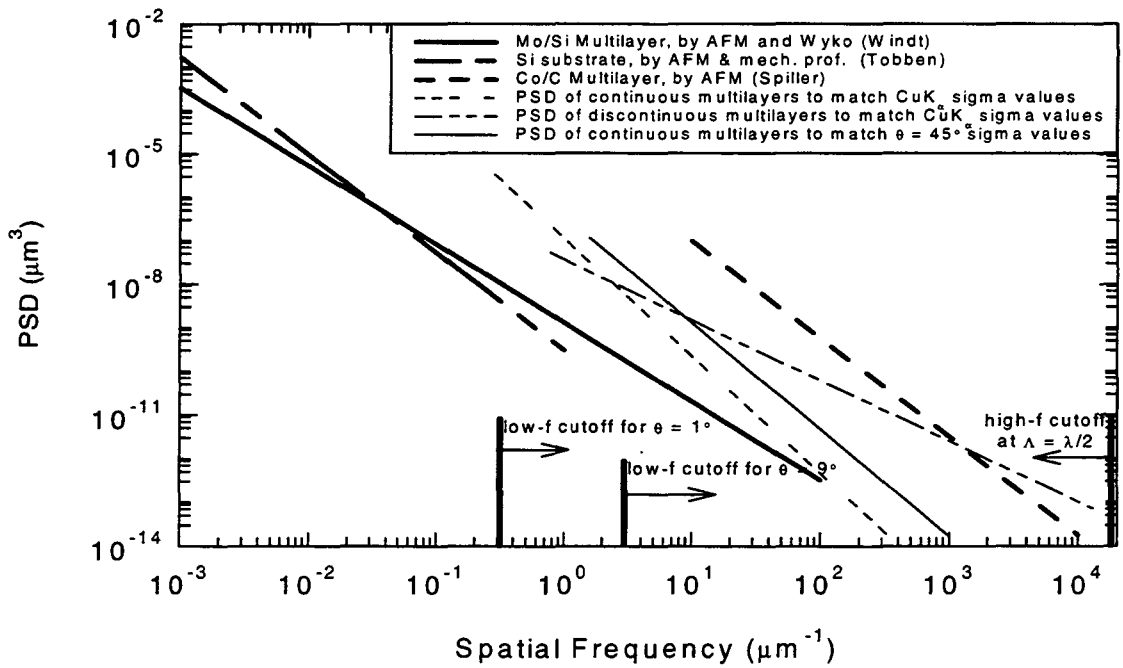

Fig. 11. Measurements of PSDs of multilayers and substrates from the literature (heavy lines). Also shown (light lines) are calculated PSDs to give the values of sigma measured for the multilayers in this study. The calculated PSDs are graphed only over the appropriate frequency range for the corresponding measurements.

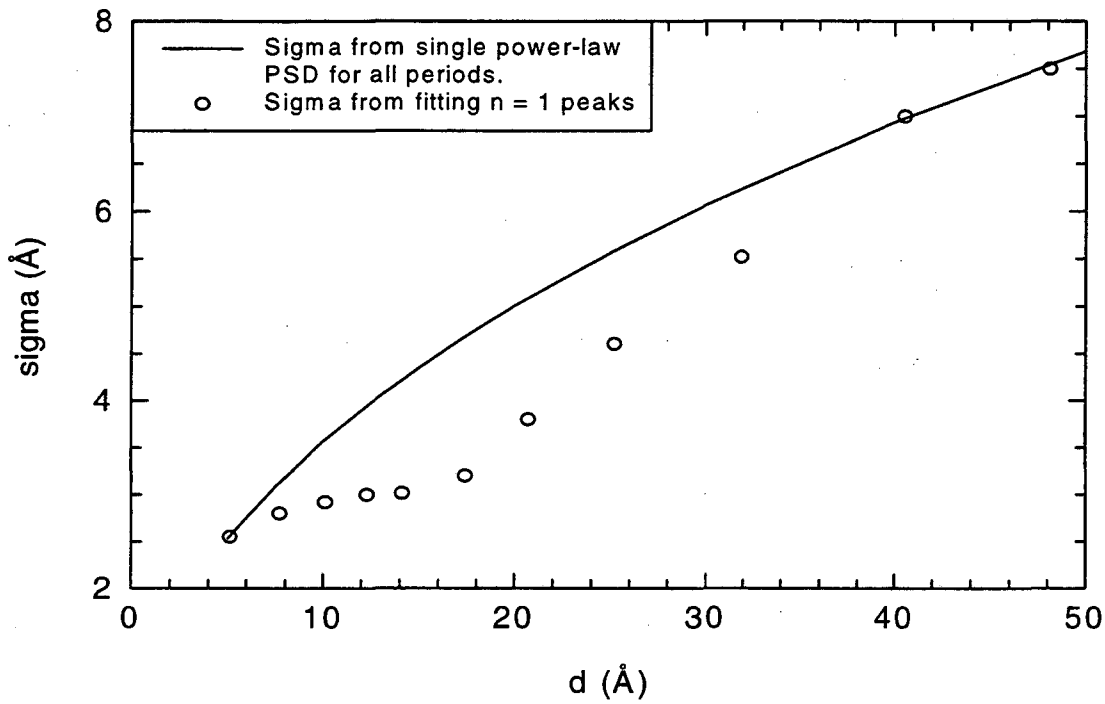

Fig. 12. Attempt to write a single power-law PSD consistent with the values of σ for d = 5Å and d = 48Å, then use it to calculate the trend of intermediate values of σ. Poor agreement indicates a single PSD is not appropriate.

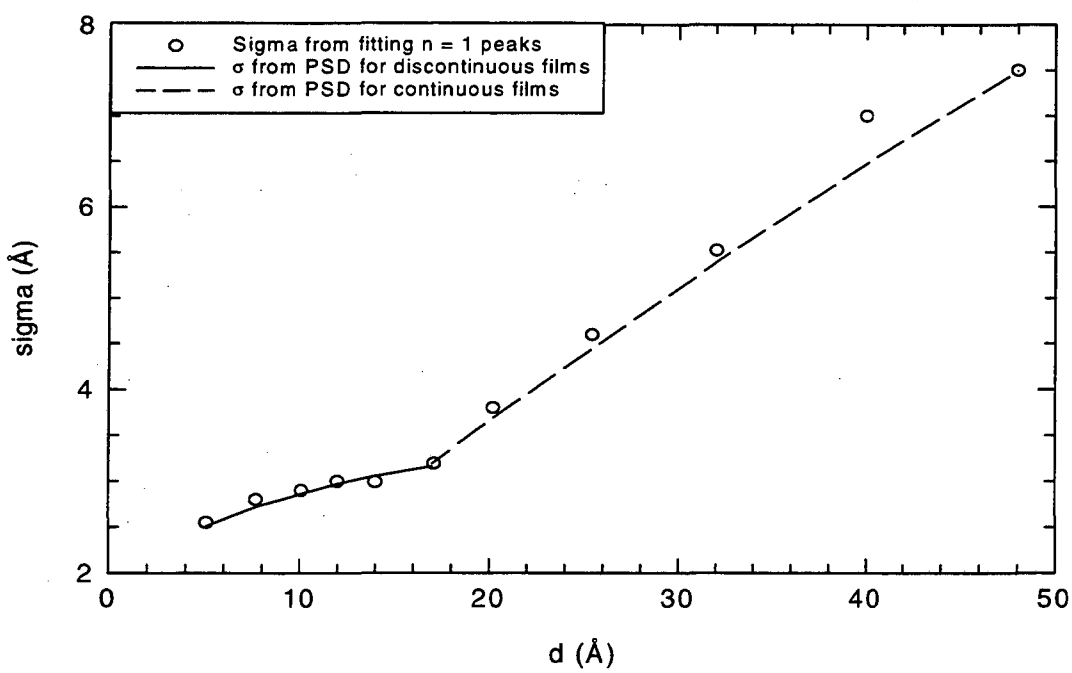

Fig. 13. If the values of σ are fit to two PSDs, one for d < 15Å and one for d > 15Å, corresponding to the discontinuous and continuous multilayers, the PSDs reproduce the trend of σ vs. d well.

References

[1]R. W. James, *The Optical Principles of the Diffraction of X-Rays* (G. Bell and Sons, London, 1958).

[2]L. G. Parratt, "Surface Studies of Solids by Total Reflection of X-Rays," Physical Review **95** (2), 359-369 (1954).

[3]J. DuMond and J. P. Youtz, Journal of Applied Physics **11**, 357 (1940).

[4]H. E. Cook and J. E. Hilliard, "Effect of gradient energy on diffusion in gold-silver alloys," Journal of Applied Physics **40** (5), 2191-8 (1969).

[5]E. S. K. Menon, P. Huang, M. Kraitchman *et al.*, "Nonlinear diffusion in Cu-Au multilayer thin films," Journal of Applied Physics **73** (1), 142-9 (1993).

[6]E. S. K. Menon and D. de Fontaine, "Effects of nonlinear diffusion on diffraction from binary multilayers," Scripta Metallurgica et Materialia **27** (4), 395-400 (1992).

[7]A. L. Greer, "Diffusion and reactions in thin films," presented at the Symposium B of the 1994 E-MRS Spring Conference, Strasbourg, France, 1994 (unpublished).

[8]D. S. Sivia, W. A. Hamilton, G. S. Smith *et al.*, "A novel experimental procedure for removing ambiguity from the interpretation of neutron and X-ray reflectivity measurements: 'Speckle holography'," Journal of Applied Physics **70** (2), 732-8 (1991).

[9]S. Manninen and K. Hamalainen, "High-resolution inelastic X-ray scattering study of the boron K absorption edge," Physical Review B (Condensed Matter) **45** (7), 3878-81 (1992).

[10]B. L. Henke, E. M. Gullikson, and J. C. Davis, "X-ray interactions: photoabsorption, scattering, transmission, and reflection at E=50-30000 eV, Z=1-92," Atomic Data and Nuclear Data Tables **54** (2), 181-342 (1993).

[11]Tai Dung Nguyen, "Microstructure-Interface-Property Relationships in Nanometer-Period X-Ray Multilayers," PhD, University of California, Berkeley, 1993.

[12]E. L. Church, "Fractal surface finish," Applied Optics **27** (8), 1518-26 (1988).

[13]P. Debye, "Uber die Intensitatsverteilung in den mit Rontgenstrahlungerzeugten Interferenzbildern," Verh. d. Deutsch. Phys. Ges. **15**, 738 (1913).

[14]I. Waller, "Zur Frage der Einwirkung der Warmebewegung auf die Interferenz von Rontgenstrahlen," Z. Physik **17**, 398 (1923).

[15]D. G. Stearns, "The scattering of X-rays from nonideal multilayer structures," Journal of Applied Physics **65** (2), 491-506 (1989).

[16]A. P. Payne and B. M. Clemens, "Influence of roughness distributions and correlations on X-ray diffraction from superlattices," Physical Review B (Condensed Matter) **47** (4), 2289-300 (1993).

[17]T. D. Nguyen, R. Gronsky, and J. B. Kortright, "Microstructure-roughness interrelation in Ru/C and Ru/B_4C X-ray multilayers," presented at the Evolution of Surface and Thin Film Microstructure Symposium Evolution of Surface and Thin Film Microstructure Symposium, Boston, MA, USA, 1992 (unpublished).

[18]J. B. Kortright, "Status and limitations of multilayer X-ray interference structures," Journal of Magnetism and Magnetic Materials **156** (1-3), 271-5 (1995).

[19]A. E. Yakshin, I. I. Khodos, I. M. Zhelezniak *et al.*, "Fabrication, structure and reflectivity of W/C and W/B/sub 4/C multilayers for hard X-ray," Optics Communications **118** (1-2), 133-42 (1995).

[20]F. E. Christensen, Zhu Shou-Hua, A. Hornstrup *et al.*, "X-Ray Study of State-of-the-Art Small d-Spacing W/BC Multilayers," Journal of X-Ray Science and Technology **3** (1-13), 1 (1991).

[21]D. E. Savage, Y. H. Phang, J. J. Rownd *et al.*, "Determination of interfacial roughness correlation in W/C multilayer films: comparison using soft and hard X-ray diffraction," Journal of Applied Physics **74** (10), 6158-64 (1993).

[22]R. A. Cowley and C. Lucas, "X-ray scattering measurements of silicon oxides on silicon," Colloque de Physique C **7**, 145-52 (1989).

[23]D. G. Stearns, R. S. Rosen, and S. P. Vernon, "Fabrication of high-reflectance Mo-Si multilayer mirrors by planar-magnetron sputtering," Journal of Vacuum Science & Technology A (Vacuum, Surfaces, and Films) **9** (5), 2662-9 (1991).

[24]D. L. Windt, W. K. Waskiewicz, and J. E. Griffith, "Surface finish requirements for soft X-ray mirrors," Applied Optics **33** (10), 2025-31 (1994).

[25]H. Tobben, G. Ringel, F. Kratz *et al.*, "The use of Power Spectral Density (PSD) to specify optical surfaces," presented at the Specification, Production, and Testing of Optical Components and Systems, Glasgow, UK, 1996 (unpublished).

[26]Eberhard Spiller, *Soft X-Ray Optics* (SPIE Optical Engineering Press, Bellingham, Wash. USA, 1994).

[27]S. P. Vernon, D. G. Stearns, and R. S. Rosen, "Ion-assisted sputter deposition of molybdenum-silicon multilayers (for soft X-ray optics)," Applied Optics **32** (34), 6969-74 (1993).

Chapter Seven

Diffuse Scattering Studies

7.1 Introduction

In the previous chapter the specular reflectivity was analyzed in some detail, including analysis of the intensity missing from the specular because of roughness and interdiffusion lowering the reflectivity. A diffuse interface will have lower reflectivity than an abrupt one, and the extra intensity is simply transmitted through the multilayer. A rough interface also has lower reflectivity, but the extra intensity is scattered (elastically) away from the specular rather than transmitted. Some analysis of how this diffuse intensity is distributed was necessary to properly interpret the specular results in the previous chapter, since some diffuse scattering is inevitably counted with the specular in a real experiment. But the diffuse scattering can of course be measured directly, and its angular distribution is a rich source of information on the various inhomogeneities that cause it. In this chapter two diffuse-scattering measurements, one in transmission and one in reflection, are applied to the same set of multilayers. Small-angle scattering is used to place the scattering vector in the multilayer plane to look for variations in density from very rough or discontinuous films, and rocking curves in the reflection geometry also use an in-plane scattering component to measure roughness contributions. Application of the results to direct determination of the frequency dependence of the PSD will be presented.

7.2 Small-Angle Scattering

Small-Angle X-ray Scattering, or SAXS, is a technique with a large literature spanning many years. It consists of measuring transmitted intensity through a thin specimen, and looking for radiation scattered at small angles from the transmitted beam by inhomogeneous structures in the specimen. Since the scattered beam and the incident beam are nearly collinear, the scattering vector **q** is in the plane of the thin specimen, in contrast to a measurement in reflection, where it has at least a large component normal to the surface. In the case of multilayers this puts **q** in the plane of the layers and lets us measure just the type of in-plane inhomogeneity that a discontinuous film would have. For hard x-rays the available length scales are in the tens or low hundreds of Angstroms, which is suitable for the periods of these multilayers.

The Small-Angle X-ray Scattering (SAXS) measurement is sensitive to fluctuations in the atomic scattering factor, or essentially in the electron density, neglecting anomalous scattering effects. It is most usually applied to study phase separation or ordering on small size scales difficult to observe by other techniques. The scattered intensity is recorded as a function of angle from the transmitted beam. If the specimen is homogeneous in the direction of the scattering vector no signal will be observed. If the specimen is inhomogeneous the total SAXS signal will depend on the mean-square of the density fluctuation, and its angular distribution will depend on the shape and size of the inhomogeneity. Because the signal is weak an intense source and long collection times are generally needed, and such studies are commonly done at synchrotrons. For this study the soft x-ray metrology beamline 6.3.2 at the Advanced Light Source, LBNL was used, and for the hard x-ray (CuK_α) the rotating-anode generator used to measure reflectivity also had marginally sufficient intensity for SAXS.

In the usual practice of SAXS, the thin sample is kept fixed, and the scattered signal is collected in parallel by a fixed array of detectors behind the sample, encompassing scattering angles of a few degrees. In this study the scattering angles were as high as 20° in the hard x-ray and 120° in the soft x-ray, and the samples were tilted at half the detector angle to keep the scattering vector in the sample plane. With this rotation of the sample the result of the measurement is equivalent to small angles with a fixed specimen, so the term "SAXS" is still used, despite the difference from the conventional SAXS setup.

7.2.1 Experiment

For SAXS measurements the multilayers deposited on Si_3N_4 membranes were used, as described earlier for the spectroscopy studies. The first measurements were made at CuK_α on the rotating-anode generator, with the beam slitted to 0.5mm X 1.5mm. A set of slits 200mm in front of the detector was adjusted to minimize the contribution from air scatter near the specimen. The sample was carefully translated in X and Y to ensure that the beam passed through the center of the 3mm square membrane. During the scan the sample was rotated at half the detector angle, just as in a $\theta/2\theta$ reflectivity scan, to ensure that the scattering vector was always in the plane of the layers and would not begin to measure the multilayer periodicity. A scan with no specimen was also made to measure the air scatter and tails of the incident beam.

The second set of SAXS measurements was performed on BL6.3.2 at the ALS. The scattering vector was kept in the multilayer plane as before. Because of the shape of the sample holder only angles up to $2\theta \cong 120°$ were available; beyond this angle the holder blocked the beam. An energy of 700eV was selected, which places features of the size scale expected in that angle range, and conveniently is near enough to the maximum energy available through the beamline optics that the problem of higher harmonics in the incident beam was eliminated. This energy is also sufficiently far from absorption edges of the materials in the multilayers and in the membranes that anomalous scattering could be neglected. A parasitic scatter curve, taken on an empty sample holder, was also recorded over the same angles. To count very low intensities a Channeltron photomultiplier was used as a detector. While this detector can count as low as about 1 part in 10^{10} of the full beam, it cannot withstand the full incident beam itself, so normalization of the results by the intensity of the full beam must be estimated. For the change of the beam strength over the time of the experiment a "nominal I_0" signal is collected by measuring the photoelectron current from one of the beamline's focussing mirrors. A 5mm round aperture made of two sheets of aluminum foil was placed in front of the detector to provide some collimation of the signal scattered from the sample and block out stray light from elsewhere in the chamber.

7.2.2 Data Reduction

Background Subtraction: For the measurements at 700eV the background scattering was quite small as shown with the results, so the parasitic scatter scan could be subtracted directly from all the signals. For the meaurements at CuK_α the background signal was larger than the measured signal. For this case the background scan was fitted with two exponential functions:

$$\frac{I}{I_0} = a\exp(-b\theta) + c\theta^{-\frac{1}{2}} \tag{1}$$

to give a smooth background that could be subtracted from all the scans.

Absorption of the membrane and specimen: These quantities were calculated from other measurements. For the membrane the absolute transmissivity had been measured during the spectroscopy studies at lower energies, and its thickness was calculated from those values assuming the bulk density of Si_3N_4. For the multilayers the average composition was known from the rate tests when the specimens were made (and their content of W, the dominant scatterer, was verified by the fluorescence measurements described in Chapter 3). The thickness was known accurately from the measurements of the d-spacing so the absorption could be calculated.

Conversion to Absolute Scattering Cross Section: With the steps above the data for absolute intensity I/I_0 could be converted to scattering cross sections according to

$$\frac{d\Sigma}{d\Omega} = \frac{I}{I_0}(k)\frac{1}{t}\frac{1}{e^{-\mu t}}\frac{r^2}{\varepsilon\Delta a} \tag{2}$$

where I/I_0 is the measured absolute intensity, t is the sample thickness, $\exp(-\mu t)$ is the absorption of the specimen, ε is the detector efficiency, and $r^2/\Delta a$ is the reciprocal of the solid angle subtended by the detector. The formula above assumes that I_0 is known exactly but that I must be adjusted for the detector efficiency. For the CuK_α data the same detector actually measured both so this factor cancels. For the

700eV data I_0 was estimated from the known characteristics of the beamline. At an energy of 700eV with the 1200 line/mm monochromator grating the beam gives about $4x10^{10}$ photons/sec/0.1%bandwidth, or $6.4x10^{10}$ photons/sec at the monochromator's energy resolution of $\Delta E/E \cong 1/600 \cong 0.16\%$. The detector was assumed to have an efficiency of 5% based on past estimates by the beamline designer. These numbers are necessarily approximate as the current in the storage ring varies with time between refills and the beamline was not carefully characterized in advance for a quantitative SAXS experiment but just to see if such scattering could be observed. The 700eV data were eventually scaled up by a factor of 45 to reach an acceptable fit. This missing intensity is probably an overestimation of I_0. Finally, the data were adjusted for the decay of the incident beam over time, by comparing the nominal I_0 from the mirror current to its initial value and scaling the real signal up accordingly.

7.2.3 Results

Scattering curves at CuK_α are presented in Fig. 1. The data represent scans counting at about 120sec/point and the data are noisy – to show the features more clearly the data have been smoothed by an averaging window of ±2 points (much smaller than features of interest). For clarity, the curves are displaced with additive factors as labeled. The background subtraction leaves a signal averaging to zero for the flat regions of all the curves indicating there truly is no signal there. To represent the curves as measured the ordinate is left in absolute I/I_0.

The results at 700eV are presented in Fig. 2. No smoothing was performed in this case. The ordinate is counts per second for 68 seconds per point.

7.2.4 Analysis

For a very simple analysis one can think of the SAXS signal as representing a broad Bragg peak for some periodicity in the multilayer plane. For a peak at $\theta = 2.5°$, like the one observed for the 6Å multilayers, this gives $d = \lambda/2\sin\theta \cong 17.6$Å at $\lambda = 1.54$Å, or for a peak at $\theta = 30°$ with $\lambda = 17.7$Å, d = 17.7Å. The breadth of the peak would indicate a large variation in spacing. This is consistent with island

sizes for growing films a few atoms thick, and likely several more atoms wide, with a wide variation in size.

Using existing theory for small-angle scattering, however, we can make a more sophisticated analysis, deriving quantitative information from the height, breadth and position of the peaks. The formalism used here is taken from work by Rice[1] on phase separation in solid solutions of Mo-Ge and other systems.

For the simplest possible theoretical model, the scattered intensity of a dilute solution of spherical particles of one phase in a matrix of another is

$$I = I_e(k) N V_p^{\,2} (\rho_p(E) - \rho_m(E))^2 \Phi^2(kR) \tag{3}$$

where $I_e(k)$ is the intensity that would be scattered from a single electron, N is the number of particles, and V_p is the volume of a particle. The density ρ_p of the particles and ρ_m of the matrix is the effective electron density, i.e. the electron density scaled by the atomic scattering factor at the wavelength of interest:

$$\rho_p(E) = \frac{N}{V}[m_W f_W + m_B f_B + m_C f_C] \tag{4}$$

(with a similar equation for $\rho_m(E)$) where the m_i are the atomic fractions of the species i in the particle. Finally, the function $\Phi^2(kR)$ is the form factor for the spherical particles and is given by

$$\Phi(kR) = 3\frac{\sin(kR) - kR\cos(kR)}{(kR)^3} \tag{5}$$

For the case of these multilayers, the volume fraction of the sample occupied by the particles is on the order of 0.5, since it is approximately Γ, the fraction of the period occupied by the scattering layer. Since this is not a dilute solution a correction can be added for secondary scattering between particles:

$$I = I_e(k) N V_p^{\,2} (\rho_p(E) - \rho_m(E))^2 \Phi^2(kR) \left[\frac{1}{1 + 8c\Phi(2kR)} \right] \tag{6}$$

where c is the volume fraction occupied by the particles.

To take into account the experimental geometry this expression can be rewritten for the absolute scattering cross section:

$$\frac{d\Sigma}{d\Omega} = r_e^2 c V_p (\rho_p(E) - \rho_m(E))^2 \Phi^2(kR) \left[\frac{1}{1 + 8c\Phi(2kR)} \right] \tag{7}$$

where r_e is the classical electron radius. This expression was used to fit the data. As with the x-ray reflectivity calculation it was assumed that the matrix was bulk B_4C. There are then three parameters in the equation: the volume fraction c, the particle density ρ_p, and the particle size R. These are not independent, however: since the average composition of the specimen is known, the volume fraction occupied by the particles determines their composition. The average composition of the multilayer is given by bulk W layers of thickness $\Gamma_{nom}d$ and bulk B_4C layers of thickness $(1-\Gamma_{nom})d$ (as was verified for W by the x-ray fluorescence measurements in Ch. 3). When the W layer expands by absorbing some of the B_4C layer, a mass-balance calculation shows that the mass density of the W-rich layers is

$$\rho = \rho_W + \rho_{B_4C} \left(1 - \frac{\Gamma_{nom}}{\Gamma_{act}} \right) \tag{8}$$

and its composition is

$$W(B_4C)_{A(\frac{c}{\Gamma_{nom}} - 1)} \tag{9}$$

where $A = \rho_{B4C}(M.W)_{.W}/\rho_W(M.W)_{.B4C}$ From the composition we can calculate mole fractions m_W, m_B and m_C of the three constituents in the W-rich particles. With the atomic scattering factors (taken from the tabulated values by Henke[2]) it is simple to calculate $\rho_p(E)$ according to Eq. (4). This provides the effective electron density in terms of c, which relates two of the parameters, leaving a two-parameter fit. The average separation of the particles is already determined by their volume fraction and composition, since the average composition is fixed.

A slight refinement of this model takes into account that the particles are nuclei of growing films and they are competing for the arriving W atoms during sputtering. Therefore, like precipitates surrounded by depletion zones, it is unlikely that two particles would abut each other, but rather a buffer zone would exist between them. This can be built into the model by replacing the volume fraction c in the interparticle scattering term with

$$\eta = \frac{V_s}{V_p} c \tag{10}$$

where $V_s = (4/3)\pi(R+\sigma)^3$ is the the volume of a particle plus its buffer zone of radius σ. This refinement gave a slight improvement of fit with little change in the other parameters, and will be presented below. Only the results at d = 6Å and d = 14Å were fit, as the higher d-spacings were nearly featureless, though in the soft x-ray results, the 22Å multilayer may show some small intensity, at a lower angle near 30° consistent with the trend of the other two peaks.

7.2.5 Fits and Discussion

The fits to the CuK_α results are presented in Fig. 3. The intensities have been converted to $d\Sigma/d\Omega$ as described above, and the angles converted to the scattering vector in the plane, $q_x = 4\pi\sin\theta/\lambda$, where θ is half the detector angle 2θ even though the actual sample surface is now at 90° to the usual $\theta/2\theta$ geometry. The fits reproduce the experimental curves quite well, with the largest errors occurring at the very low angles for the CuK_α fits. This is to be expected as this region of the curve was on a steep slope of the edge of the incident beam where the subtraction of the tails of the incident beam may not have been accurate. This is the reason for the non-physical negative values of the scattering cross-section for the 6Å multilayer at the lowest angles. The fits also tend to be narrower than the experimental curves. This would likely be fit better in a more sophisticated model including dispersion of the particle sizes and separations, which brings a dispersion in the scattering distances and tends to widen SAXS features.

The fits show a particle size of about 24Å for the d = 6Å multilayer and about 32Å for the 14Å multilayer. In the W/B_4C system the surface energy of W on B_4C and B_4C on W is necessarily very low, or such thin layered structures could not be formed. The "layer growth" model would therefore be expected, with each film forming islands as thin as 1 atom, which grow to much larger dimensions laterally before thickening. In this model islands of 10-15 atoms across are very reasonable. In the plan-view TEM individual islands can be seen in the thinnest area near the edge of the 6Å multilayer, which measure about 20Å across, very consistent with the SAXS results. As the islands grow, some would coalesce and the average size would increase, which is also consistent with the results. The densities are reasonable, though somewhat higher than the densities calculated from the value of Γ observed by TEM in the 20Å and 30Å multilayers. The greatest intermixing (and the lowest densities of the W-rich phase) would be expected at the lowest d-spacings, so a density at least as low would be expected. However, if the film is discontinuous the density of the particles must be greater than the average density of the film, which is what would be calculated from the thickness observed in cross section.

The model assumes that the spherical particles of composition different from the matrix are the primary source of diffuse scattering in the plane. If the structure contains voids they can also give a diffuse signal. The experiment itself is sensitive only to a difference of the density, and would give the same result for voids of density 0 in a matrix of density 2, as it would for particles of density 4 in a matrix of density 2. However, to produce the SAXS signal observed, the voids would have to exist at a volume fraction similar to that of the W-rich particles, about 0.5-0.6. If the sample had such a large void fraction it would be observable by TEM, and the loss of density would be reflected by a change in the apparent sputtering rate. Neither of these effects was observed. As discussed in Chapter 2, the low sputtering pressure is selected to produce bombardment of the growing film and a corresponding high film density; it is unlikely that a large volume fraction of voids would appear, for the discontinuous multilayers only, under these conditions. Rice[1] found a void volume fraction of 0.001 and any void contribution in this study must be similarly small.

The total area under the SAXS signal depends only on the mean-square variation of the effective electron density. This quantity is independent of the sample size and the particle size and shape and is therefore called the invariant

$$Q = \int_0^\infty \frac{d\Sigma}{d\Omega}(k)dk \tag{11}$$

For these results this quantity is not constant but decreases significantly from d = 6Å to d = 14Å and is no longer measurable for larger d-spacings. To account for this the calculated curve at d = 14Å was scaled down by a factor of 2.65. This occurs because the layers are partly continuous at d = 14Å, so the variation of the electron density is reduced in the in-plane direction as the W and B_4C are increasingly segregated into their layers. The model of spherical precipitates clearly breaks down for a layered structure: the spherical model assumes that material is conserved, and that if the material is separated into two phases the density of the W-rich phases will vary inversely with its volume fraction. But it cannot account for the material phase-separating into layers parallel to the scattering vector, where there is a large density variation but it is invisible to the experiment. While a model could be constructed to account for this, it would be unable to measure the particle density without detailed assumptions about the extent of the layered sample texture as a function of d, while the purpose of this experiment was to demonstrate the phase-separated nature of the multilayers at the smallest d-spacings where the spherical model is realistic.

Fits for the measurements at 700eV are presented similarly in Fig. 4. The data treatment was the same as for the CuK_α measurements, except that the experimental intensities were all scaled up by a factor of 45. This is not unexpected because of the large uncertainty of the relation between the Channeltron detector counts and the absolute intensity. The particle sizes and densities are very similar to the previous values – particles of diameter 25Å and 32Å. There is a similar reduction in the area under the SAXS curve, consistent with the change from a system of particles to a strongly layered structure that shows no density variation in the scattering direction, with the transition occurring between d = 14Å and d = 22Å.

It should be emphasized that this is a very simple model. A more detailed study would include more controlled data collection intended for this type of analysis, using an absorption standard and some method of measuring the intensity of the incident beam accurately for the results at 700eV. A more sophisticated model applicable to the discontinuous multilayers would include a dispersion of particle sizes and a form factor for disk-shaped, rather than spherical, particles.

7.2.6 Conclusions

SAXS results taken on the same specimens at very different wavelengths are consistent with a model of discontinuous multilayers. The SAXS signal reveals significant intensity from in-plane correlations, which can be observed independently at two very different wavelengths. The onset of this intensity is between multilayer d-spacings of 14Å and 22Å, in agreement with the loss of continuity observed by HRTEM and with the onset of rapid loss of multilayer reflectivity. By a model based on conservation of W, which is the predominant scatterer at both wavelengths, the intensity can be interpreted quantitatively by a simple model of spherical particles of a denser phase in a lighter matrix. For the 6Å multilayers the W-rich phase consists of particles averaging about 25Å across, and for the 14Å multilayers they average about 32Å across. The particles have densities of about $15 g/cm^3$ in both cases, consistent with some intermixing of W with B and C, but more dense than the average density of the W-rich layers found from other measurements. The longer-period multilayers show little or no discontinuity in-plane, consistent with continuous layers at d = 30Å and nearly continuous layers at d = 22Å.

The results are consistent with a thin-film growth theory in the "layer growth" model, with layers becoming continuous while still only a few atoms thick. The island sizes in the discontinuous films correspond to a contribution to roughness at spatial frequencies of $300\text{-}400 \mu m^{-1}$. This matches well with the frequencies where extra power is observed in the roughness power spectrum, as measured in a single power-law approximation in Chapter 6 and in fits to rocking curves in the second section of this chapter. SAXS technique is demonstrated to give useful results for multilayers of very short periods where in-plane inhomogeneities are an important characteristic, and to give quantitative information on average particle size and density.

7.3 Rocking Scans

7.3.1 Introduction

The rocking scan is often used in x-ray analysis to study the orientation dependence of the periodic structures in a sample, for example to test the degree of texture in a crystalline metal film. The detector is kept fixed at $2\theta = 2\theta_{Bragg}$ on a reflection from the metal lattice, and the sample is rocked about the symmetric condition. The effect is to tilt a constant scattering vector $|\mathbf{q}| = 4\pi\sin(\theta_{Bragg})/\lambda$ through the sample, and the signal gives a measure of how strongly periodic the structure is in the directions scanned. The scattering vector is perpendicular to the surface (defining the z-direction) at the symmetric condition, and takes on an in-plane (x-direction) component as the sample is rocked. Fig. 5 shows a schematic of the path taken by a rocking curve in q_x-q_z space. The rocking scan is limited in angular range to $\theta = \pm\,\theta_{Bragg}$ from the symmetric condition, because beyond this the sample blocks the incident or the scattered beam. Fig. 5 shows the increasing available tilt range as higher detector angles (2θ) are used.

The application to x-ray multilayers is the same, except the structure is expected to be very strongly textured since it is grown as flat layers on the substrate. The substrate and the layers are not perfectly flat, however, and the longer wavelength roughness features in the substrate tend to be copied by conformal growth of the layers above them. The long-wavelength or low-frequency roughness is said to be correlated and results from the substrate roughness. In the case of significant roughness at spatial wavelengths comparable to the beam size (about 1mm for these measurements) this very low-frequency roughness gives a width to the specular peak which may exceed the natural width from angular divergence of the incident beam and the finite number of layers. Fig. 6 shows a sample rocking curve from a multilayer of d = 12.3Å. This curve was measured at $2\theta = 2\theta_{Bragg}$ for the first multilayer peak. The intense specular feature in the center represents the symmetric reflection condition, and the shoulders of diffuse scattering at other angles are at much lower intensity. A measurement of the full beam (solid line) has been superimposed for comparison of the beam width. At an incident angle of about 0.5°, and at the same angle for the scattered beam on the other side, the intensity is cut off as the beam reaches the critical angle and

penetration into the sample is reduced, allowing less diffuse scattering from the buried interfaces. The specular reflectivity for this sample is shown in Chapter 6, Fig. 5.

Mid-frequency roughness is often partially correlated, meaning that roughness features from one layer are copied to the next but may be damped or amplified over several periods. These features contribute to scattering at angles a few degrees from the specular condition, and dominate what is measured in the diffuse scattering in a rocking curve. The roughness in these frequencies has contributions from the intrinsic roughness of the layers and from the substrate.

Shorter-wavelength features (features whose wavelength is comparable to the d-spacing or less) tend not to be copied from layer to layer, because their size is similar to that of local effects in the film growth such as smoothing from surface diffusion of the arriving atoms. Roughness in this wavelength regime is uncorrelated and random and cannot contribute to constructive interference over many multilayer periods. It does produce diffuse scattering, however, at angles dependent on the spatial wavelength as described earlier. This roughness contributes to the diffuse background farther from the specular peak. Its contribution may not be measurable in a rocking scan because of the limited tilt range.

For the multilayers in this study the rocking curve provides a chance to study the roughness for a short range of the middle spatial frequencies. A simple model of the diffuse scattering from the multilayers will be used to extract information on the frequency distribution of the roughness, which will then be compared with previous results.

7.3.2 Experiment and Data Reduction

Rocking scans at the first Bragg peak were measured for multilayers from d = 6.3Å to d = 31.9Å on the rotating-anode CuK_α source described earlier. The diffractometer settings and alignment procedures were the same as for the specular reflectivity described in Chapter 2. The multilayer specimens on Si(111) wafers were used, with count times of 60-80s at each point since the diffuse signal is weak. Between scans the intensity of the incident beam I_0 was measured to normalize the scans to absolute intensity. For the analysis the absolute intensity was divided by the solid angle subtended by the detector of $W = r^2\Delta a/4\pi = 4.7 \times 10^{-5}$ steradians.

7.3.3 Results

Fig. 7 shows the normalized rocking scans for 8 multilayer periods as labeled. Each curve is at the first Bragg peak, and the trend of decreasing angle reflects the lower Bragg angles as the d-spacing increases. The scans are plotted versus angle on the same range for comparison.

7.3.4 Discussion

The rocking scans show a clear trend of decreasing height of the specular peak with lower d-spacing, as the Bragg peak moves to higher angles. This parallels the loss of reflectivity over the same range, since the rocking scans are taken at the n = 1 Bragg peaks. In the transverse direction the rocking scan measures the width of the specular "ridge", which is determined by the convolution of the angular spread of the beam and the degree of correlation of the roughness. For angles close to the specular peak the rocking curve corresponds to spatial wavelengths much longer than the multilayer period, where complete correlation of roughness features from one layer to the next is expected. No change of the width of the specular ridge is found, consistent with a very low roughness at the lowest spatial frequencies (below $10^{-2}\mu m^{-1}$) as expected for very smooth polished substrates. Beyond the critical angle (about 0.4° for the average composition of the multilayers) there is a sharp drop in the signal as the sample begins to occlude the incident or the scattered beam. For a fuller analysis a simulation will be required as will be described below.

7.3.5 Analysis

The topic of diffuse scattering from rough surfaces is a rich one, and includes many different models and types of measurements from radar to the hard x-ray. A book containing a review and many references has recently been published by Bennett and Mattsson.[3]

For the case of multilayers the problem is complicated considerably by the issue of coherence of the scattered rays. For uncorrelated roughness the scattered radiation adds with random phase, while for correlated roughness coherent addition is possible at conditions away from specular, giving "quasi-Bragg" features which have been observed experimentally.[4,5] In reality the roughness is normally partially correlated as described above – correlated at longer wavelengths and uncorrelated at shorter ones. General treatments have been published by Sinha[6] and Stearns[7,8], but they require a model including cross-correlations of roughness for all the interfaces over all frequencies, which are very difficult to measure accurately. Another complication is the multiple reflections when the reflectivity is strong, which are accounted for in the specular reflectivity by the dynamical treatment described in Chapter 3. A full dynamical treatment, including correlation and extinction effects has been published by Stearns[9] aimed at predicting the effects of diffuse scattering on image quality in multiple-bounce soft x-ray lithography systems operating near $\lambda = 130$Å.

For the multilayers in this study a kinematical model based on that of Gullikson[10] and Sinha[6] has been used. This formalism works in the Born approximation for scattering from a surface, which assumes that the scattered wave is weak compared to the incident wave. This model will be presented below, beginning with scattering from a single surface.

The central assumption of the theory by Sinha is that the surface is Gaussian, or that the surface is represented by a single-valued function z(x, y) for which $\langle z(x', y') - z(x, y)\rangle$ is a Gaussian random variable (where the averaging is over all pairs of points (x, y) and (x', y')). We write the mean square variation of the surface as a function $g(X, Y) = \langle [z(x', y') - z(x, y)]^2\rangle$ where the relative coordinates (X,Y) represent the distances between two points: $(X,Y) \equiv (x'-x, y'-y)$. The function g then represents the average spatial relationship of two points on the surface. Many rough surfaces in nature, both microscopic and macroscopic, show behavior of

$$g(X,Y) = g(R) = AR^{2h} \tag{12}$$

where $R^2 = X^2 + Y^2$. This is an increasing function because for R = 0, the two points are identical and have no separation, so g(0) = 0, and the greater the separation of the points in x and y, the greater the likelihood

they will be widely separated in z. The exponent h is related to how jagged the surface is, a larger value representing a surface with smoother, longer-wavelength undulations. This representation of roughness corresponds to self-affine surfaces, as studied in detail by Mandelbrot[11] and Voss[12,13], and can describe many rough surfaces in nature. In this model, the function g(R) diverges as $R \rightarrow \infty$, though real polished surfaces such as silicon wafers are macroscopically flat and for them g(R) must reach a finite value at large R. In this case the mean-square roughness saturates at a value σ^2 and the PSD has a finite integrated area, and g(R) can be written

$$g(R) = 2\sigma \left[1 - e^{-(R/\xi)^{2h}}\right] \tag{13}$$

where ξ is a cutoff length for the roughness of the substrate. This function behaves like the general case when $R << \xi$.

For any scattering from a Gaussian surface, the scattering cross-section is given by

$$\frac{d\sigma}{d\Omega} = n^2 r_e^2 |f|^2 A S(\mathbf{q}) \tag{14}$$

where n is the number density of atoms of atomic scattering factor f, r_e is the classical electron radius e^2/mc^2, A is the illuminated area on the surface, and $S(\mathbf{q})$ is the scattering function:

$$S(\mathbf{q}) = \frac{1}{q_z^2} \int\int_S (e^{q_z^2 g(X,Y)/2} - 1) e^{-i(q_x X + q_y Y)} dX dY. \tag{15}$$

$S(\mathbf{q})$ represents all scattering from the surface. If the surface is macroscopically flat as defined above (i.e. is flat on the size scale of the width of the incident beam) the specular and diffuse scattering can be separated and the diffuse scattering is given by:

$$S_{diff}(\mathbf{q}) = \frac{e^{-q_z^2 \sigma^2}}{q_z^2} \int\int_S (e^{q_z^2 C(X,Y)} - 1) e^{-i(q_x X + q_y Y)} dX dY \tag{16}$$

where C(X,Y) = C(R) is the height-height correlation function for a rough surface with a low-frequency cutoff:

$$C(R) = \sigma^2 e^{-(R/\xi)^{2h}} \tag{17}$$

The cross-section is related to the measured intensity by

$$\frac{1}{I_0}\frac{dI}{d\Omega} = \frac{(I/I_0)}{\Delta\Omega} = \frac{1}{A_0}\frac{d\sigma}{d\Omega} \tag{18}$$

where A_0 is the area of the incident beam, and the scattered intensity is then given by

$$\frac{1}{I_0}\frac{dI}{d\Omega} = \frac{q_z^{\ 4}}{16\pi^2 \sin\theta} R(q_z) S(\mathbf{q}) \tag{19}$$

Here $R(q_z) = |1-\varepsilon|^2 (k/q_z)^4$ is the Fresnel reflectivity of the surface for angles above the critical angle. The Born approximation is not appropriate for angles below the critical angle, where the Fresnel reflectivity is large, and the scattering can no longer be considered weak. A diffuse-scattering model based on the distorted-wave Born approximation, accurate near the critical angle, is also presented by Sinha[6] though its application to multilayers is difficult as mentioned earlier.

Diffuse scattering from a multilayer can be treated in this formalism by summing the Fresnel reflectivities and scattering functions over the pairs of interfaces. This is a kinematic treatment with no multiple scattering events included. The scattered intensity is then given by

$$\frac{d(I/I_0)}{d\Omega} = \frac{q_z^{\ 4}}{16\pi^2 \sin\theta} \sum_{i,j} \Delta\varepsilon_i \Delta\varepsilon_j^* e^{-iq_z(z_i - z_j)} S_{ij}(\mathbf{q}) \tag{20}$$

where $\Delta\varepsilon_i$ is the difference of the dielectric function at the ith interface and $S_{ij}(q)$ is the scattering function for the pairs of interfaces i,j:

$$S_{ij}(\mathbf{q}) = \frac{e^{-q_z^2(\sigma_i^2+\sigma_j^2)/2}}{q_z^2} \iint_S (e^{q_z^2 C_{ij}(x,y)} - 1) e^{-i(q_x x + q_y y)} dxdy \tag{21}$$

Here the $C_{ij}(x,y)$ are the cross-correlations for pairs of interfaces i,j which depend on distance – the roughness is expected to be fully correlated from layer to layer at distances much greater than the multilayer period, and uncorrelated at short distances comparable to the period or comparable to diffusion distances of of adatoms and particles on the growing film. If the roughness is completely correlated (for the spatial frequencies contributing to the measurement) then $C_{ij}(x,y) = C(R)$ for all i,j, and the scattered intensity is

$$\frac{d(I/I_0)}{d\Omega} = \frac{q_z^{\ 4}}{16\pi^2 \sin\theta} R(q_z) S(\mathbf{q}), \text{ where } R(q_z) = \left| \frac{k^2}{q_z^2} \sum_i \Delta\varepsilon_i e^{-iq_z z_i} \right|^2 \tag{22}$$

Here $\Delta\varepsilon_i$ is the change of the dielectric function at the ith interface, at height z_i above the substrate, and k is the wave vector $2\pi/\lambda$ of the incident beam. This is the same expression as for a single surface, except that the reflectivity is calculated for a multilayer using the kinematic approximation. This is not treating the multilayer as a single surface, however, since the multilayer reflectivity includes constructive interference whenever **q** meets the Bragg condition $|\mathbf{q}_x| = 2\pi/d$. This model will thus include the "Bragg ridge", or resonant diffuse scattering where $|\mathbf{q}_x| = 2\pi/d$ away from the specular condition. This formalism was used to fit the rocking curves for the parameters of the correlation function h, σ and ξ. The error between the calculated and experimental rocking curves was calculated using the same error metric as for the reflectivity fits in Chapter 6, and errors compiled for a matrix of the three parameters, covering the physically possible values of σ and ξ and the range of h consistent with the model, $0 < h < 1$. The parameters giving the minimum error were then included in a more finely-spaced matrix, and the calculation repeated. Multiple minima in the error were not found for any curve, consistent with the monotonic dependence of $C(\tau)$ on the parameters, though a detailed inspection of the error contours was not made.

The assumption of perfect correlation is a reasonable one for most of the multilayers in this study, for the spatial frequencies contributing to scattering in the rocking curves. For d = 31.9Å the rocking curve

extends to $q_x \cong 0.002Å^{-1}$ or $\Lambda = 2\pi/q_x = 3100Å$, and for d = 6.3Å it extends to $q_x \cong 0.04Å^{-1}$ or $\Lambda = 160Å$. Even at the shortest d-spacing the longest spatial wavelengths are more than 20 times the multilayer period and should be unaffected by uncorrelated roughness from local microstructure effects, such as random variation in the film thickness. However, the correlation is also affected by diffusion distances of particles in the growing film, which may operate over longer distances. The limits of the validity of this assumption will be revisited later.

7.3.6 Fits

The rocking curves are shown with the fits in Fig. 8. The angles have been converted to q_x to compare the curves on one graph and the intensities are vertically offset with multiplicative factors to separate the curves. The model calculates the diffuse scatter only, so the fits contain no specular feature at $q_x = 0$. The curve for the lowest d-spacing, 6.3Å, could not be acceptably fit with this model, possibly because the assumption of perfect correlation may no longer hold. For the rest of the curves the model fits quite well, except in some cases near the critical angle where the reflectivity is large and the kinematic treatment is not adequate. The assumption of perfect correlation is approximate – the roughness at mid spatial frequencies (roughly 10^{-2}-$10^{2}\mu m^{-1}$) is expected to be highly correlated but to contain substantial contributions from roughness intrinsic to the layers.[9,10] The inability of the model to fit the reflectivity at d = 6.3Å, where the ends of the rocking curve correspond to spatial wavelengths of 160Å, is consistent with a breakdown of this assumption. The model also slightly overpredicts the diffuse scattering at the ends of the d = 10.2Å rocking curve, which is consistent with the model assuming a stronger correlation than exists in the sample. Windt's measurements[14] of substrates before and after coating indicated that strong correlation of top-surface roughness to substrate roughness exists for spatial wavelengths as short as 50Å, while studies of diffuse scattering by Gullikson[10] indicate that correlation breaks down closer to L = 1000Å. The degree of correlation depends to some degree on the sputtering conditions, since the mobility of particles arriving on the growing surface (which is strongly affected by sputtering pressure) determines the distance the particles can travel to fnd a minimum-energy position. A value above 160Å but below about 300Å (where the model fits the end of the d = 14.1Å rocking curve well) is reasonable.

The values of the fit parameters are given in Table 1. The error is calculated by the same error metric used for the specular reflectivity, omitting the end regions beyond the critical angle where the model is expected by be inaccurate. The error is normalized by dividing by the number of points in the region fitted, to account for the different lengths of the rocking scans.

The general increase of the correlation length with d indicates roughness dominated by longer spatial wavelengths, consistent with the films becoming continuous and the roughness from the island structure decreasing. For the continuous films, the roughness is expected to be dominated by the substrate roughness and roughness intrinsic to the films from other sources, such as fluctuations from the statistical nature of the film growth. Measurements of correlation lengths from rocking curve fits on a polished glass surface[6] on a Si wafer gave $\xi = 7000$Å, while measurements from fits for a single thick AlSi film on a Si wafer[15] gave $\xi = 4000$Å. Since the multilayers in this specimen would be expected to include a greater contribution from shorter-wavelength roughness intrinsic to the layers[9], a value of 1100Å for the continuous multilayers is a reasonable one. With decreasing d-spacing, the correlation length should include more high-frequency contributions, especially as the films become discontinuous with islands about 20Å across.

The values of σ represent in this case the rms roughness over the entire range of frequencies, from the low-frequency cutuff (due to the macroscopic flatness of the substrate and multilayer) to the high frequencies where the power is low and makes a vanishing contribution to the overall roughness. Sigma appears as a coefficient in the power-law correlation function which scales the entire correlation function, the frequency dependence being contained in the R/ξ term. While this range of contributing frequencies remains constant, the increase in σ is due to the increasing spectral weight at the lower frequencies with the higher d-spacing, as shown in the calculated PSDs corresponding to these values. While the rms roughness is increasing, the roughness measured by any experiment might show a different trend, since the slope of the PSD is also changing with d. This illustrates the point, also brought up by Church[16] and Windt, that a property of interest, such as reflectivity, may not correlate with a measurement of the rms roughness or of the roughness over a limited range of frequencies, but consideration of the surface's PSD is essential. The roughness exponent, h, shows no clear trend in the fits. It is in theory related to the texture of the rough

surface, low values of h giving jagged surfaces, and high values giving smoother features. Distinguishing different combinations of h and ξ had the greatest uncertainty in the fits, as some range of each parameter can give similar correlation functions. The resulting PSD, however, is not strongly influenced by this choice.

To relate these fits to other data, the correlation functions defined by the fit values of h, σ, and ξ were converted to a section of the PSD for each sample, using a Fourier cosine transform (since $C(\tau)$ is an even function for an isotropic surface). The range of the distances τ was chosen to cover the spatial wavelengths relevant to the rocking curves. Because of the limited frequency range available in the rocking curves (especially for the higher d-spacings), the calculated PSDs have flat tails at the higher frequencies which are not meaningful and have been trimmed. Fig. 10 shows the calculated PSDs, plotted with the experimental PSDs from the literature (measured by scanning-probe techniques) that were presented in Chapter 6, Fig. 11.

The calculated PSDs are comparable to those measured by the surface probe techniques, though they are higher by about an order of magnitude than those measured on similar substrates by Windt and Tobben. The scanning probe techniques, however, measure only the top surface of the multilayer. The Mo/Si multilayers measured by Windt, for example, had an Si layer as the top surface, while it is known[17] that amorphous layers in a crystalline/amorphous multilayer system such as Mo/Si are typically smoother than the metal layers and reduce the overall roughness of the stack. Any roughness originating from discontinuity within the layers would likely not be measured by a scan of the top surface. The diffuse scattering, on the other hand, is sensitive to both roughness of the layer surfaces and discontinuity with the

d (Å)	error ($\times 10^{-5}$)	h	σ (Å)	ξ (Å)
10.2	0.68	0.69	1.7	190
12.3	5.93	0.52	2.1	180
14.1	6.56	0.70	2.2	230
17.4	14.2	0.58	2.5	270
20.6	25.1	0.65	2.5	340
25.0	22.2	0.99	2.5	660
31.9	62.6	0.79	3.3	1200

Table 1. Values of roughness exponent h, rms roughness σ, and correlation length ξ from fits of multilayer rocking curves, 10.2Å < d < 31.9Å.

layers, and would be expected to give a higher roughness.

The slopes of the calculated PSDs are also of interest. They are available only over a limited range of spatial frequencies accessible in the rocking curve, and this range is narrower for the rocking curves at higher d-spacings because of the smaller Bragg angle of the first peak. The slopes are nearly the same for all d-spacings up to 20.6Å, then the higher d-spacings have more negative slopes. While the trend is not monotonic, the slopes for the lower d-spacing multilayers are comparable to that calculated from the specular reflectivity for the discontinuous multilayers, and those for d = 25.0Å and d = 31.9Å are comparable to that found for the continuous multilayers. This is consistent with the discontinuous multilayers gaining extra spectral weight at the higher frequencies, due to the extra roughness from the island structure.

7.3.7 Conclusions from Rocking Scan Analysis

Data from accurate rocking scans of W/B_4C multilayers of period 10.1Å < d < 31.9Å can be fit using a kinematical diffuse-scattering model and using a simple power-law spectral density to characterize layer roughness, assumed to be perfectly correlated from one interface to the next. The fits give PSDs comparable to those measured on similar samples by scanning probe techniques, though somewhat higher, which is consistent with the x-ray measurement being sensitive to roughness internal to the layers resulting from a loss of continuity, which may not be measured by the scanning probe on the top surface. The PSDs show a less negative slope with smaller d-spacing, consistent with thinner layers becoming discontinuous and acquiring extra roughness at higher frequencies. The change of slope is most distinct between d = 20.6Å and d = 25.0Å, somewhat higher than the apparent transition from discontinuous to continuous multilayers between 15Å and 20Å indicated by the evidence from TEM and analysis of specular reflectivity. This may be attributable to the range of frequency sensitivity of the rocking curves, which does not quite include the size scale of the islands seen in the thinnest multilayers but would be sensitive to somewhat longer length scales of a nearly-continuous film consisting of larger islands.

The results are consistent with discontinuity in the shorter d-spacing contributing to increased diffuse scattering at angles within a few degrees of the specular, in agreement with analysis of the specular

reflectivity and the information on microstructure from the TEM. The rms roughness decreases by approximately 50% from d = 31.9Å to d = 10.2Å, though the roughness as a fraction of d is increasing. The change in roughness is associated with a change in slope of the PSD, so the effect of the different roughness on any x-ray optic application may not be related to the change in rms roughness. Despite the simplicity of the measurement and the model, such an analysis of rocking curves can give useful information on internal roughness of buried interfaces in the multilayer that it otherwise difficult to measure.

7.4 General Conclusions on Diffuse Scattering Results

Diffuse scattering studies performed in transmission in the small-angle x-ray scattering (SAXS) geometry, and in reflection in rocking curves, permit quantitative analysis of contributions of in-plane roughness and inhomogeneities in multilayers to the multilayer power spectrum. The SAXS results give direct evidence of the onset of discontinuity at d-spacings between 14Å and 22Å, in good agreement with results from HRTEM microstructure studies and specular reflectivity. The SAXS results are consistent with the discontinuous multilayers containing islands of 25-30Å size, in excellent agreement with sizes observed in TEM. The averaging over the entire specimen in the SAXS results permits a more global and quantitative result than is available by TEM, and provides complementary information to the high-resolution inspection of the microstructure. The sizes of the islands indicate they would make a strong contribution to the roughness power spectrum at frequencies near 300-400μm^{-1}, consistent with indications of higher spectral weight near these frequencies from simulation of specular reflectivity. Simulation of rocking curves with a physically reasonable model of highly-correlated roughness indicates a change in the slope of the multilayer power spectrum, also consistent with increasing contributions at high frequencies as the layers become rougher, in the d-spacing range 20Å to 25Å. Diffuse scattering techniques permit measurement of microstructural changes contributing to the PSD in ranges of spatial frequency not easily accessible to other techniques, and including contributions from buried interfaces not detectable in surface scans.

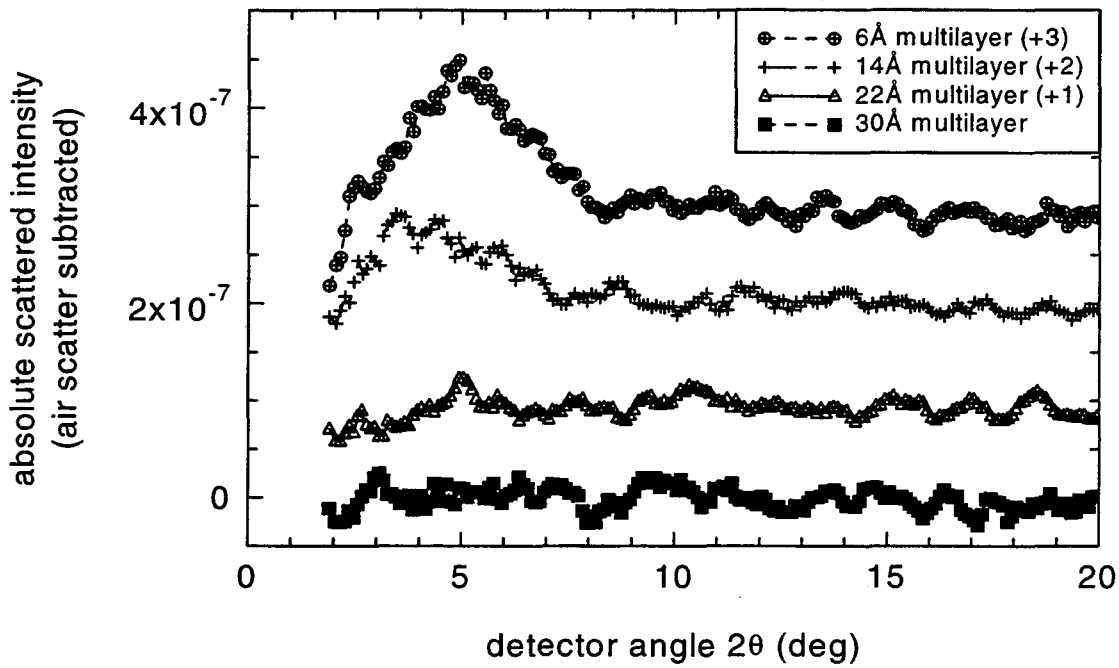

Fig. 1. Small-angle x-ray scattering (SAXS) signal at l =1.54Å (CuK_α) from four W/B_4C multilayers. Background has been subtracted and scans are smoothed by averaging over a window of 5 points (±0.2°) to better show the significant features.

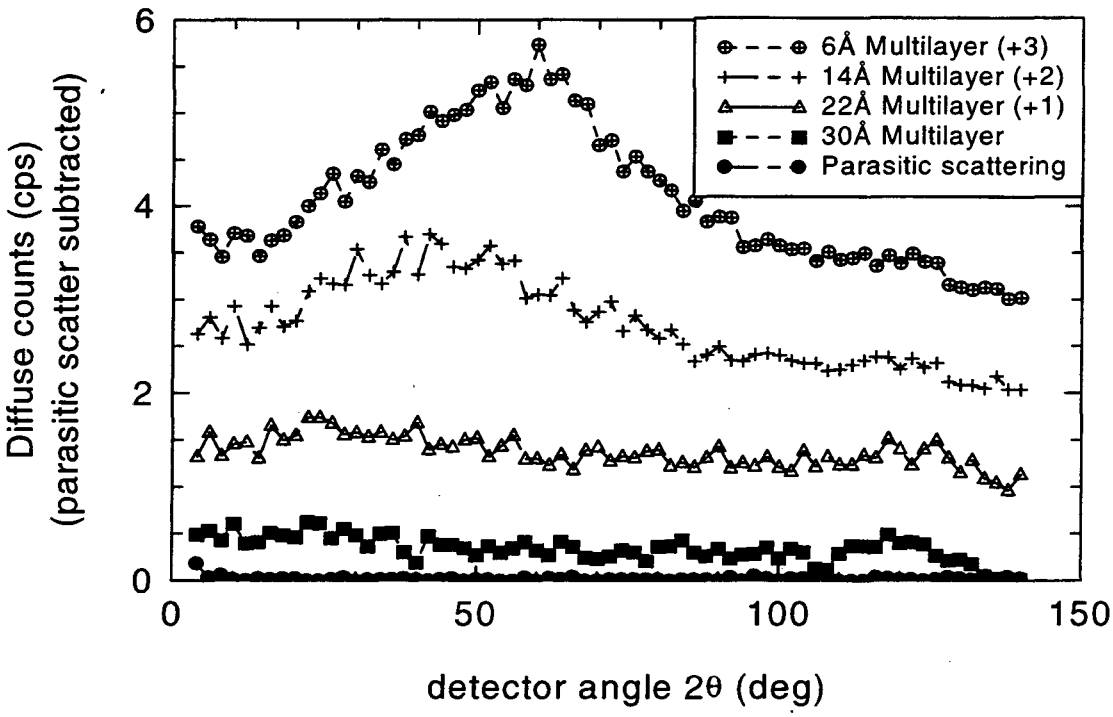

Fig. 2. SAXS signal at l = 17.7Å (700eV) from W/B_4C multilayers. Background (parasitic) signal has been subtracted; no smoothing has been performed.

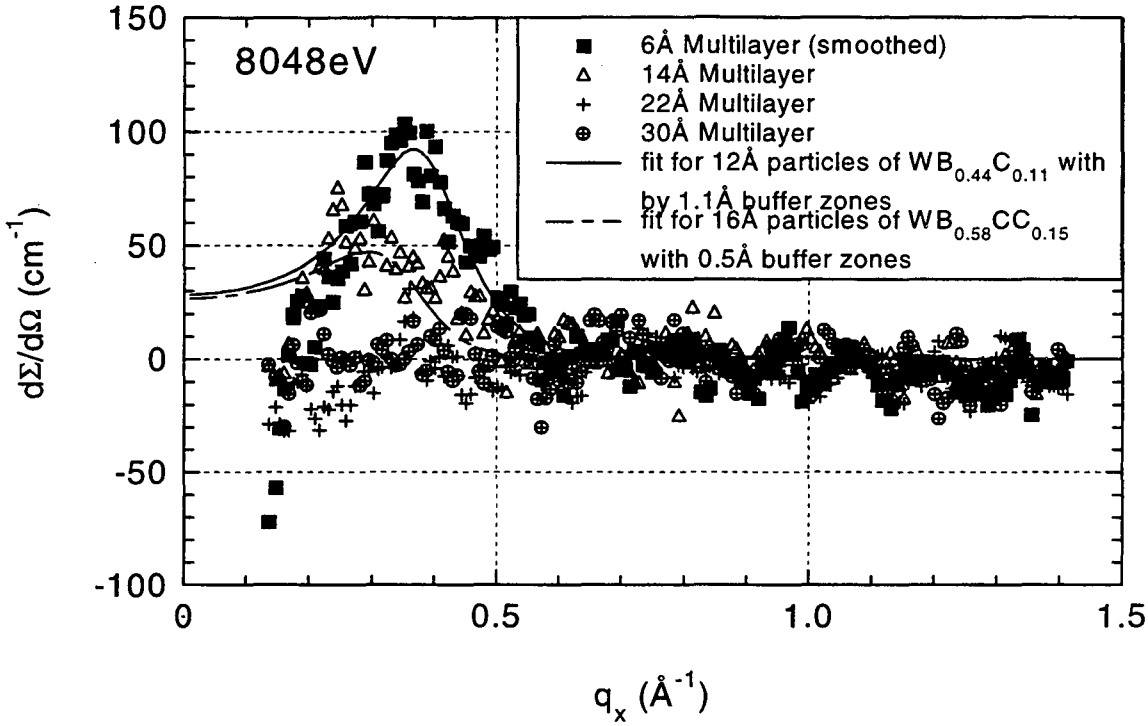

Fig. 3. Fits to SAXS results at $\lambda = 1.54Å$ (CuK_α) for d = 6Å and d = 14Å W/B_4C multilayers. Particle sizes are radii (R). The 14Å fit has been multiplied by 2.65 to improve the fit – see text. The particle composition corresponds to a density of 15.9 g/cm^3 or an expansion of the W-rich phase by 25%.

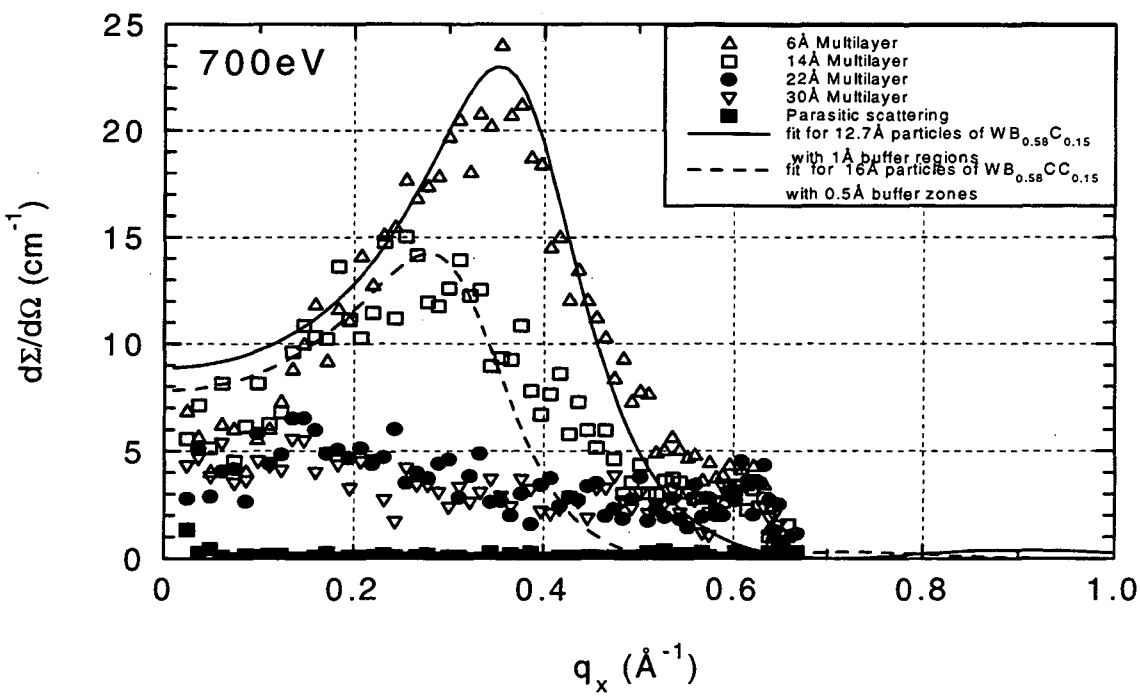

Fig. 4. Fits to SAXS results at $\lambda = 17.7Å$ (E = 7003V) for d = 6Å and d = 14Å multilayers. Particle sizes are radii (R). The 14Å fit has been multiplied by 2.65 like the previous figure. The particle composition corresponds to a density of 15.0 g/cm^3 or an expansion of the W-rich phase by 35%.

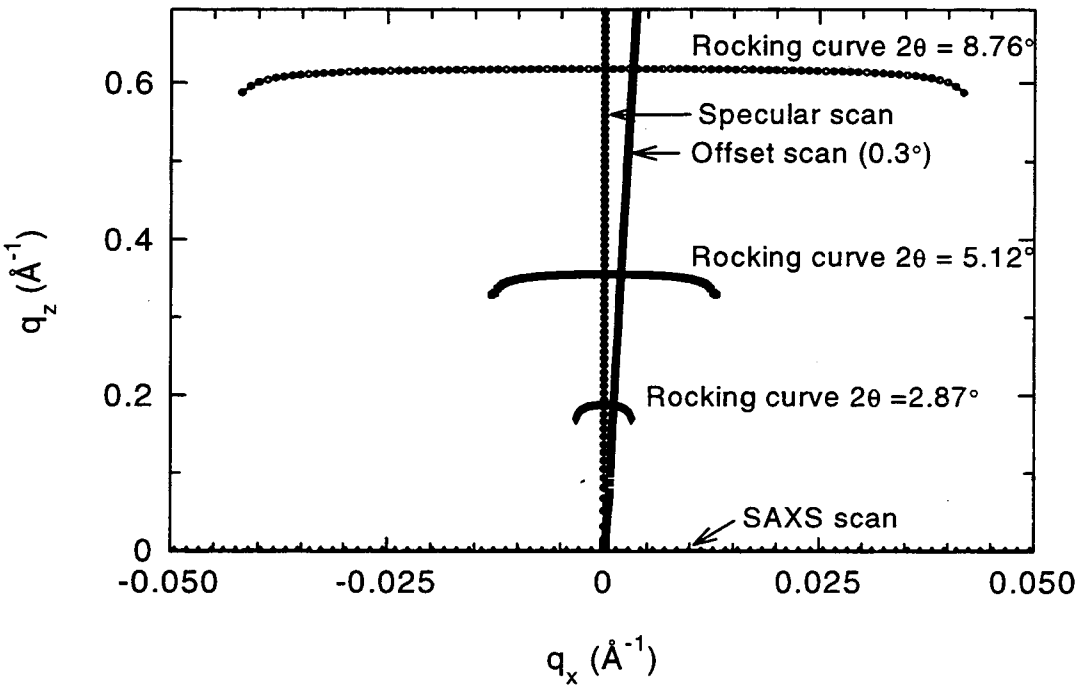

Fig. 5. Path of rocking scans and other scans in reciprocal space, plotted as the component normal to the sample surface (q_z) versus the component in the plane of the sample (q_x). The range of rocking scans is limited by the intrusion of the sample into the incident or scattered beam. The q_x scale is expanded – the frequency range accessible to the SAXS scan extends to much greater q_x.

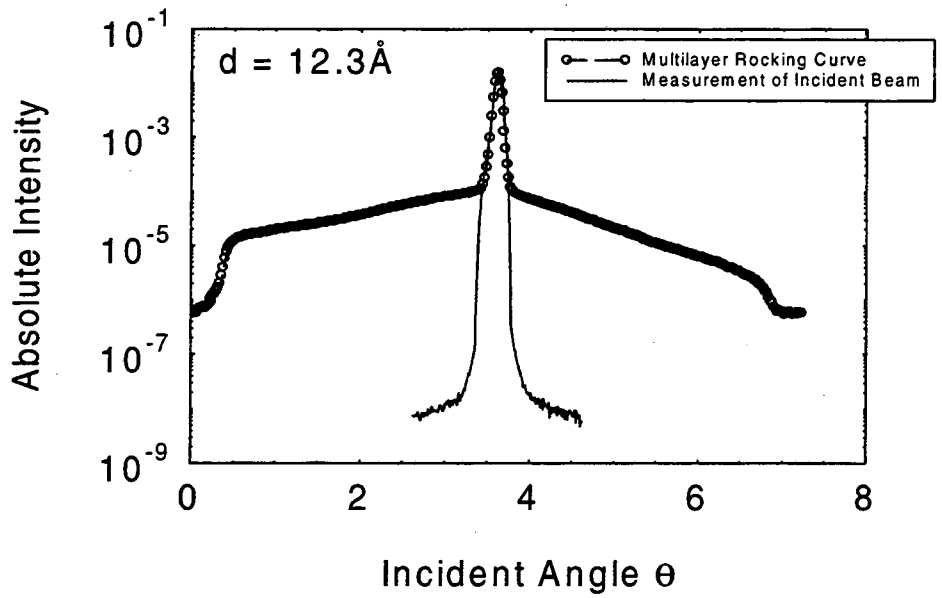

Fig. 6. Example rocking scan of d = 12.3Å multilayer (circles). Also shown is measurement of the incident beam, superimposed on the specular peak of the rocking curve for comparison. There is no measurable broadening of the specular peak by the multilayer, consistent with a low level of roughness at the lowest frequencies.

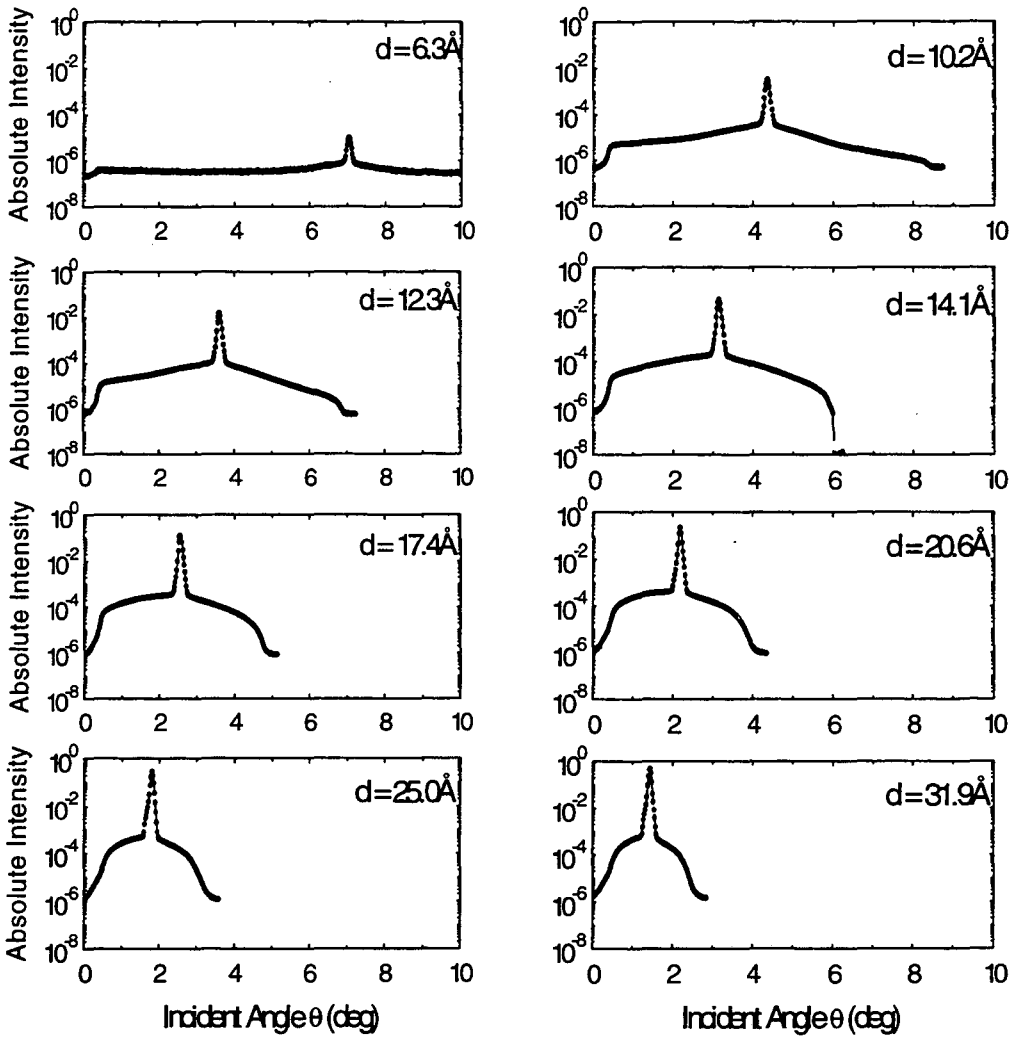

Fig. 7. Rocking scans for W/B_4C multilayers 6.3Å < d < 31.9Å, at first Bragg peaks, l = 1.54Å.

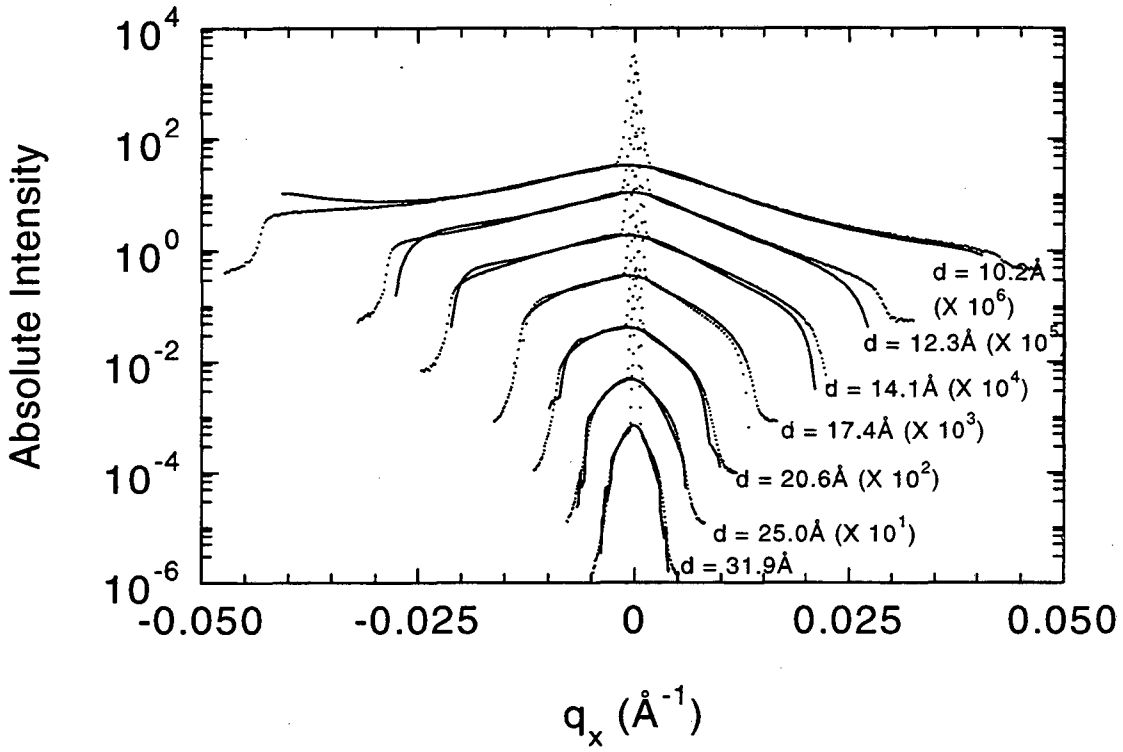

Fig. 8. Rocking curves (symbols) and fits (solid lines) for multilayers 10.1Å < d < 31.9Å.

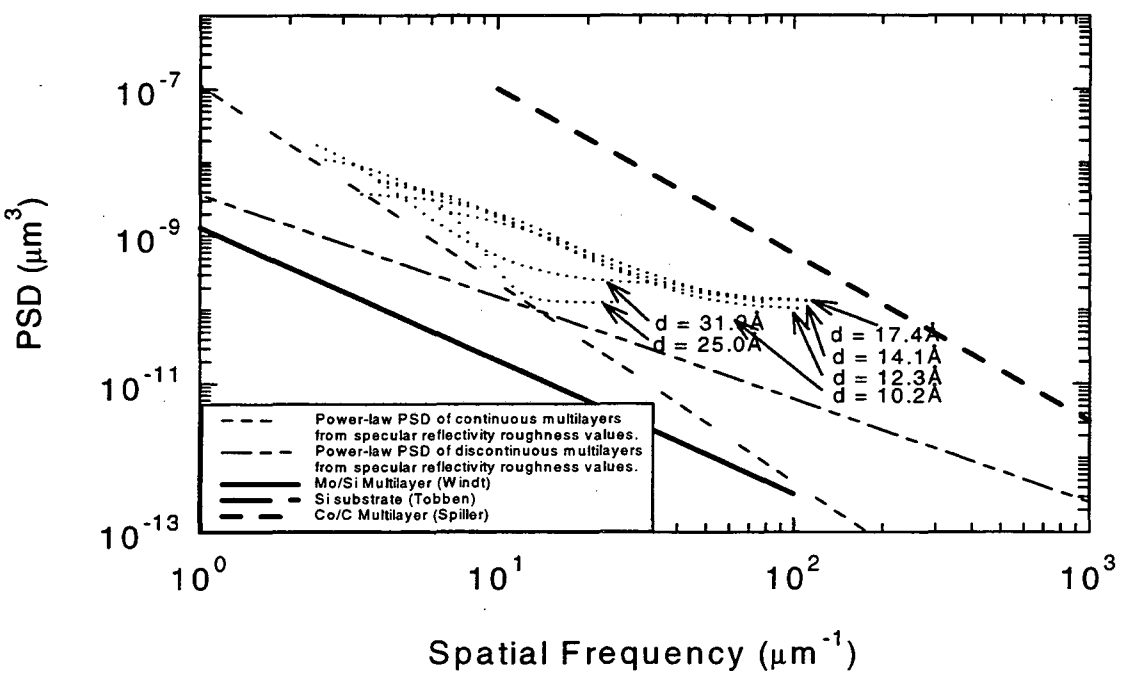

Fig. 9. PSDs calculated from rocking-curve fits, with other PSD data as shown in Chapter 6 Fig. 4.

References

[1]M. B. Rice, "Anomalous Small Angle X-Ray Scattering Studies of Amorphous Metal-Germanium Alloys," Ph.D., Stanford University, 1993.

[2]B. L. Henke, E. M. Gullikson, and J. C. Davis, "X-ray interactions: photoabsorption, scattering, transmission, and reflection at E=50-30000 eV, Z=1-92," Atomic Data and Nuclear Data Tables **54** (2), 181-342 (1993).

[3]Jean M. Bennett and Lars Mattsson, *Introduction to surface roughness and scattering* (Optical Society of America, Washington, D.C., 1989).

[4]J. B. Kortright, "Nonspecular X-ray scattering from multilayer structures," Journal of Applied Physics **70** (7), 3620-5 (1991).

[5]D. E. Savage, J. Kleiner, N. Schimke *et al.*, "Determination of roughness correlations in multilayer films for X-ray mirrors," Journal of Applied Physics **69** (3), 1411-24 (1991).

[6]S. K. Sinha, E. B. Sirota, and S. Garoff, "X-ray and neutron scattering from rough surfaces," Physical Review B (Condensed Matter) **38** (4), 2297-311 (1988).

[7]D. G. Stearns, "The scattering of X-rays from nonideal multilayer structures," Journal of Applied Physics **65** (2), 491-506 (1989).

[8]D. G. Stearns, "X-ray scattering from interfacial roughness in multilayer structures," Journal of Applied Physics **71** (9), 4286-98 (1992).

[9]D. G. Stearns, D. P. Gaines, D. W. Sweeney *et al.*, "Nonspecular X-ray Scattering in a Multilayer-Coated Imaging System (to be published)," .

[10]E.M. Gullikson, D.G. Stearns, D.P. Gaines *et al.*, "Non-specular scattering from multilayer mirrors at normal incidence," presented at the Grazing Incidence and Multilayer X-Ray Optical Systems, San Diego, CA, 1997 (unpublished).

[11]Benoit B. Mandelbrot, *The fractal geometry of nature* (W.H. Freeman, San Francisco, 1982).

[12]R. F. Voss, "Scaling Phenomena in Disordered Systems," , edited by R. Pynn and A. Skjeltorp (Plenum Press, New York, 1985), pp. xii, 580.

[13]R. F. Voss, "Fundamental algorithms for computer graphics," , edited by Rae A. Earnshaw (Springer-Verlag, Berlin
New York, 1985), pp. xvi, 1042.

[14]D. L. Windt, W. K. Waskiewicz, and J. E. Griffith, "Surface finish requirements for soft X-ray mirrors," Applied Optics **33** (10), 2025-31 (1994).

[15]W. Weber and B. Lengeler, "Diffuse scattering of hard X rays from rough surfaces," Physical Review B (Condensed Matter) **46** (12), 7953-6 (1992).

[16]E. L. Church and P. Z. Takacs, "Specification of glancing- and normal-incidence X-ray mirrors," Optical Engineering **34** (2), 353-60 (1995).

[17]E. Spiller, "Enhancement of the reflectivity of multilayer X-ray mirrors by ion polishing," Optical Engineering **29** (6), 609-13 (1990).

Chapter Eight

Synthesis

8.1 Conclusions

A systematic study of the reflectivity of W/B4C multilayers shows that this system can form multilayers for very short periods. The reflectivity is close to that of an ideal multilayer structure for periods above 25-30Å, though some intermixing of the W and B_4C reduces the density of the W-rich layers. Absolute eflectivity begins to drop sharply at d = 15-20Å, and at the same thicknesses the reflectivity begins to fall sharply below the calculated values for ideal structures. Despite this drop, the multilayers retain a measurable composition modulation for periods as short as 4.7Å, corresponding to individual films 2-2.5Å thick, or approximately monolayers of W and B. A stack of layers is not an accurate description of the structure at these periods, however.

The two principal mechanisms limiting reflectivity of x-ray multilayers are interdiffusion and roughness (including contributions from layer discontinuity). Both are present in this system and limit reflectivity in different ways. Substantial interdiffusion is present even at periods near 50Å and affects reflectivity, as is evident from observed layer thicknesses in HRTEM and reduced densities consistent with the observed reflectivities. But interdiffusion is not the primary cause of the reflectivity loss, because even at the smallest d-spacings discrete W-rich and B-rich regions can be directly observed by TEM. Instead, at periods of 15-20Å, the W-rich layers are no longer thick enough to become continuous. At the smallest periods they are broken up into isolated islands, and at periods of 15-20Å, at the transition from continuous layers to discontinuous ones, they have irregular thickness corresponding to roughness that is a significant fraction of the multilayer d-spacing. The roughness and discontinuity of the layers reduce the reflectivity by reducing the average abruptness of the interfaces contributing to the Bragg reflection, and produces diffuse scattering away from the specularly-reflected beam. The discontinuity is the ultimate limit on the multilayer performance.

The spatial frequency distribution of the roughness reflects its relation to the multilayer microstructure. Analysis of the reflectivity at all periods is consistent with roughness obeying a power-law power spectral density, or PSD, for low to mid spatial frequencies up to about $10^2 \mu m^{-1}$. The PSD changes in slope with d-spacing, acquiring a less negative slope with smaller d from extra spectral weight at the higher frequencies. The PSD is likely to level off or have a bump at higher spatial frequencies (10^3 - $10^2 \mu m^{-1}$) for the shortest-period multilayers with the onset of discontinuity of the films. Direct measurement of the PSD is possible for limited spatial-frequency ranges by analysis of diffuse scattering in rocking curves, which includes contributions to roughness from in-plane inhomogeneities and from all the buried layers, and more information may be available from diffuse scattering in other geometries. The changing slope of the PSD with different d-spacings indicates that analysis of the PSD provides essential insight into the expected effects of roughness in x-ray applications of multilayers. Measurements of rms roughness only are useful but must be interpreted carefully, taking into account the range of frequency sensitivity of the measurement and of the intended application.

Direct evidence of in-plane inhomogeneity from discontinuity of the layers is available from the small-angle x-ray scattering (SAXS) technique. Results from these multilayers indicate the onset of multilayer discontinuity between 14 and 22Å, with some marginal discontinuity present at 22Å, where the layers are likely nearly continuous but with fluctuations in thickness which give some in-plane scattering. At periods of 14Å and 6Å the layers are clearly discontinuous and show distributions of cluster or island sizes centered at about 30Å and 25Å. The islanded structure can also be directly observed by TEM in plan view. While cross-section TEM shows the onset of discontinuity and gives a valuable analysis of microstructure, it is unable to detect the weak composition modulation at the shortest periods, underscoring the importance of complementary x-ray techniques to full analysis of microstructure issues on the near-atomic scale.

Even at the very short d-spacings near 5Å, where the composition modulation in the vertical direction is weak, strong inhomogeneity is found in the in-plane directions. The SAXS results indicated average compositions of the islands near $WB_{0.6}$, and the contrast visible in the plan-view TEM results at d = 6Å also indicates substantial segregation. This indicates that the discontinuous or islanded layers must begin to interpenetrate, causing the observed loss of reflectivity without complete interdiffusion.

Spectroscopic studies of boron bonding show some continuous change in the average environment of the boron atoms from films of B_4C only through the thinnest multilayers. This change may result from increasing average proximity of B and W atoms with thinner layers, or may also result from some increase in interdiffusion with thinner layers. With a better set of standard samples the spectroscopy techniques hold promise for investigation of changing bonding in multilayers.

Incomplete growth of the layers is consistent with thin-film growth theory, with a high energy of the arriving particles during sputtering. A low sputtering pressure allowing bombardment of the growing film and removal of loosely-bound particles appears, from results in the literature, to contribute to the ability of W/B_4C to form such thin continuous layers. The ultimate cause of reflectivity loss is a microstructural one, suggesting that further analysis of materials choice and sputtering conditions may provide useful multilayers at even shorter periods, or improve performance in the d = 10-20Å range.

Evidence from many techniques gives a consistent model of the multilayer performance and microstructure over the range of periods. The limitations of the different techniques underscores increases the importance of using others to make correct interpretations. The TEM gives excellent local microstructural information but is not sensitive to the weak vertical composition modulation at the shortest periods. The specular reflectivity alone gives an estimate of roughness in a single parameter σ, but this could be misinterpreted without diffuse scattering and consideration of the entire range of spatial frequencies of the roughness. In this difficult problem of determining atomic-scale microstructures the need for several complementary techniques is clear.

8.2 Suggestions for Improving Reflectivity and Future Work

In order to improve reflectivity in this system, it would be necessary to make layers thinner than 8-10Å that are still continuous. This is a delicate balance in different effects of the sputtering process. The bombardment caused by low pressure knocks off loosely-bound particles and helps form dense and smooth layers, but at the same time it probably contributes to islanding, because the most loosely-bound particles are the ones that have not attached to ledges at the edges of islands but are isolated. A parametric study of the sputtering current (and necessarily with it the voltage) to change the rates and energies of this

bombardment might give some improvement here. Similarly a negative substrate bias can be used to attract Ar^+ ions from the plasma for extra bombardment. Several researchers[1,2] have investigated substrate bias and ion bombardment and it seems to give improved smoothness, but the improvement is largest at higher sputtering pressures. Since higher pressures have been shown[3-5] to produce poorer multilayers because of low surface mobility, this suggests that bias may produce the same benefit as low pressure and may offer no improvement if the pressure is already optimized.

There is also a delicate balance in materials choice, between materials with enough mutual affinity (low enough surface energy) to wet each other and form thin continuous layers, but not so much affinity (energies of reaction and mixing) that they interdiffuse easily, as did the first multilayers of Cu/Au[6]. From the large body of literature the best systems at many x-ray wavelengths seem to be heavy refractories as reflectors, separated by light spacers with which they form compounds. The reactivity lowers the surface energy, but if the reaction product is very strongly bonded it lowers the diffusivity at the same time by binding the atoms that diffuse. The refractories generally form very stable, hard and high melting-point compounds with many of the lowest-Z solids such as B and C, indicating very strong bonding. Using a compound for the spacer material appears to limit its atoms' mobility in the same way – W/B_4C forms smoother and more stable multilayers than W/C[7]. Since B_4C is already a stable and strongly-bonded compound it may prevent the B and C atoms from diffusing into the heavy layers or better resist implantation of W atoms during sputtering. For better reflectivity at ultra-short periods, other material combinations might be promising for this reason: W/SiC, WC/B_4C or WB/B_4C.

8.3 Suggested Future Work on W/B_4C

Suggestions for future analytical work on this system would include further spectroscopic studies on the extent of intermixing of W and B_4C. Some preliminary Electron Spectroscopy for Chemical Analysis (ESCA) studies showed peak shifts for W and B with different d-spacing. Proper interpretation of ESCA results in this system is not simple because the signal is highly surface-sensitive and is prone to misinterpretation because of contamination of the top surface by oxidation in the ambient atmosphere. While this can be addressed to some extent by *in situ* sputter removal of some of the surface layers, this

also complicates the question because the surface sputtering has a limited depth resolution, while the multilayer's composition modulation is on a very short distance scale. The sputter removal would likely expose more than one multilayer material at once by an uneven removal of the surface and confound interpretation of the composition of the different layers. However, work on a carefully-planned set of specimens, such as a series of bilayers of a constant tungsten thickness with varying thicknesses of B_4C on top, could give useful new information on the extent of intermixing and show what bonds are forming.

The field of diffuse scattering from multilayers remains under-exploited. With the availability of bright synchrotron sources in the soft x-ray regime with detectors of low noise levels and many orders of magnitude dynamic range, such as Beamline 6.3.2 at the ALS, and complete theoretical models like those of Sinha and Stearns cited in Chapter 7, scattering at various non-specular geometries provides tools not previously available for investigating in-plane roughness components and roughness correlation. The Grazing-Incidence X-ray Scattering (GIXS) geometry applied in the hard x-ray by Salditt *et al.*[8-10] allows measurements with the scattering vector nearly in the plane of the multilayer without using a transmission specimen, and geometries used in this study such as rocking curves, are also now feasible in the soft x-ray.

Finally, packaged computer codes are available[§] that can simulate the sputtering process, including ion-peening and atomic implantation effects, and could probably provide a realistic model of this complicated system of amorphous, nonepitaxial and reactive materials with a large mass difference. With the increasing availability of computational power this could provide a valuable study of very thin sputtered layers, in a less idealized case than many existing studies, that may find insights into the subtleties of many other systems.

[§] The TRIM90 code can give energy distributions of sputtered particles and reflected neutrals in a given sputtering experiment, and the TRIDYN code (available from the journal Computer Physics Communications) can incorporate this information into growth models.

References

[1]A. Kloidt, H. J. Stock, U. Kleineberg *et al.*, "Smoothing of interfaces in ultrathin Mo/Si multilayers by ion bombardment," presented at the 12th International Vacuum Congress, The Hague, Netherlands, 1992 (unpublished).

[2]S. P. Vernon, D. G. Stearns, and R. S. Rosen, "Ion-assisted sputter deposition of molybdenum-silicon multilayers (for soft X-ray optics)," Applied Optics **32** (34), 6969-74 (1993).

[3]D. G. Stearns, R. S. Rosen, and S. P. Vernon, "Fabrication of high-reflectance Mo-Si multilayer mirrors by planar-magnetron sputtering," Journal of Vacuum Science & Technology A (Vacuum, Surfaces, and Films) **9** (5), 2662-9 (1991).

[4]R. E. Somekh, W. C. Shih, K. Dyrbye *et al.*, "The sputter deposition of metal multilayers," presented at the X-Ray Instrumentation in Medicine and Biology, Plasma Physics, Astrophysics and Synchrotron Radiation, Paris, France, 1989 (unpublished).

[5]E. E. Fullerton, J. Pearson, C. H. Sowers *et al.*, "Interfacial roughness of sputtered multilayers: Nb/Si," Physical Review B (Condensed Matter) **48** (23), 17432-44 (1993).

[6]J. DuMond and J. P. Youtz, Journal of Applied Physics **11**, 357 (1940).

[7]A. F. Jankowski, L. R. Schrawyer, and M. A. Wall, "Structural stability of heat-treated W/C and W/B_4C multilayers," Journal of Applied Physics **68** (10), 5162-8 (1990).

[8]T. Salditt, T. H. Metzger, and J. Peisl, "Kinetic roughness of amorphous multilayers studied by diffuse X-ray scattering," Physical Review Letters **73** (16), 2228-31 (1994).

[9]T. Salditt, T. H. Metzger, J. Peisl *et al.*, "Determination of the height-height correlation function of rough surfaces from diffuse X-ray scattering," Europhysics Letters **32** (4), 331-6 (1995).

[10]T. Salditt, T. H. Metzger, Ch Brandt *et al.*, "Determination of the static scaling exponent of self-affine interfaces by nonspecular X-ray scattering," Physical Review B (Condensed Matter) **51** (9), 5617-27 (1995).

Ernest Orlando Lawrence Berkeley National Laboratory
One Cyclotron Road | Berkeley, California 94720

Prepared for the U.S. Department of Energy under Contract No. DE-AC03-76SF00098